VASILEIOS A. PAPADIMITRIOU

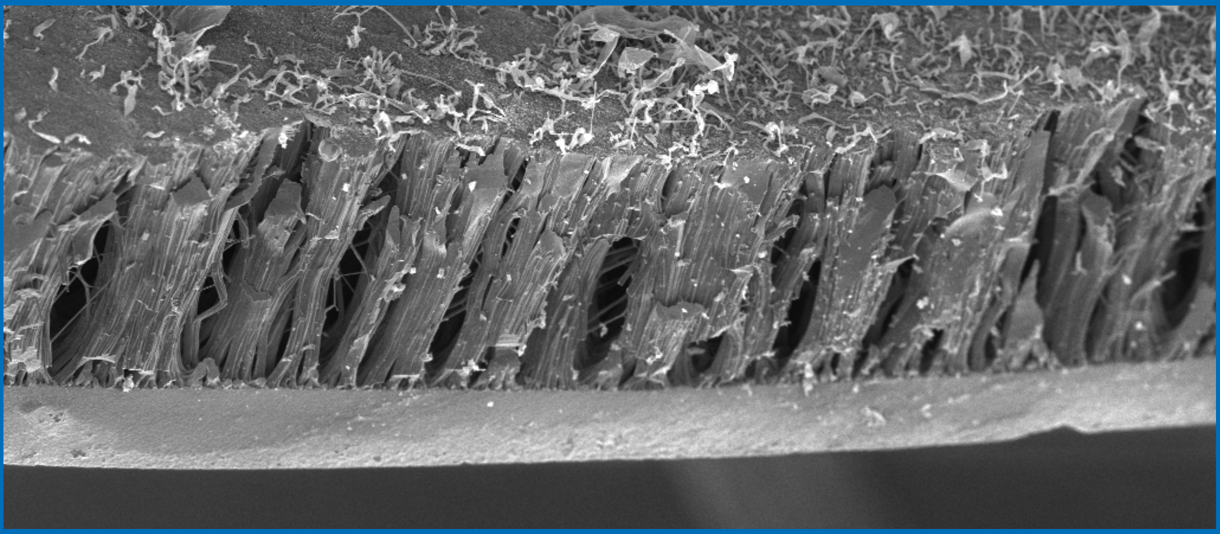

MASTER THESIS

MEMBRANE TEMPLATED ACTIVATED CARBON FOR ELECTRIC DOUBLE LAYER CAPACITORS

Master of Science in Electrical Engineering

in the

BIOS - Lab-on-a-Chip Group
University of Twente

SEPTEMBER 2015

University Of Twente

Master of Science in Electrical Engineering

Master Thesis

Membrane Templated Activated Carbon for Electric Double Layer Capacitors

---

Author:
Vasileios A. Papadimitriou

Supervisors:
Wouter Olthuis, BIOS-UT
Yawar Abbas, BIOS-UT

Examining Committee:
Albert van den Berg, BIOS-UT
Wouter Olthuis, BIOS-UT
Yawar Abbas, BIOS-UT
Johan Bomer, BIOS-UT
Niels Tas, MCS-UT

ECTS: 40

Submitted to the Board of Examiners in partial
fulfillment of the requirements for the degree of
MSc. Electrical Engineering
of the
University of Twente.

September 2015

"Science is nothing but perception."

Plato

"Where the senses fail us, reason must step in."

Galileo Galilei

This work is dedicated to my family. Thank you for everything.

Acknowledgements

Before the ”science” stuff starts I would like to thank a not so few people for the thesis and the whole master program.

First of all, I would like to thank my family for one more time, for all their support, psychological and financial, especially this last two years that I am away from Greece.

I want also to thank all my friends for all the fun we had this last two years and the fun that will follow. I am not going to name all of you individually because I am going to forget a couple of names and then I have to live with their whining about it.

I want to thank all the people in BIOS - Lab-on-a-Chip that made possible for me to do this thesis and all the fun this last seven months.

I also want to thank Guido Giammaria from the Catalytic Processes and Materials (CMP) group, that let me use his furnace and let me annoy him several times per week.

I want to thank Cindy Huiskes from the Inorganic Membranes (IM) group that did all the BET measurements for me.

I want to thank all the people from MESA+ Cleanroom that helped throughout the thesis, with equipment training and advises.

Last but not least I want to thank my supervisors (Wouter and Yawar) and Johan, with whom we did the whole thesis together. And an extra thank you to Wouter for his guidance through the whole master program, since he was my person of contact in BIOS from day one and my supervisor in my internship.

Contents

List of Figures

List of Tables

Abbreviations

EDLC	**E**lectric **D**ouble **L**ayer **C**apacitor
EDL	**E**lectric **D**ouble **L**ayer
MBT	**M**odified Poisson-**B**oltzmann **T**heory
IL	**I**onic **L**iquids
AC	**A**ctivated **C**arbon
TC	**T**emplated **C**arbon
CDC	**C**arbide-**D**erived-**C**arbon
CV	**C**yclic **V**oltametry
EIS	**E**lectrochemical **I**mpedance **S**pectroscopy
BET	**B**runauer-**E**mmet-**T**eller
PZC	**P**otential of **Z**ero **C**harge
EDR	**E**quivalent **D**istributed **R**esistance
ESR	**E**quivalent **S**eries **R**esistance
ZPC	**Z**ero **P**otential **C**urrent

Physical Constants

Vacuum permittivity $\epsilon_0 = 8.8541 \times 10^{-12}\ F/m$

Boltzmann constant $k_B = 1.3806488 \times 10^{-23}\ m^2\ kg\ s^{-2} K^{-1}$

Avogadro constant $N_A = 6.022140 \times 10^{23}\ mol^{-1}$

Elementary charge $e = 1.60217657 \times 10^{-19}\ C$

Symbols

C_h	Helmholtz EDL model capacitance	F
d_H	Helmholtz EDL model distance between plates	m
T	Absolute temperature	K
I	Ionic strength of electrolyte	M
c_i^0	Concentration of i species in the bulk	M
c_i^0	Bulk salt concentration	M
c_i	Ion density distribution of i species	M
z_i	Ion valency	$Dimensionless$
C_S	Specific area capacitance	F/m^2
C_S^D	Specific area capacitance of diffuse layer	F/m^2
C_S^S	Specific area capacitance of Stern layer	F/m^2
R_{ion}	Hydrated ion radius	m
Q	Stored charge	C
A	Electrode/electrolyte interface area	m^2
n	Normal unit vector at Electrode/electrolyte interface	$Dimensionless$
A_{sp}	Specific surface area	m^2/g
C_g	Gravimetric capacitance	F/g
D	Diffusion coefficient	m^2/s
D_∞	Diffusion coefficient in bulk	m^2/s
J	Molar flux	$mol\ m^{-2}/s$
u	Fluid velocity	m/s
F_D	Chemical Potential Force	N
F_{fr}	Stokes' friction Force	N
r	Particle radius	m
J_∞	Molar flux in bulk	$mol\ m^{-2}/s$

J_{pore}	Molar flux in nanopore	$mol\ m^{-2}/s$
h_d	Enhanced drag	$Dimensionless$
E	Stored Energy	J
V	Operational potential	V
R_{cell}	Total cell electric resistance	Ω
ϵ_r	Dielectric constant of electrolyte	$Dimensionless$
λ_D	Debye Length	m
σ	Surface charge density	C/m^2
ψ	Potential	V
ρ^*	Local electric charge density	C/m^3
ψ_S	Surface Potential	V/m^2
μ	Dynamic viscosity	Ns/m^2
s	CV Scan rate	V/s

UNIVERSITY OF TWENTE
Faculty of Electrical Engineering, Mathematics and Computer Science.

Master of Science in Electrical Engineering

Abstract

Membrane Templated Activated Carbon for Electric Double Layer Capacitors

by Vasileios A. Papadimitriou

In this thesis the field of Electric Double Layer Capacitors (EDLC) is investigated. Two main research questions are discussed.

First, which are the properties for an ideal EDLC electrode in terms of energy (capacitance) and power density? The literature study revealed that both nanopores and meso-/macropores are required for an ideal electrode. Nanopores enhance the energy density due to desolvation effects, when the pore size is between solvated and bare electrolyte ion size. Meso-/macropores enhance the power density due to faster diffusion in them than in nanopores. In addition, the resistance between electrode and current collector also affects the power density.

Second, can an electrode be fabricated in respect with the findings of the first question? By combining two techniques which are typically used in EDLC fabrication, namely templated carbon (TC) and activated carbon (AC), several electrodes were fabricated with a combination of nano-, meso- and macropores. An addition, a new type of current collector is proposed.

The electrodes have been characterized electrochemically (via cyclic voltametry, electrochemical impedance spectroscopy and charge-discharge cycling) and physically (via scanning electron microscopy and Brunauer-Emmet-Teller method). The electrodes exhibit capacitance up to 217.63 F/g and power up to 25.83 kW/kg.

Chapter 1

Introduction

Nowadays with the advance of technology new ways of detaching ourselves from the need of fossil fuels have emerged. This advance, especially, in the energy field, from renewable energies to portable devices and electric cars, created a need for a reliable, high power electric energy storage. Electrochemical capacitors, also known as supercacitors, have demonstrated several unique characteristics that make them the appealing candidates to cover that need [1, 2, 3, 4, 5]. When a discussion about electric energy storage devices takes place, one must show a energy versus power plot also known as Ragone plot (Figure 1.1).

The goal is to move to the top right regions of the Ragone plot where devices pack high energy and high power. Supercapacitors have properties which lay between electrochemical cells [6, 7, 8] and traditional electrostatic capacitors. Specifically, they can pack lower energy densities comparable to the modern batteries. Electrochemical capacitors, similar to electrostatic capacitors, can pack higher power density, better cycle life, long storage duration and charge rate as compared to batteries. In contrast, electrochemical capacitors pack much higher energy storage than electrostatic capacitors[1, 2, 3].

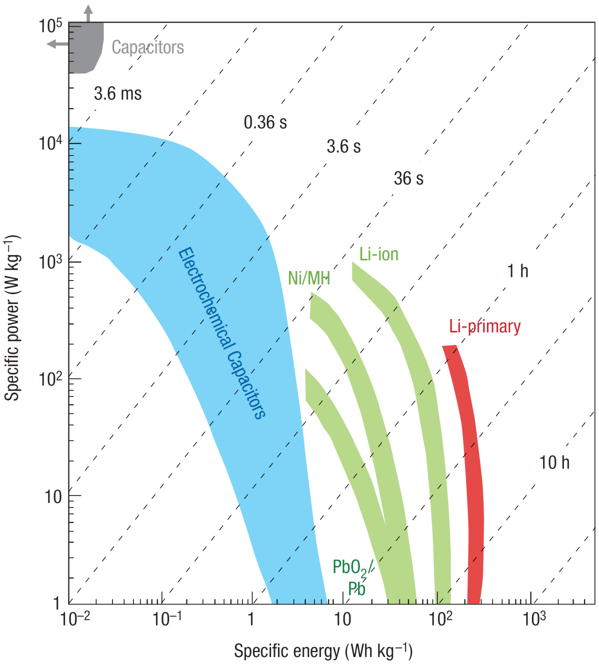

FIGURE 1.1: Ragone plot. Specific power against specific energy, for various electric energy storage devices. The 45^o dashed lines describe the charge/discharge time of the devices. Electrochemical capacitors cover a wide range of applications. [9]

That fact makes supercapacitors ideal for applications where high power is needed. One application is the energy regeneration systems. An example is the Formula 1 racing cars' KERS (Kinetic Energy Regeneration System.) where during the braking of vehicle (or from the exhaust system) thermal energy is transduced into electric energy and stored in a supercapacitor. The driver can use that energy to power an 82 horsepower motor for 3-6 seconds [10]. The supercapacitor fully charges and discharges within seconds. Such systems as KERS with the use of supercapacitors are slowly spreading to commercial application from electric bikes and cars to public transit vehicles, such as buses and trains. In addition, supercapacitors' ability to operate in wider operating temperature window make them appealing for harsh environment application. E.g. electrochemical capacitors are used in the emergency doors of Airbus A380 planes which proves that supercapacitors' technology is mature enough in terms of reliability, safety and performance [9]. Nevertheless, the race in order to create electrochemical capacitors that pack higher energy and power density is still on.

Supercapacitors can be divided into two main categories based on the way that they store energy inside them [11]. The first category is the faradaic pseudocapacitor which uses fast reversible faradaic reactions store charge in different oxidation states, using active materials such as metal oxides and conducting polymers[1, 2, 5]. The second category is the Electric Double Layer Capacitor (EDLC) which stores energy electrostatically in the electric double layer which is created in the interface between electrode and electrolyte[12, 13, 14]. Since the EDLCs store charge physically, the microstructure and composition of the electrode material experience no significant changes during charging and discharging. Pseudocapacitors can pack higher energy density (up to $2,188Fg^{-1}$ have been reported[15]) than EDLC due to their redox reactions, but EDLC have longer cycle life, higher power density and wider operating voltage and temperature range.

This report will focus on EDLCs. Specifically, it discuss to answer two main research question. First: What are the ideal electrode properties for high power and energy EDLCs based on literature? And second, from the findings of the first question, can we fabricate such an electrode? EDLC electrodes are made exclusively out of carbon. There are several methods available for the fabrication of carbon supercapacitor electrodes. The most used methods/material are the Activated Carbons (AC), the Carbide-Derived-Carbons (CDC) and the Templated Carbons(TC). All of the methods have some advantages and disadvantages in the resulted material. In our capacitor a "hybrid" electrode was fabricated with the use of two methods, namely AC and TC, in an attempt to combine their advantages, which are going to be discussed in the following chapter.

This report consists of the following chapters: First in chapter 2 a theoretical background on the electric double layer and electric double layer capacitors is going to be built. In addition the materials along with fabrication and characterization methods used in EDLCs are going to be investigated. In chapter 3 the ideal electrode properties will be extracted and based on them our proposal on how to fabricate such an electrode is presented. In chapter 4 after characterization of our device, the results are presented and discussed. Finally, in chapter 5 a summary of the work is presented and some future work is proposed.

Chapter 2

Background

2.1 Electric Double Layer

2.1.1 History and EDL models

The theory of the electric double layer dates back to the late 19th century as part of the classical electrokinetics theory. First, Helmholtz [16] proposed a model of a double layer that is created in the interface between solid surface (electrode) and an ionic solution (electrolyte). The charges on the surface attract the counter-charges (ions in the electrolyte) in order to achieve the electro-neutrality. The proposed model was similar to an electrostatic capacitor. One plate is the solid electrode and the other one is a layer of charged particles of electrolyte. The two plate are separated by an imaginary plate in the solid/liquid interface. Helmholtz model predicted a capacitance

$$C_h = \frac{\epsilon_r \epsilon_0}{d_H},$$

where ϵ_r is the dielectric constant of the electrolyte, ϵ_0 is the vacuum permittivity and d_H is the distance between the capacitor plates. This capacitance, in contrast with the reported experimental results, was independent of ion concentration in the electrolyte and the surface charge/potential.

Later, Gouy [17] and Chapman [18] modified Helmholtz model to include electrode potential and ion concentration of the electrolyte. In the modified model electrostatic forces and random thermal movement arrange the ions in a so-called diffuse layer. The electric field in the diffuse layer is calculated by solving the Poisson-Boltzmann equation. The thickness of this diffuse layer is described by a quantity called Debye length [19] (for monovalent electrolyte and low surface potentials)

$$\lambda_D = \kappa^{-1} = \sqrt{\frac{\epsilon_r \epsilon_0 k_B T}{2 N_A e^2 I}},$$

where ϵ_r is the dielectric constant of the electrolyte, ϵ_0 is the vacuum permittivity, k_B is the Boltzmann constant, N_A is the Avogadro number, e is the elementary charge and I is the ionic strength of the electrolyte. The drawback of this model was that, ions were taken as dimensionless point charges, this resulted in unrealistic values of ion concentration in the diffuse layer, because of the neglect of steric repulsion.[20].

Stern [21] by combining the Gouy-Chapman and Helmholtz models proposed a new model of electric double layer that was consisting of two different regions. The region close to the electrode which is called Stern layer, and the diffuse layer of the Gouy-Chapman model further away from the electrode. His model took into account the finite size of ions and the adsorption (covalent) forces of ions. Grahame [22] further improved the Stern model by distinguishing two different regions in the Stern layer where ions adsorb due to different forces (i.e. covalent and electrostatic). A schematic presentation of the models is shown in figure 2.1

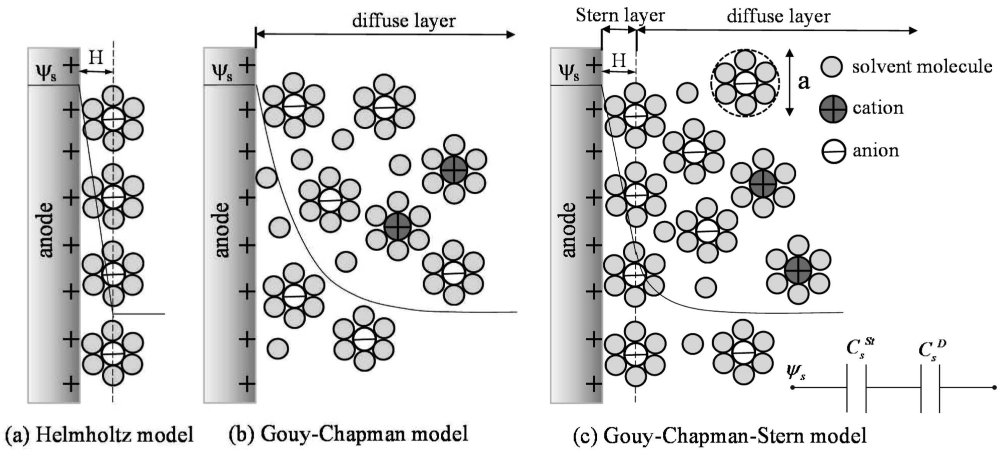

(a) Helmholtz model (b) Gouy-Chapman model (c) Gouy-Chapman-Stern model

FIGURE 2.1: Schematic representation of different models of electric double layer. a) Helmholtz model where electrolyte ions arrange themselves in a layer on the surface of the electrode. b)Gouy-Chapman model where the electrolyte ions are arranged in a diffuse layer. c) Stern model which combines the previous models.[23]

Until today the Stern-Grahame model is accepted and describes sufficiently the electric double layer. But there are several assumptions in the Possoin-Boltzmann theory for the calculations of the diffuse layer, which lead to limitations. Specifically [24],

- The finite size of ions is neglected.
- Surfaces are considered to be flat in molecular scale.
- The ions in solution are considered as continue charge distribution, i.e. the discrete nature of their charge is ignored.
- The dielectric constant of the electrolyte is considered to be constant over the whole medium, which is not true in practice.
- All non-Coulombic interactions are not taken into account.
- Image forces between ions and surface are neglected.

Because of the aforementioned limitations, for electric double layer simulations for EDLC, several Modified Poisson-Boltzmann Theories(MBT) have been proposed. A recent review [25] present some MBT in depth.

2.1.2 Mathematical Analysis of EDL

Ion concentration and potential distribution[26] - In order to mathematical describe the electric double layer all that is needed is the electric potential ψ near a uniformly charged surface with surface charge density σ in C/m^2. By electric potential is meant the three dimensional distribution $\psi(x, y, z)$ of the potential. When the surface charge density and the potential are related, generally the Poisson's equation is used:

$$\nabla^2\psi = \frac{\partial^2\psi}{\partial x^2} + \frac{\partial^2\psi}{\partial y^2} + \frac{\partial^2\psi}{\partial z^2} = -\frac{\rho^*}{\epsilon_r\epsilon_0},$$

where ϵ_r is the dielectric constant of the electrolyte, ϵ_0 is the vacuum permittivity and ρ^* is the local electric charge density in C/m^3.

Boltzmann's equation describes the local ion density distribution, c_i:

$$c_i = c_i^0 * \exp(-\frac{z_i e\psi}{k_B T}),$$

where c_i^0 is the concentration of the i species in the bulk, z_i is the ion valence, e is the elementary charge, k_B is Boltzmann's constant and T is the absolute temperature. For all the species in the bulk according to the previous formula, the local electric charge density is:

$$\rho^* = \sum_i z_i e c_i = e c_0 \sum_i z_i \exp(-\frac{z_i e\psi}{k_B T}),$$

where c_0 is the bulk salt concentration. By substituting ρ^* in the Poisson equation we get the Poisson-Boltzmann equation:

$$\nabla^2 \psi = \frac{e c_0}{\epsilon_r \epsilon_0} \sum_i z_i \exp(-\frac{z_i e\psi}{k_B T})$$

Poisson-Boltzmann equation is a partial differential equation of second order, which in most cases has to be solved numerically. Only for some simple geometries can it be solved analytically. Furthermore, depending on the case under investigation several approximations can be used. For example for highly diluted salts and low surface potential the Debeye-Huckel approximation can be used. Low surface potential means that $z_i e\psi << k_b T$ which corresponds to a surface potential of $25,7mV$ at $T = 300K$. In practice, Debeye-Huckel approximation describes sufficiently the experimental data up to surface potentials of $\sim 80mV$.

For EDLC where is a case of high surface potential and electrolytes with high concentration of ions are used, such approximations are not possible. The different mathematical ways of solving the Poisson-Boltzmann equation for the EDLC cases it is beyond the scope of this report. But when the equation is numerically solved, a known ψ (i.e. the three dimensional distribution of ψ) is sufficient to calculate an expected capacitance.

Differential Capacitance - Even on the first model proposed by Helmholtz, EDL behaves as a capacitor. The amount of energy stored in this capacitor is described by the differential capacitance[27]. The Stern layer and the diffuse layer contribute separately in the total capacitance. The two layers behave like two capacitors connected in series[28]. Hence,

$$\frac{1}{C_S} = \frac{1}{C_S^D} + \frac{1}{C_S^S},$$

where C_S is the total specific area capacitance (F/m^2), C_S^D and C_S^S are the specific area capacitance contribution of diffuse and Stern layer, respectively. The Stern layer contribution in the capacitance equals to[26]:

$$C_S^S = 2\frac{\epsilon_r \epsilon_0}{R_{ion}},$$

where R_{ion} is the hydrated ion radius. The diffuse layer capacitance contribution can be calculated by [28]:

$$C_S^D = \frac{Q}{\psi_S A},$$

Where Q is the total charge stored due to the diffuse layer, ψ_S is the surface potential on the electrode and A is the electrode/electrolyte interface area. The total charge can be calculated by integrating the potential distribution over the total double layer area A,

$$Q = \int_A \epsilon_r \epsilon_0 (\mathbf{n} \cdot \nabla \psi) dA,$$

where $\mathbf{n}$ is the normal unit vector at the electrode/electrolyte interface. In order to calculate the gravimetric capacitance (F/g) all we need to do is multiply the specific area capacitance (F/m^2) by the specific surface area (SSA) $A_{sp}(m^2/g)$.

$$C_g = C_S * A_{sp}$$

Power Density - The power density translates to how fast can a EDL be formed, i.e. how fast do the ions come into an equilibrium near the electrode surface. One can use the Nernst-Planck equation to describe the movement of ions in an electrolyte under the influence of both concentration gradient and electric field [29]. The time dependent form of Nersnst-Planck equation is:

$$\frac{\partial c}{\partial t} = \nabla \left[D\nabla c - uc + \frac{Dze}{k_B T} c \left(\nabla \psi + \frac{\partial \mathbf{A}}{\partial t}) \right) \right]$$

And the steady state Nernst-Planck equations is:

$$J = -\Bigg[\underbrace{D\nabla c}_{\substack{\text{Diffusion}\\ \text{Contribution}}} + \underbrace{\frac{Dze}{k_B T} c(\nabla\psi)}_{\substack{\text{Electric Field}\\ \text{Contribution}}} \Bigg],$$

where u is the fluid velocity, J is the flux of ions, D is the diffusion coefficient, ∇c is the concentration gradient.

It must be noted that the diffusion in pores is different than the diffusion in the bulk. In general, the force that moves the ions in case of diffusive flux comes from gradient of the chemical potential and it is equal to :

$$F_D = k_B T \frac{\partial lnc}{\partial x}$$

for one dimensional diffusion, where x is the distance in the direction of concentration gradient. The friction force according to Stokes for spherical particles equals:

$$F_{fr} = 6\pi r \mu v,$$

where r is the particle radius, μ the dynamic viscosity and the v the particle velocity. When the sum of the two forces is zero we can deduce the terminal particle velocity and thus the flux:

$$J_\infty = -\frac{k_B T}{6\pi\mu r}\frac{\partial c}{\partial x} = -D_\infty \frac{\partial c}{\partial x},$$

where

$$D_\infty = \frac{k_B T}{6\pi\mu r}$$

which is the diffusion coefficient in the bulk.

According to [30] in nanopores because of the proximity of the walls there will be an extra coefficient called enhanced drag, h_d which makes the diffusion slower. Specifically, the ratio between the flux in the pore, J_{pore}, and flux in the bulk, J_∞ for slit like pores equals to:

$$\frac{J_{pore}}{J_{\infty}} = h_d \left(1 - \frac{r}{h}\right),$$

where h is the channel width. This ratio is plotted against r/h in figure 2.2.

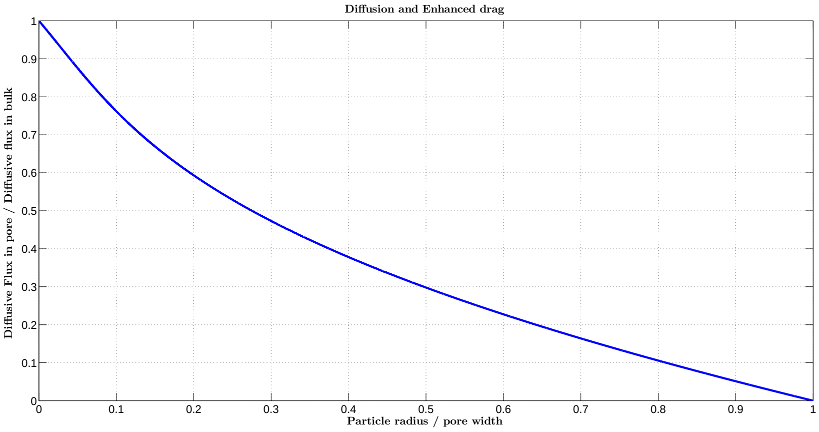

FIGURE 2.2: Ratio between diffusion in bulk and in pores in respect with the ratio of particle size and channel width. The bigger the particle compared to the pore the slower the diffusion of species

For simple geometries, this analysis can give a qualitative description of power density. But for the practical cases of EDLC other methods are used for the evaluation of their power, which will be described in section 2.3.

2.2 Electric Double Layer Capacitors (EDLCs)

2.2.1 Energy Density

Electric Double Layer Capacitors store their energy in the differential capacitance of the EDL between the electrolyte and electrode interface. According to the previously described model, the capacitance is influenced by two factors.

First, factor is the potential ψ. The increment of surface potential is limited by the nature of electrolyte, e.g. In aqueous electrolytes, the water will start to decompose to O_2 and H_2 at $1.2 Volts$. In addition, ion valence, size and salt concentration affect the double layer.

The second factor is the surface area of the electrode. This is a reasonable factor, since EDL is a liquid/solid interface phenomenon. The higher the electrode surface, the higher the EDL area, the higher the amount of ions and hence the charge stored in the capacitor [31]. Both experimental and simulations result show almost linear relation between specific surface area (m^2/g) and gravimetric capacitance (F/g)(Figure 2.3).

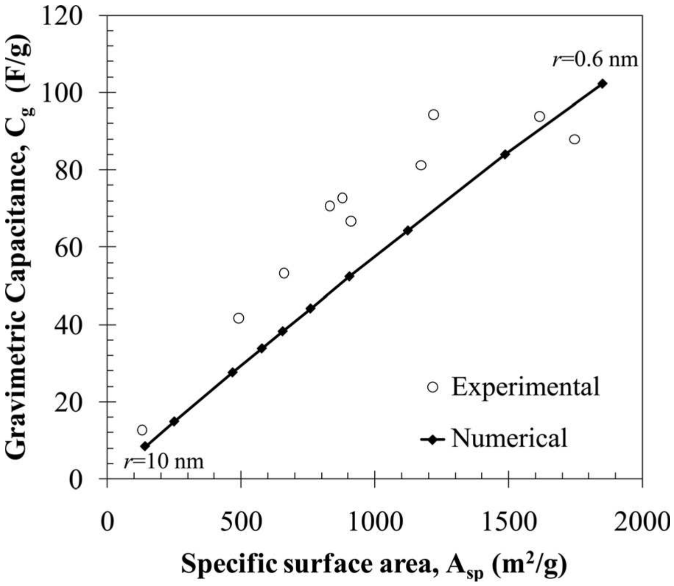

Figure 2.3: Relation between specific surface area and gravimetric capacitance. Both numerical and experimental results show linear dependency between gravimetric capacitance and specific surface area. [28]

In order to create electrodes with high specific surface area, electrodes with high porosity have been created. But an abnormal behavior is noticed when the pore size decreases. The normalized capacitance decreases with the decrease in pore size until a critical value ($\sim 1nm$) is reached [32]. When the pores are smaller than this value a sharp increase in the specific capacitance is noticed, despite the fact that the size of solvated ion is larger than the pore itself [33](Figure 2.4) The aforementioned EDL models fail to describe such behavior. One explanation for this phenomenon is, that the ions distort or partially lose their solvation shell so they can enter the pore. This creates a so called superionic state, where the electrostatic repulsion forces are screened out and greater packing of ion/energy is achieved. This theory have been experimentally confirmed by many research groups [34, 35, 36]. This nanoconfinement is taking place in micropores in the electrode material [37]. Experiments with organic electrolytes shown that the ideal pore size, for the maximum capacitance lays between the solvated and desolvated ion size[33, 38](Figure 2.5). That means that only partial desolvation of the ion takes place. Recent articles ([39]) report that loosing the first molecule of the solvation shell requires less energy than loosing the last molecule of the shell, so partial desolvation is more energetic favorable than complete desolvation.

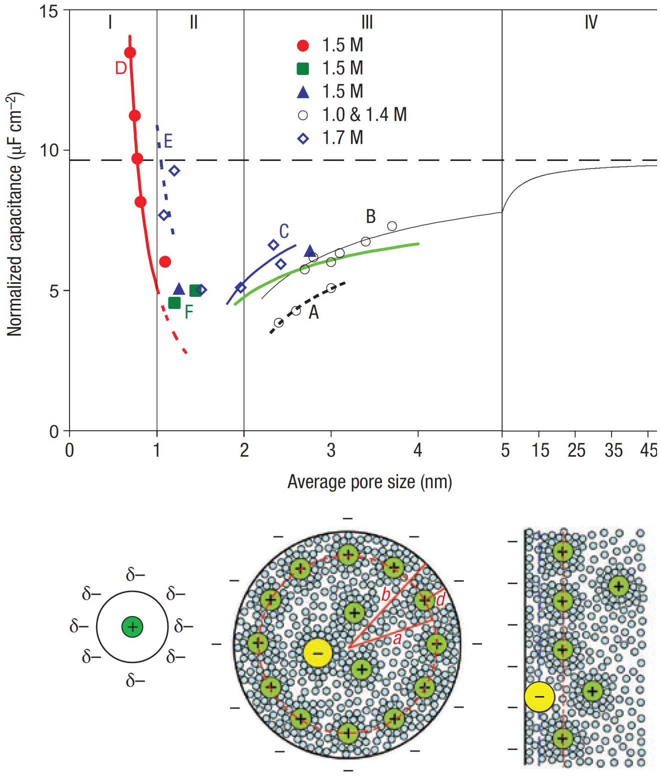

FIGURE 2.4: Average pore size against normalized specific capacitance. The symbols show the experimental data for different samples. For all samples the same electrolyte has been used, namely (NEt_4^+, BF_4^-), with different concetrations, marked on the legend. When the pore size is much larger than the ion size the surface can be considered flat (Zone IV). With the decrease of pore size(Zone III), we can model the EDL as a cylindrical double layer capacitor, where less solvated ions can approach the surface compared to zone IV, hence the specific capacitance drops. In Zone I where the pore size is comparable to the ion size there is a sharp increment in the capacitance because of the desolvation of the ions. [40]

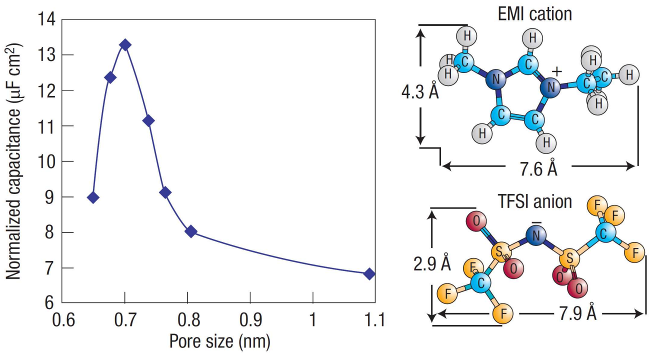

FIGURE 2.5: Relation between specific capacitance and pore size. The peak in the capacitance occurs when the pore size is comparable to the ion size. [38]

Despite the fact that capacitance of an EDLC is the first factor under investigation for its capability to store energy, it tells half the story about the energy density. The energy, E, stored in a capacitor is given by the following formula:

$$E = \frac{1}{2}CV^2,$$

where C is the capacitance and V the operational voltage. So the energy is not depended only on the capacitance but also on the operating voltage. As it was noted before, the limiting factor for the potential is the electrochemical stability window of the electrolyte, i.e. at what voltage does the electrolyte decompose. Only but a few more details about the electrolyte will be given in section 2.3, since this thesis is focused on the solid electrode.

2.2.2 Power Density

The second factor that needs to be investigated for EDLCs is the power density. As mentioned previously, power density means how fast can we charge and discharge the capacitor. The power density translates to resistances. The total resistance, also called equivalent series resistance (ESR) or cell resistance (R_{Cell}) is a contribution of several factors. The most dominant ones are the following [41].

First, the ionic resistance of bulk electrolyte. This comes directly from the electric properties of the electrolyte solution. Since this thesis is focused on the solid electrode of the EDLCs this factor is beyond its scope.

Second, the electric resistance of the electrode material. That material for EDLCs is usually carbon and it will be analyzed in the following section (Section 2.3).

Third, is the electric resistance/capacitance between active electrode material and current collector. In the commercial EDLCs there is a layer of metal in touch with the carbon electrode that is used a current collector. At the interface between carbon and metal a capacitance and resistance is created. The use of current collector will be described in section 2.3 and a proposal for minimizing that resistance/capacitance is described in chapter 3.

Another resistance is the ion diffusive resistance. This resistance depends on the electrolyte itself along with the structure of the electrode, since it describes the resistance of transport of ion inside the porous structure. The factors that affect this resistance are both the pore size and the shape of the pores (tortuosity of the electrode)[42]. In general, highly and randomly disordered porous electrodes (e.g. made out of activated carbon grains and pores with bottleneck features) behave poorly from power point of view, compared to highly ordered porous electrodes (e.g. microfabricated or templated carbon electrodes). In order to achieve high ion diffusion coefficient, mesopores with tuortosity close to 1 are needed, since the diffusion is much lower in micropores [43]. Nevertheless, if micropores are still needed, for the increase of the capacitance, then the diffusion path (pore length) must be as short as possible. In general there is a trade off between pore size and pore length to achieve the optimal diffusion and diffusive resistance.

2.3 EDLC Materials & Fabrication Methods

In this section the typical materials and fabrication methods of EDLCs in commercial and research level are going to be discussed.

2.3.1 Materials

As mentioned before EDLCs consist of the solid and liquid electrode (electrode and electrolyte). Despite the fact that this thesis is focused on the solid electrode, some details on the electrolyte must be given since the quality of the capacitor comes in the combination of the properties of both electrolyte and electrode.

Electrolyte - On the first EDLCs simple aqueous solutions with high concentration of salts (e.g. KOH, KCl) were used. The advantages of such electrolytes is that they are low cost, the ions are small and fast(high diffusion) and the ionic conductivity of the electrolyte is high. A drawback of the aqueous electrolytes is that low potential window can be used to avoid hydrolysis of H_2O. The maximum potential that can be applied is a bit over 1 Volt before the thermodynamic decomposition of the water.

For that reason organic electrolytes are now widely used in commercial applications. In such electrolytes, water is being replaced, as supporting electrolyte, by organic solvents. The most used supporting electrolytes are acetonytrile and propylene carbonate[33]. Organic electrolytes have a voltage limit close to $3V$ which almost three times higher than aqueous ones, which corresponds two a nine-fold increase in the stored energy. Because energy density is proportional to the voltage squared. In addition, organic electrolytes have a much wider operating temperature window (from $-40^{o}C$ to $+60^{o}C$). Nevertheless their low ionic conductivity, high cost and high flammability and toxicity are important disadvantages.

Finally, a lot of attention have been drawn by the so called ionic liquids (IL) and they are often called as the next generation of electrolytes[44]. IL are room temperature molten salts and they are solvent free electrolytes. Their voltage window is only depended on the electrochemical stability of ions which allows a voltage window of $> 4V$ at room temperature[45]. Their solvent free nature simplifies the coupling between ion and pore size, since no desolvations phenomena take place. In addition they are non-toxic and non-flammable and a wide variety of anions and cations is available to choose from, which makes them ideal for EDLC electrolytes. Despite that, their ionic conductivity is extremely low at room temperature which affects their performance and limits their use in typical operational temperatures.

Solid electrode - In the case of solid electrode the story is much shorter in terms of materials compared to the electrolytes. And that story is carbon. Carbon is almost exclusively the material used for EDLC electrodes. Its high conductivity, excellent chemical inertness, high thermal stability, low cost and high manufacturing versatility makes carbon the best candidate for electrode material.

2.3.2 Fabrication Methods

There many fabrication methods for carbon EDLC electrodes. The goal is to create electrodes with high and accessible surface area, high conductivity and tunable pore sizes. There are three most widely used fabrication methods, i.e. activated carbons(AC), carbide derived carbons (CDC) and templated carbons(TC).

Activated Carbon (AC) - This is the most widely commercially used method for EDLC electrodes, because of the low cost, simplicity and the yield of high specific surface area. The process can be generally described as follows. Various types of products with high concentration in carbon are used as precursors, usually organics (e.g. wood residues, nutshells etc.). The precursors are carbonized when heated in high temperatures in inert atmosphere such as N_2. The carbonation process is called pyrolysis. The carbon then is grind in powder form and activated. By activation, is meant the creation of pores and increase of the surface area. There are two main methods for activation, physical and chemical. For the physical activation the carbon material is heated to $700 - 1200^oC$ in oxidizing gas atmosphere such as H_2O steam or CO_2[46]. Oxygen radicals from the oxidizing gas react with the carbon molecules to create CO and $CO2$ and remove them from the surface of the carbon. The chemical activation requires lower temperatures ($400 - 700^oC$) but requires activating agents[45]. The most widely used activating agent is KOH[47]. Depending on the carbon precursor pyrolysis and activation can be done in one or two steps. Carbon activation is a highly tunable process and results in porous carbon with high surface area (up to $3000m^2/g$)[44]. Despite the tunability of the activation process the resulted carbon has a wide pore size distribution, meaning that micro- meso- and macro-pores will be created.

The resulted AC powder is mixed with binders and carbon black in order to create a paste. This paste is coated on an aluminum foil which works as a current collector. The current collector provides high conductive support for the carbon and an easy path for the charges to move during charging and discharging of the capacitor. But in contrast the added resistance/capacitance created in the interface of carbon and current collector costs some power to the total capacitor. A typical set up of a commercial capacitor is shown in figure 2.6

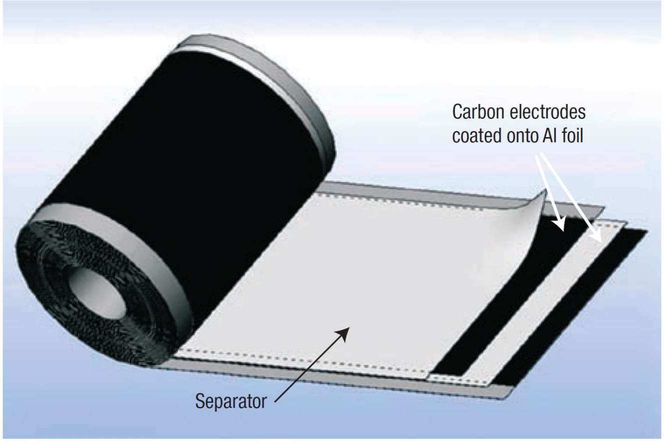

Figure 2.6: Schematic of commercial EDLC. The active material is coated on Aluminium foil and rolled in cylinder. The positive and negative electrode is electrically insulated with a separator, usually a kind of paper. The rolled capacitor is inserted in its housing and filled with electrolyte. [33]

Carbide Derived Carbon (CDC) - The idea behind the fabrication of CDCs is similar to the ACs, i.e. use a carbonaceous precursor material and remove the non-carbon molecules. The methods and the resulted carbon are different though. The precursor used in this case are carbides. Most widely Silicon Carbide (SiC) and Titanium carbide (TiC) are used. The removal of the non-carbon molecules from the precursor matrix is done by Chlorine treatment which is etching of precursors with Cl_2 gas at elevated temperatures.

Depending on the precursor and the chlorination parameters nanoporous carbon with narrow pore size distribution are created and the mean pore size can be controlled with sub-angstrom accuracy[48]. Such a pore size distribution of CDC is presented on figure 2.7. The CDC electrodes because of their narrow pore size distribution they can achieve 80% more volumetric capacitance and 50% more gravimetric capacitance compared to the AC electrodes [33]. Nevertheless, Chlorine treatment must be done in highly controlled environment because of the toxic and corrosive nature of the Cl_2 gas, which increases the cost of the CDCs. In addition carbides are more expensive than the organic AC precursors.

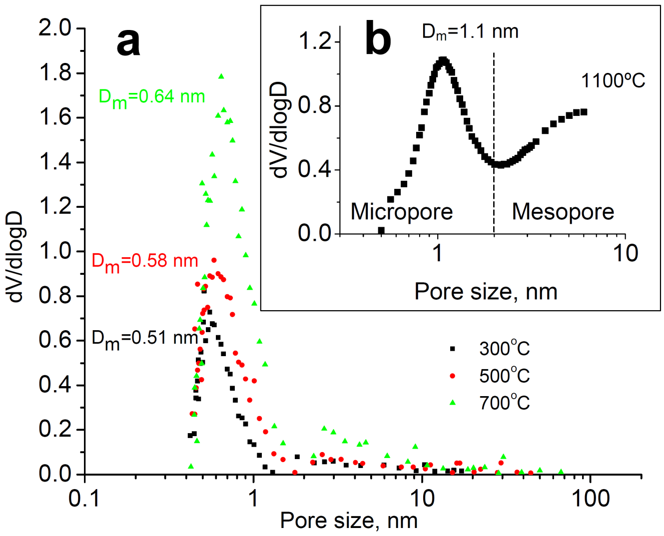

FIGURE 2.7: Differential pore size distribution of Ti_3SiC_2-CDCs produced by different chlorination parameters (temperature). In most of the samples uni-modal pores can be noticed, i.e. only nanopores and no mesopores or macropores can be seen. The mean pore size is controlled with sub-angstrom accuracy. [48]

Templated carbon (TC) - The principle behind templated carbons is different than AC and CDC. An already porous template is impregnated with the carbon precursor (usually polymers). Then the precursor is carbonized, usually by means of pyrolysis, and the template is then removed. The general concept of templating method is presented on figure 2.8.

The nanostructured carbon created by templating technique have very narrow pore size distribution, high surface area and depending on the template used they can have highly ordered pores and structures, which makes such electrodes ideal candidates for high power applications. In contrast, on CDC and AC electrodes only the size and not the shape of the pore can be controlled.

There are methods that they do not belong to these categories such as carbon nanotubes/nanofibers, carbon aerogels and nanofabricated carbon structures. There is an extensive amount of research on the fabrication of high surface area carbons.

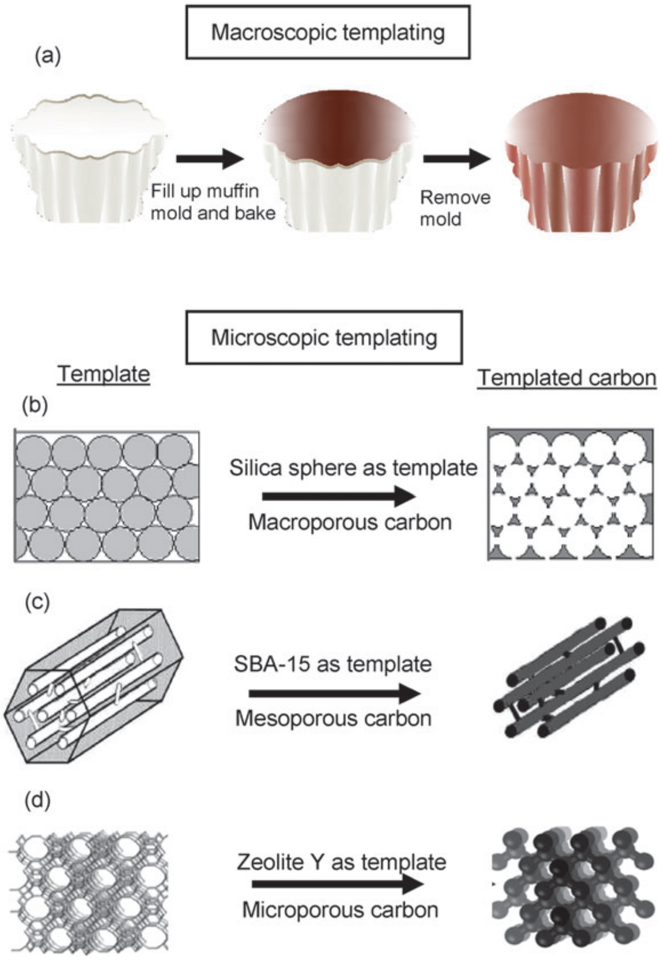

FIGURE 2.8: Graphical representation of templating method in different size scales. The template is filled with the precursor. The precursor is then carbonized and then the template is removed. [44]

2.4 Characterization Methods

For the characterization of electrodes three main techniques are used. Two of them are electrochemical methods, namely cyclic voltametry (CV) and electrochemical impedance spectroscopy (EIS) and the other one is physical (thermodynamic), namely Brunauer - Emmett – Teller (BET).

2.4.1 Cyclic Voltametry (CV)

Because the mathematical calculation of capacitance is nearly impossible for complex porous electrode geometries, experimental methods are used for the determination of the capacitance. The most widely used method is Cyclic Voltametry, where in a single experiment the potential is swept and the current versus potential curve is recorded[27], known as CV curve. In EDLCs where no faradaic reactions take place during the charge/discharge circles the CV curve has a rectangular shape. A typical EDLC CV curve is presented in Figure 4.17.

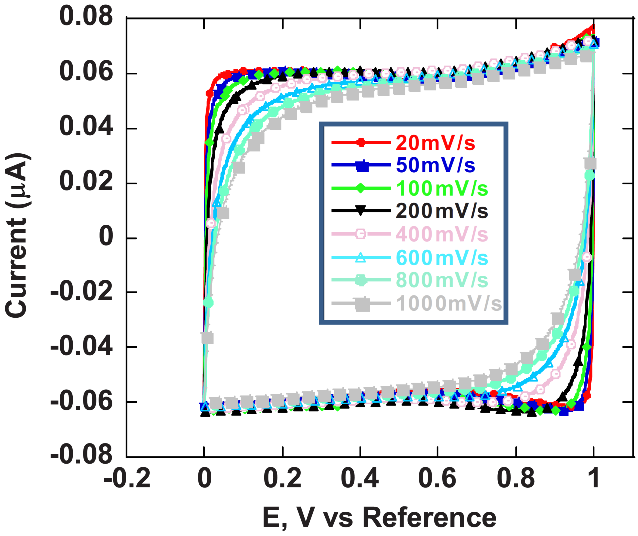

FIGURE 2.9: CV curve for EDLC. Current against Voltage for several scan-rates. The rectangular shape indicates that no redox reactions take place. [39]

Once the CV curve is recorded, the capacitance, of the electrode or cell under investigation, can be calculated by the following formula,

$$I = C\frac{dV}{dt},$$

where I is the current(vetical axis), C is the capacitance and dV/dt is the scan rate. Simply, by dividing the measured current, at a plateau of the graph, by the scan rate the capacitance of the electrode can be extracted. The gravimetric capacitance(F/g) can be calculated by dividing the CV capacitance with the mass of the electrode. The specific capacitance (F/m^2) can be calculated by dividing the gravimetric capacitance with the specific surface area of the electrode(m^2/g).

But because in reality the CV graph of supercapacitors is not completely rectangular like an ideal capacitor would exhibit, an average capacitance is calculated. So the formula for the average gravimetric capacitance can be derived as follows. The gravimetric capacitance(C_g in F/g) equals to:

$$C_g = \frac{Q}{mdV} = \frac{I(v)dt}{mdV} = \frac{I(v)}{m(dV/dt)},$$

where m is the mass of the electrode, (dV/dt) is the scan rate and from now on it will be noted as s and $I(v)$ is the current recorded through the CV. This gravimetric capacitance is the instant capacitance since there is a dependence between I and V. We get the average capacitance by integrating the aforementioned formula over a potential window.

$$\int_{V_2}^{V_1} C_g dv = \frac{\displaystyle\int_{V_2}^{V_1} I(v)dv}{ms}$$

$$(V_1 - V_2)C_g = \frac{\displaystyle\int_{V_2}^{V_1} I(v)dv}{ms}$$

$$C_g = \frac{\displaystyle\int_{V_2}^{V_1} I(v)dv}{ms(V_1 - V_2)}$$

The numerator of the fraction equals to the area of the CV curve between V_1 and V_2. But this area calculated from the current intergral includes two times the wanted capacitance since it includes a charge and a discharge cycle, so we need to divide by two. That gives us the final formula for average gravimetric capacitance:

$$C_g = \frac{\displaystyle\int_{V_2}^{V_1} I(v)dv}{2ms(V_1 - V_2)}$$

In addition, further information can be extracted from CV graphs. One example is the aging of the capacitor. The electrode is submitted to thousands of charge discharge (CV) cycles and the drop (if any) in capacitance is recorded. Typical commercial activated carbon supercapacitors have a life time of hundreds of thousand cycles and in [49] a review on the aging factors is presented.

Another example of use of CV is the qualitative explanation of the charging discharging process. I.e phenomena such as sieving, "surface saturation", charge depletion and electrolyte instability can be deduced from CV graphs.(Figure 2.10)

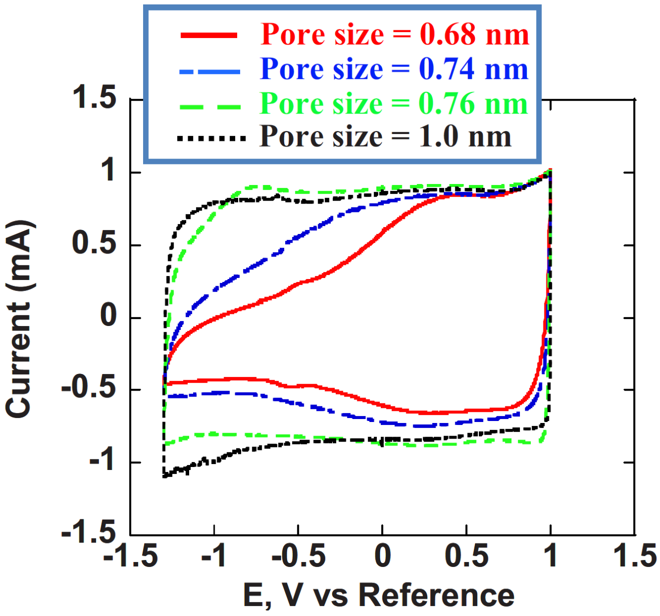

FIGURE 2.10: CV curve for EDLC electrodes with different pore sizes (marked in the legend). For the small pore samples the rectangular shape is distorted. That could either mean sieving effects or there was insufficient time for the ions to adsorb in the pores. The repetition of the experiment with lower scan rate can clarify the results. [39]

Finally, by using different scan rates and record any deviations from the ideal rectangular CV shape, some power density results can be extracted. But for power density characterization Electrochemical Impedance Spectroscopy is mainly used.

2.4.2 Electrochemical Impedance Spectroscopy (EIS)

As described in section 2 the power density depends on the equivalent series resistance, ESR, which is a contribution of several resistances. The most widely used method for characterization of capacitors in respect with their power is the electrochemical impedance spectroscopy(EIS).

During EIS an AC voltage with varying frequencies is applied on the capacitor, so a ”sweeping” of the frequencies takes place, and the impedance is recorded. Usually, the results are presented in a Nyquist plot where the imaginary part of the impedance is plotted as against the real part, a typical EIS graph for EDLCs is presented on figure 4.32. The advantage of EIS is that, the different contributions of the cell resistance can be distinguished, because of the sweep in the frequencies.

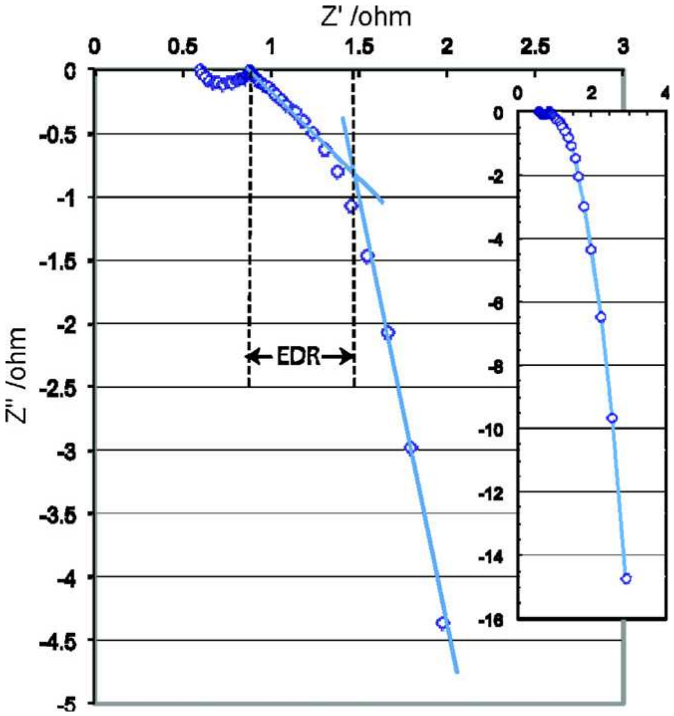

Figure 2.11: Typical EIS curve for EDLCs. The ESR is calculated from the point were the curve intercepts the real axis. The EDR is calculated from the width of the Warburg region (i.e. the region were the curve has a 45^o slope.)[41]

As it can be seen in figure 4.32 the EIS graph for EDLCs can be split in three regions. On high frequencies, a semicircle can be noticed. This resistance comes from the electric resistance of the electrode and mainly from the electric resistance/capacitance of the interface between the electrode and current collector. Typically the ESR is measured at the point were the graph intercepts the real axis. On the other hand, at low frequencies the capacitor has enough time to charge and discharge, so an almost vertical line appears which is the ideal capacitive behavior. The middle region is called Warburg region or distributed resistance region[41]. At this region a slope with 45^o is noticed, where the charge storage shifts from capacitive to diffusive controlled. In the Warburg region, one can evaluate the equivalent diffusive resistance (EDR) of the porous electrode [50, 51]. This is the main resistance of interest and it comes from the morphology of the electrode, the nature of electrolyte and the pore size in respect with the electrolyte ion size.

2.4.3 Brunauer–Emmett–Teller (BET) method

Other than the electrochemical properties of EDLCs (capacitance, cell resistance) also physical properties of the electrode is needed. The main property that needs to be quantified is the specific surface area, i.e. area per unit of mass (m^2/g). With the use of specific surface area and gravimetric capacitance (F/g), one can calculate the specific capacitance (F/m^2) which is an important quantity for the evaluation of the electrode. Specific capacitance, describes how well the area of carbon is used for the creation of capacitance. Phenomena like ion desolvation affect significantly the specific capacitance.

The main method used for the quantification of specific surface area is the Brunauer–Emmett–Teller, known as BET method. BET method is based on the adsorption of gas molecules on the surface of the porous medium [52]. Usually, inert gases are used as N_2 and Ar. The amount of the adsorbed gas can be correlated to the available surface of the material under investigation.

In addition, with the BET method, the pore size distribution graph can be extracted. Such a graph was presented earlier on figure 2.7. Through the pore size distribution graph one can extract the mean pore size, and evaluate if the material is micro-, meso- or macroporous, or a combination of them. Even for electrodes with subnanometer pores, beyond the resolution limits of microscopy, BET method is known to extract reliable results.

Chapter 3

Experimental

3.1 Ideal Electrode

In this section the ideal properties for an electric double layer capacitor electrode will be discussed in respect to their energy and power density based on the literature and the analysis of previous chapters.

3.1.1 Energy Density

As it is mentioned before, the two main electrode properties that affect the capacitance in EDLCs are the surface area and amount of pores with size comparable to the electrolyte ion size. Nevertheless, high surface area is not only the dominating factor but it has been shown that it is requirement. I.e. in [53] is shown that in electrodes with relatively low surface area and high concentration of ions in the electrolyte, the whole surface of the electrode was fully occupied by adsorbed ions in voltages lower than the maximum operating voltage of the electrolyte. Hence, the further increase of the voltage does not contribute to the capacitance and the stored energy on the electrode. They call this phenomenon "surface saturation". Furthermore, similar behavior is noticed when low concentration of electrolyte is used. In this case, all the ions are adsorbed on the surface and there are no more charges in the electrolyte to be attracted to the walls of the electrode, hence further increase of potential does not affect the capacitance and the energy stored.

In order to satisfy both needs (high surface area and narrow pores), electrodes with high porosity are used. By porosity is meant the ratio between the empty void (volume) inside the electrode and the total volume of the electrode. Higher porosity usually translates to higher specific surface area for porous materials. Another quantity used to describe porous materials is the pore size distribution. Which is the relevant amount of pores sorted by size. The pores can be divided into three categories according to their size, macropores ($\geq 50nm$), mesopores ($2 - 50nm$) and micropores ($\leq 2nm$). The specific capacitance experiences anomalous increase with pore sizes close to the ion size, so electrodes with narrow pore size distribution with high density of micropores are needed. Nevertheless, practically mesopores and macropores are needed since their contribution to the porosity is higher because of their bigger volume. In order to achieve the same porosity with only micropores the electrode walls between each pore must reduce drastically. The extreme decrease of wall thickness can cause hindering in the distribution of charge in the electrode[23]. This is similar to the charge depletion in low concentration of electrolyte, but for the solid electrode case. Similarly, the increase of the voltage will not increase the charge density in the electrode, hence it will not contribute to the capacitance. For the operating voltages of EDLC the minimum wall thickness is expected to be around $\sim 2nm$ [54].

However, if an electrode can be fabricated with narrow pore size distribution of micropores, high specific area and appropriate wall thickness, so surface saturation and charge depletion is avoided, it will be ideal. The optimum size for the pores depends on the ions of the electrolyte and the supporting electrolyte itself. It has been reported [39], that the molecules that create the solvation shell around the ions, strongly influence the optimum pore size.

Finally, the fact that the ion size and pore size of the electrode must be in precise agreement, suggests that the pore size of the positive and negative electrodes must be different. That is because of the asymmetry in size between anions and cations [31]. In addition, because the optimum pore size is between the solvated and the bare ion size it is nearly impossible to predict it a priori.

3.1.2 Power Density

As mentioned on chapter 2 the yielded power density of the electric double layer capacitor comes from the the cell resistance, R_{cell}, and the different contributions in the cell resistance have been investigated.

In order to minimize the diffusive resistance in the pores, shapes with low tortuosities are favorable. In addition, pores with bottleneck entrances also affect the diffusive resistance. Specifically, the ions are trapped inside the pores and are unable to escape through the bottleneck. This can be noticed by the shift of the potential of zero charge (PZC) in the CV graphs [43].

In addition, the diffusive resistance is affected by the pore size itself. Despite the fact that nanopores are favorable for high energy density, they cause increase in the diffusive resistance. For that reason the length (transport path) of the nanopores should be kept as short as possible for high power application. In terms of energy again, there is no use for macro- or mesopores. But in terms of power bigger pores improve the diffusion and can be used as ion highways or ion buffer reservoirs[43]. Because of the faster diffusion in them, the ions can gain an easy access to the nanopores where the diffusion is much slower.

In addition, the pure electric resistance, that comes from the conductivity of carbon material and the interface between electrode and current collector, must be kept low. Depending on the fabrication method both resistances can be tuned.

Note that since the thesis is focused on the solid electrode, the resistance contribution of the electrolyte will be disregarded.

3.1.3 Summary

EDLC electrode requirements:

1. Carbon walls thicker than $2nm$ for avoiding charge depletion in electrode.
2. High surface area to avoid ”surface saturation”.
3. Electrolyte with high ionic concentration to avoid charge depletion in electrolyte.

Ideal electrode properties:

1. Minimum electrode/current collector resistance/capacitance.
2. High surface area for increased EDL and capacitance.
3. Relative long macropores or mesopores to be used as ion buffer reservoir and ion highways.
4. Highly ordered electrode features and pores with low tortuosity for ease of diffusion.
5. Short micropores with size between solvated and desolvated electrolyte ions for achieving desolvation and superionic state.

3.2 Electrode Concept

Based on the aforementioned summary on the ideal properties an attempt will be made to fabricate an electrode that meets all the properties in the list.

Current collector (1) - In order to tackle the electrode/current collector interface resistance/capacitance it was decided not to use a current collector at all, at least in the "traditional" way. Usually, electrode and current collector consist of different materials. That is because for current collectors, metals with higher conductivity than carbon are used. But at the interface of carbon and metal resistance/capacitance is created. In the proposed electrode the current collector consists of thick layer of carbon. The thickness of that layer can be tuned so the total electric resistance will be reduced to meet the requirements. Electrode and current collector will consist of the same piece of material where not interface phenomena between them will exist.

Highly ordered macropores (2)(3)(4) - The electrode will consist of highly ordered relative long (micrometer scale) macropores (a few decades of nanometers wide). The macropores will be used as ion highways, and they will provide easy access of ions to the active area of the electrode. Since, highly ordered pores with low tortuosity are favorable, templated carbon techniques will be used. In addition, the macropores will provide high surface area.

Short nanopores (2)(5) - As described, nanopores are essential for the increased capacitance of the electrode due to desolvation phenomena. Short nanopores will be created on the walls of the macropores, by means of carbon activation. The activation parameters will be chosen for the creation of short pores, so the ion transport path will be kept to minimum. Finally, the activation of carbon will further increase the surface of the electrode.

3.2.1 Electrode Fabrication Parameters

Both templated carbon and activated carbon fabrication methods require a carbon precursor. Su-8 has been chosen as a precursor in our approach.

Su-8 - is a negative epoxy-based photoresist. Su-8 has chosen for several reasons. First, the film formation is a trivial process and films of thicknesses with submicrometer accuracy can be formed by spin coating. Second, the pyrolysis of Su-8 is well documented and can create carbon structures with high aspect ratios [55, 56, 57, 58]. Finally, Su-8 shrinks much less than other polymers and especially positive photoresists [55]. For our electrode Microchem® Su-8 2000 series was used. The manufacturer proposed parameters for soft and hard bake were used. In contrast, the exposure time was much higher than recommended. Specifically, 5 minutes of exposure used when the recommended time for the thickness used was less than one minute. This choice was made because extended crosslinking is needed prior to pyrolysis as described in [55].

Template - As it was mentioned before through the templating technique wide pores (a few decades of nanometers) and relative long pores(micrometer scale) must be created. For that reason a membrane structure was chosen, specifically Anopore membrane. Anopore is the commercial name for porous aluminum oxide membrane. The specific material was chosen because it is commercially available so there is no need to fabricate it from scratch. In addition, the membrane consists of relatively ordered cylindrical pores with very narrow pore size distribution. For the fabricated electrodes Whatman® Anodisc membranes used with average pore size 200nm and average wall thickness between pores of 50nm and membrane thickness of 60μm. A top view of the membrane is presented on figure 3.1. The membrane will be used as a template with three different ways that will be explained in the following section.

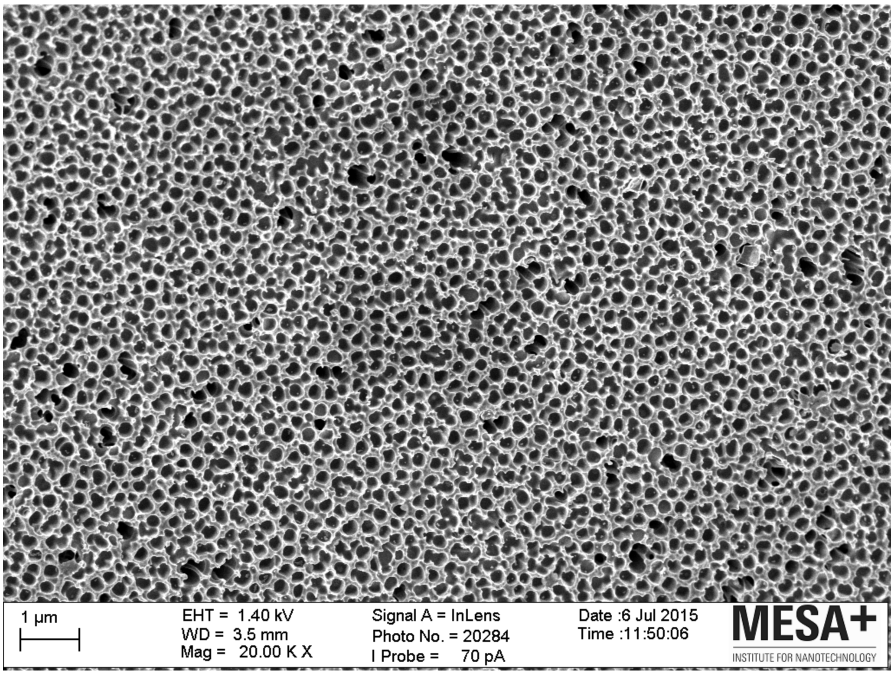

FIGURE 3.1: Top view SEM image of Anopore membrane. (Average pore size - $200nm$, Average wall thickness - $50nm$)

Pyrolysis - The parameters chosen for the pyrolysis based on article [55] and on our trial-and-error experiments. The pyrolysis took place in a tube furnace under 100% N_2 gas with flow $50ml/min$. The samples were heated from room temperature to 950^oC with a rate of $5^oC/min$. Annealing at this temperature for two hours follows and cooling down to room temperature with the same rate. Su-8 carbonizes under these conditions and results in conductive pyrolytic carbon. There is a significant vertical shrinkage for our samples in the range of 79%. The vertical shrinkage can be reduced according to [55] if forming gas ($95\%N_2$ $5\%H_2$) is used instead of pure N_2. Forming gas was not available in the used setup but in addition vertical shrinkage was not a critical issue in our case, hence, pure N_2 gas was used.

Carbon Activation - As described in chapter 2.3 there are two different ways of activation, physical and chemical. Despite the fact that chemical activation yields higher SSA at lower temperatures, it introduces metal ions into the carbon due to the activating agent. Those ions are hard to remove from the carbon lattice. In addition, physical activation is much simpler process, hence physical activation was chosen for our fabrication. Specifically, the already pyrolyzed electrodes were heated up under N_2 atmosphere to 900^oC and the the atmosphere switched to the oxidizing gas, namely CO_2 at a flow rate of $50ml/min$. The carbon is activated at this temperature for a specific period of time and then the atmosphere is switched back to inert gas and the samples cooldown. Based on [46] where the the samples were activated for different durations, two main results came out. When the samples were activated for 1 hour then they yield the higher capacitance per surface area (F/m^2) and when the samples are activated for 4 hours the result in the highest gravimetric capacitance (F/gr). For that reason these two activation times were chosen for our experiments. Once again, the activation took place in a tube furnace. In addition, when the optimal parameters are found, pyrolysis and activation can take place in a single experiment just by switching to oxidizing gas atmosphere after the pyrolysis is complete, before cooling down the sample. This reduces significantly the fabrication time and costs. With chemical activation such process is not possible since the carbon must be impregnated with activating agents prior to activation.

3.2.2 Fabrication Process

The fabrication process starts with the spin coating of Su-8 on a silicon substrate. Because the templated Su-8 will be removed from the substrate prior to pyrolysis, first a dicing foil (PVC film) is laminated on the substrate (Figure 3.2.2). The adhesion of the dicing foil is low on the silicon which makes the peal off of the Su-8 from the substrate trivial. The substrate is only used as a support for the spin coating process, through which the accurate control of the photoresist thickness is possible (Figure 3.2.3). The thickness of the Su-8 must be more than the thickness of the template ($60\mu m$) in order for the current collector to be created. For our experiments, $110\mu m$ thick layers of Su-8 were used, which creates a $50\mu m$ current collector. The current collector thickness can be higher if the reduction of electric resistance is needed. After the spin coating the aluminum oxide membranes are placed on top of the Su-8 (Figure 3.2.4). Capillary forces are strong enough to easily fill the $200nm$ pores in the membrane with Su-8 (Figure 3.2.5). When the membrane is filled it turns from white color to transparent. After that soft bake, UV exposure and hard bake follows. As mentioned before the soft and hard bake parameters (temperature and time) have been done according to the Su-8 manufacturer, but over exposure of the Su-8 for extended cross-linking was used.

The Su-8 layer is detached from the substrate which results in a freestanding $110\mu m$ film with an impregnated aluminum oxide membrane in it (Figure 3.2.6). At this point two different methods of templating followed.

On the first method the aluminum oxide membrane is etched away in KOH solution and a templated Su-8 layer is created (Figure 3.2.7a). After that the sample is pyrolized and results in the templated carbon electrode(Figure 3.2.8).

On the second method, the sample of figure 3.2.6 is pyrolyzed and carbon with the aluminum oxide membrane still impregnated in it is created. After that etching of the template in KOH solution follows and the final templated carbon electrode is created(Figure 3.2.8).

Despite the fact that the methods are the same, with the etching step in different order, the resulted electrode has completely different properties as it can be seen in the chapter 4.

In order to finalize the fabrication, activation of carbon follows with CO_2 physical activation with the parameters described before(Figure 3.2.9).

Following this process six different electrodes have been created. The electrodes that have been fabricated with the process step 7a on figure 3.2 will be called Type-A and the ones that have been fabricated with the process step 7b will be called Type-B. Each electrode of the two types have been activated for either 1 or 4 hours or not at all. Type A electrodes 1 hour, 4 hours and not activated are name Type-A-1h, Type-A-4h and Type-A-0h, respectively. Similarly we have Type-B-1h, Type-B-4h and Type-B-0h.

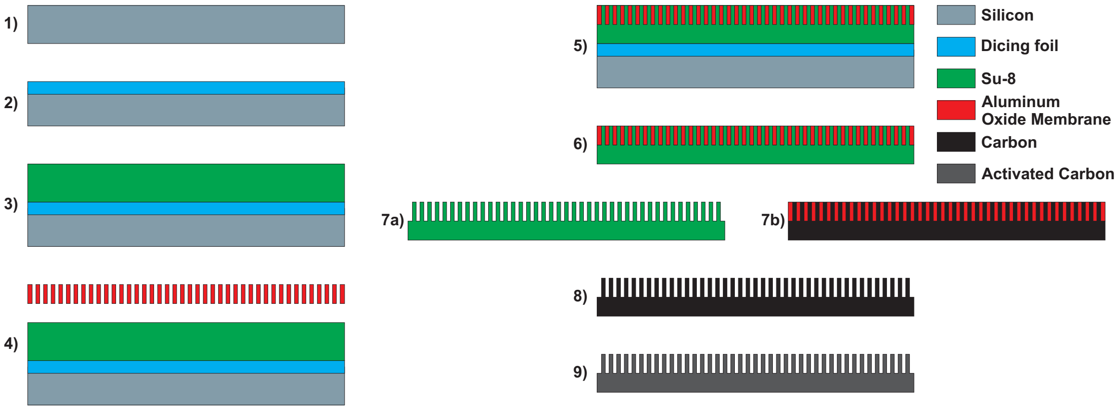

Figure 3.2: Schematic representation of the process flow. Materials are shown in the legend. (Not in scale))

3.2.3 Parylene-C electrode

In addition to the previously described electrodes, one more type of electrode has been created with the use of the same aluminum oxide membrane. But the template was used in different way. Specifically the membrane was coated uniformly instead of filling it. This way the pores of the membrane were left still open. The mebrane was coated with parylene-C film of $\sim 50nm$ in a SCS Labcoater® 2 PDS 2010 device. The samples were then pyrolized with the parameters described in [59] and then activated with similar parameters as the rest of the samples.

The fabrication process is shown in figure 4.13. Theoretically, the final electrode will have ordered pores with size of approx $100nm$, which will be used as ion highways since the diffusion in them will be easier than the micropores. On the other hand the pores will have a length of $60\mu m$ which will hinder the diffusion. The activation will create nanopores on the walls of the pores which will be used for the ion desolvation. The samples will be referred as Par-0h, Par-1h and Par-4h for the non activated, one hour activated and 4 hour activated samples, respectively.

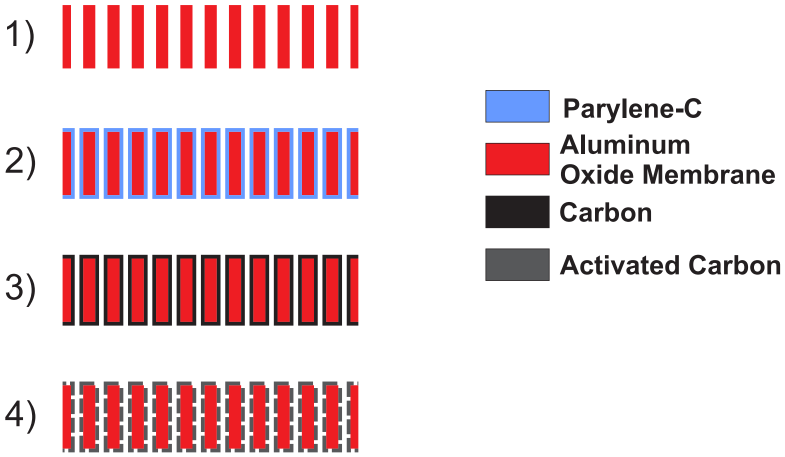

FIGURE 3.3: Fabrication process of Parylene-C Electrode. 1) Starting with anopore mebrane. 2) Uniform coating of $\sim 50nm$ parylene-C. 3) Transformation of parylene-C to carbon through pyrolysis. 4) Carbon activation

Chapter 4

Results & Discussion

In this chapter the results of our fabricated electrodes are presented and discussed. Three different methods were used to characterize these electrodes. First, Scanning Electrode Microscopy(SEM) was used to get an insight of the electrode morphology. Second, Cyclic Voltametry(CV) measurements was used in order to measure the capacitance of each electrode. Finnaly, Electrochemical Impedance Spectroscopy(EIS) was used to characterize the resistance and power density of the electrodes.

Unfortunately, the activation parameters proved not to be suitable for our electrodes which resulted in unsuccessful activation and the destruction of Type-A-1h and Type-A-4h electrodes. Nevertheless, a full characterization have been done in the survived electrodes. The results of the activated samples are based on a single sample of every type. Therefore, no information is available about the reproducibility of the results and needs to be investigated.

4.1 Scanning Electron Microscopy (SEM)

SEM images have been taken for all the samples and they are going be presented and discussed individually in the following sections.

4.1.1 Current Collector

As it was mentioned before, in our electrode current collector and active material will consist of the same material. The attempt to make such an electrode was partially successful. An example of the desired current collector is shown on figure 4.1.

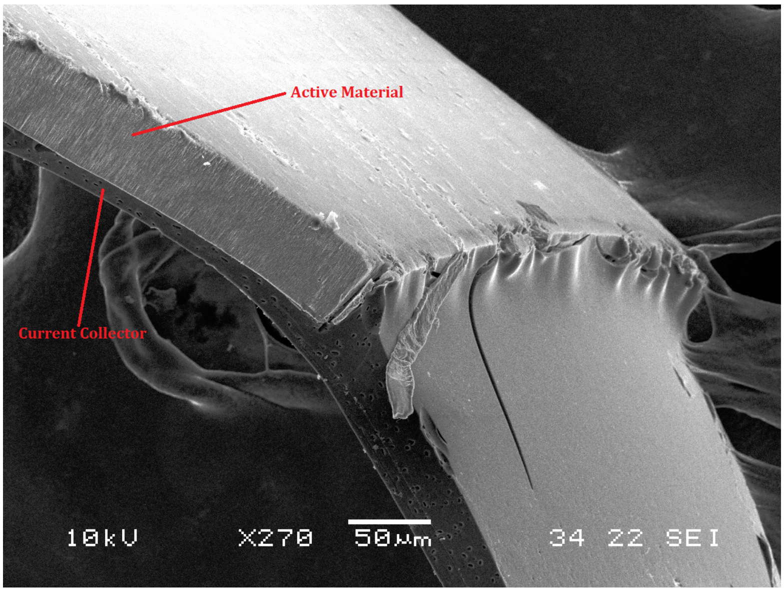

FIGURE 4.1: Crossectional SEM images of an electrode. (Dark part - Solid carbon current collector, Gray part - Active material)

As it can be seen, a thick layer (darker part) of carbon was formed under the active material (brighter part). In addition, the current collector extends further to a region where no active material is present. This is used for the electric contacts during the electrochemical characterization of the electrode.

The formation of the current collector was only partially successful, because only thin layer of carbon could be formed. When the thickness was increased the samples tend to crack under the stress of the pyrolysis. In addition, the thin layers were too fragile to attach to the clamper of the potentiostat's terminals for electrochemical measurements. So electrochemical results regarding the current collector will not be presented. Nevertheless, the concept of carbon current collector is proved that it can be fabricated, and with fine tuning of the pyrolysis process thicker current collectors will be possible.

4.1.2 Type-A-0h

For the fabrication of Type-A samples Su-8 have been templated with anopore membrane and the template was removed prior to pyrolysis. On figure 4.2 SEM images of the templated Su-8 are presented.

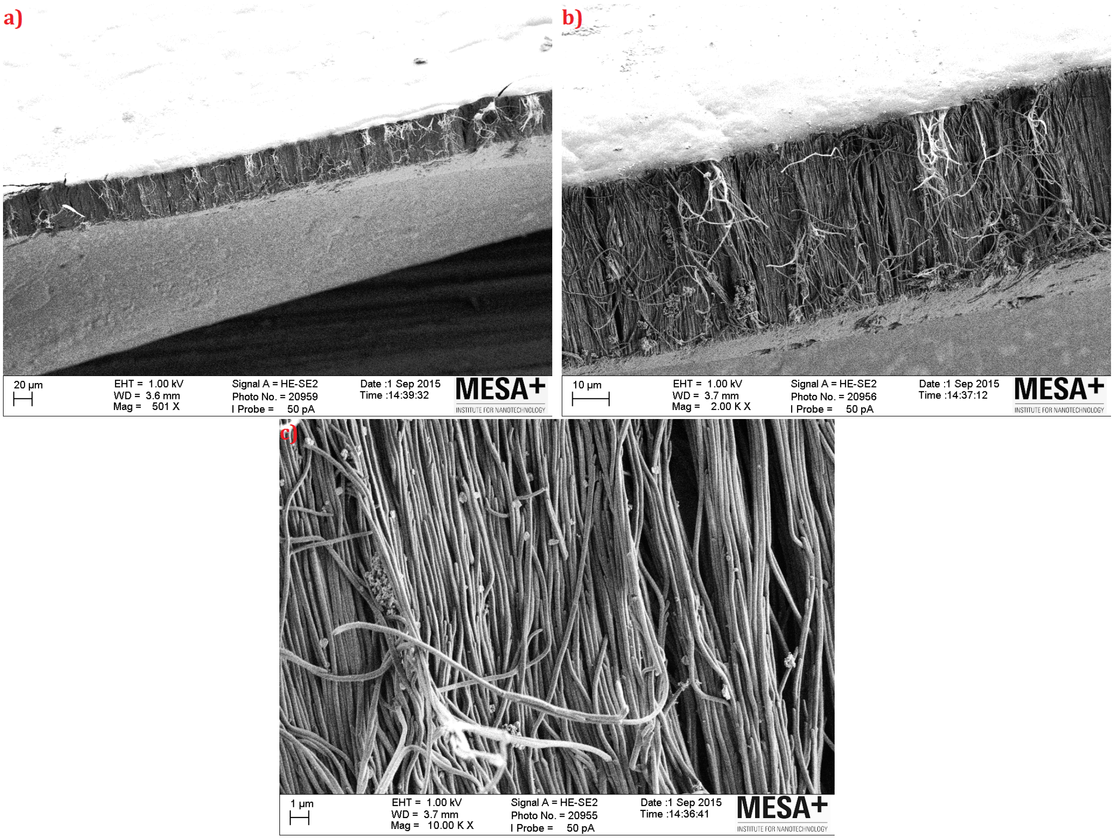

Figure 4.2: Crossectional SEM images of templated Su-8 for sample Type-A prior to pyrolysis. a) Low magnification crossectional image. The lower thick gray layer will serve as a current collector after pyrolysis. Su-8 fibers are in the darker area. b) Higher magnification crossection image, were the Su-8 fibers are visible. c) Close up on the fibers, where the spacing between them is visible.

The template seems to be completely removed and fibers of the size of the pores have been created. Su-8 fibers of approximate size of $200nm$ are visible in all images of figure 4.2. In figure 4.2.a the gray part under the fibers consists of a thick Su-8 layer which will serve as a current collector after the pyrolysis.

On figure 4.3 SEM images of the two samples after pyrolysis at 950^oC with a ramp rate of $1^oC/min$ are presented. EDX analysis showed that the samples are composed of carbon. In addition, no charging effects were noticed during SEM, which shows that the samples are conductive. On figure 4.3.a once again the current collector is visible as the lower gray part of the image. The single Su-8 fibers presented in the previous figure, are now attached to each other to form bundles. Nevertheless, in some cases there is spacing between the fibers as it can be seen in figure 4.3.d (along with some contamination).

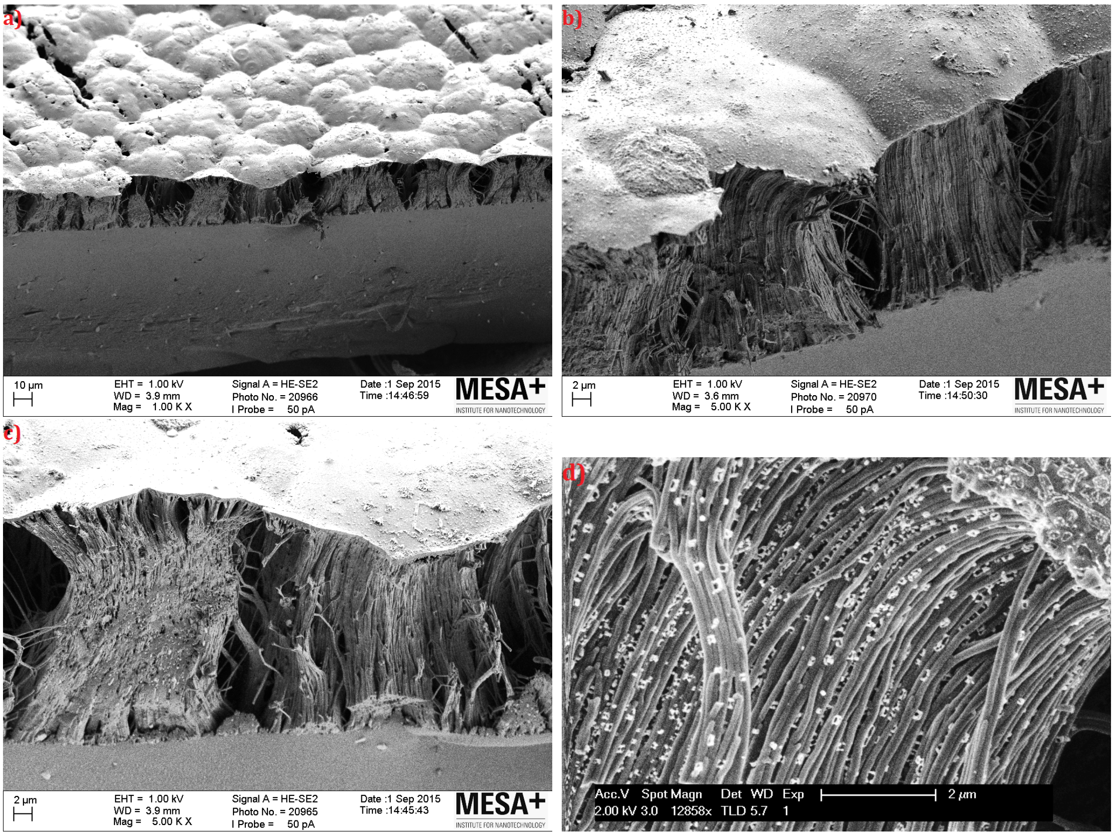

FIGURE 4.3: Crossectional SEM images of sample Type-A-0h. a) Low magnification crossection image. The lower thick gray layer will serve as current collector. In the middle the carbon fibers can be seen. And on the top bright part is the top surface of the electrode. Several big pores (a few micrometers) can be seen on the surface of the electrode. b,c) Higher magnification of the carbon fibers. The previously freestanding Su-8 fibers have now formed carbon fiber bundles. There is a wide range of pores/spacing between fibers and between bundles. d) A close up image on a bundle of fibers reveals that there also some micropores between fibers along with some contamination (bright spots).

On figure 4.4 a sample that was pyrolysed with higher temperature ramp rate (namely $5^oC/min$) is presented. Once again the fibers formed bundles, but the fibers seemed to attached more in comparison to the other samples.

On figure 4.5 SEM images of the top view of the samples (of figure 4.3) are presented. Bigger (micrometer scale - Figure 4.5.a , figure 4.5.b) and smaller (nanometer scale - figure 4.5.c) are present on the surface of the electrode. According to this, most of the surface of the electrode seems to be accessible to the electrolyte.

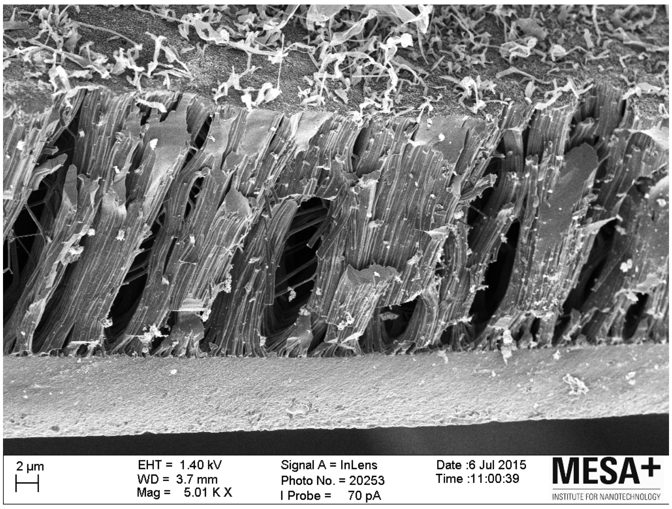

FIGURE 4.4: Crossectional SEM images of sample Type-A-0h pyrolized with higher temperature ramp rate($5^oC/min$). The merging of fibers is more obvious than the previous sample, and there is no pores/space between individual fibers.

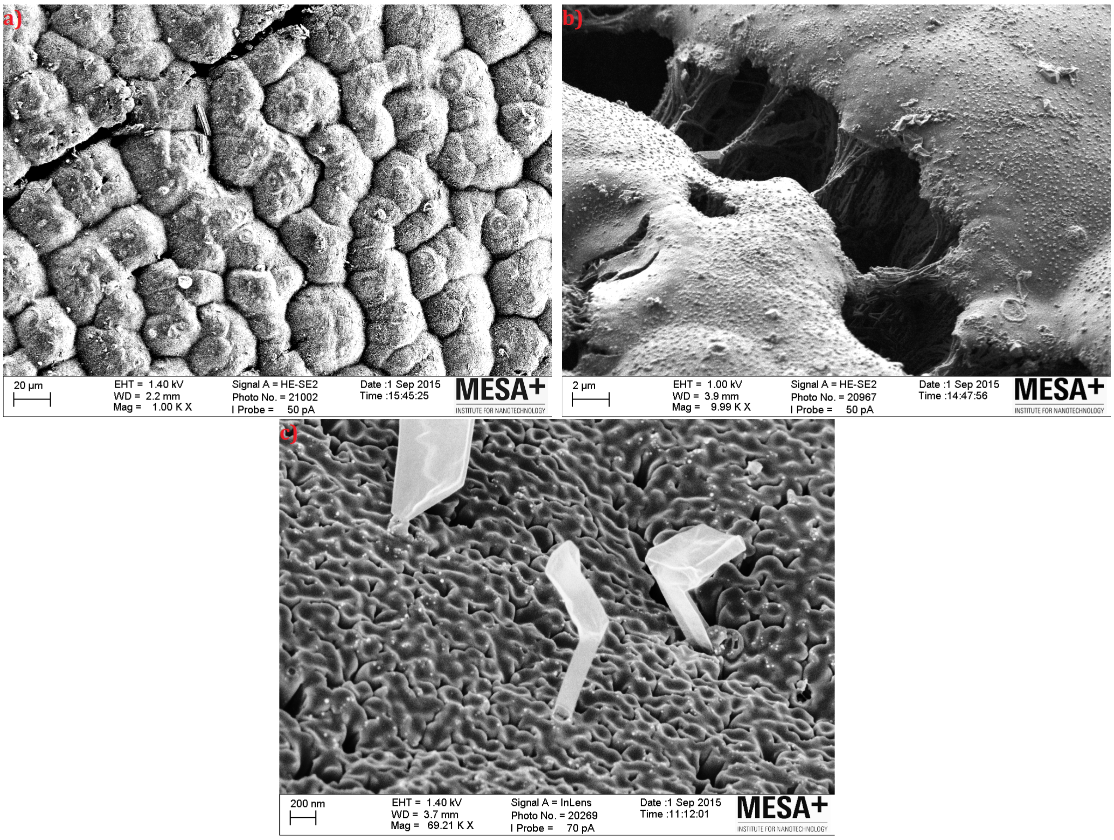

FIGURE 4.5: SEM images of top view of sample Type-A-0h. a) The low magnification image of the top surface of the electrode reveal that in many cases there are ridge-like pores of few micrometers in width between the bundles of fibers. b) A close up look on one of the ridge-like pore, and the carbon fiber network inside it. c) A high magnification SEM image of the surface of the electrode. Nanometer scale pores are visible.

4.1.3 Type-B-0h

In a similar fashion as previous, the image of the non-pyrollyzed sample was first taken. SEM images of the samples prior to pyrolysis are presented on figure 4.6. For the preparation of Type-B samples the anopore membrane was impregnated with Su-8 and pyrolysed without removing the template, in contrast to Type-A samples. The Su-8 fibers are still visible impregnated in the aluminum oxide membrane and at the breaking points they come out by bending and twisting. One can see how flexible the Su-8 is. Once again in figure 4.6.a the bottom thick layer will serve as current collector.

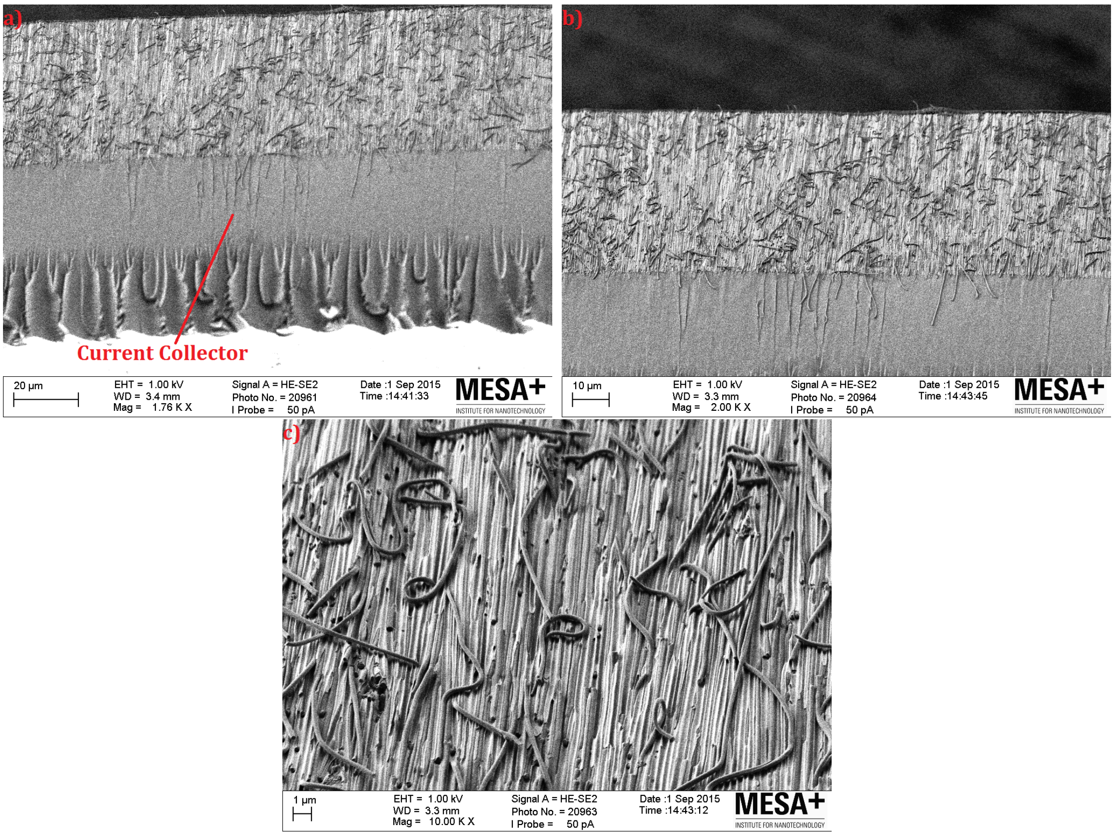

Figure 4.6: Crossectional SEM images of Type-B samples prior to pyrolysis. The samples consist of Su-8 and aluminum oxide membrane impregnated in Su-8. a) Low magnification image of a crossection. The lower gray layer will serve as current collector. Some defects are visible in the lower part of that Su-8 layer. The brighter part above the current collector is the anopore membrane filled with Su-8 b) A higher magnification on the membrane shows the Su-8 fibers. c) A close up on the fibers coming out of the template at the breaking point.The fibers are almost perfectly cylindrical and of $\sim 200nm$ in width.

After pyrolysis all samples cracked and broke in approx. $1mm^2$ pieces. This is because of the miss-match in the shrinkage of the two materials. Aluminum oxide experiences only thermal contraction and expansion and in contrast Su-8, which during carbonization process shrinks. Specifically the current collector shrank from $\sim 55\mu m$ to $\sim 13\mu m$. This corresponds to a shrinkage of 76.3% close to the value of 80% that was previously report for pyrolysis under pure N_2 atmosphere [55].

On figure 4.7 crossectional SEM images of the pyrolyzed sample Type-B-0h are presented. On the figure 4.7.a the curvature of the sample is apparent even in the SEM images. This shows the amount of stress introduced by the shrinkage miss-match between the materials. On the right image with higher magnification one can see the crossection of single fibers. Before pyrolysis the fibers where non-porous. After pyrolysis the fibers where unable to shrink vertically so they formed a sponge-like structure.

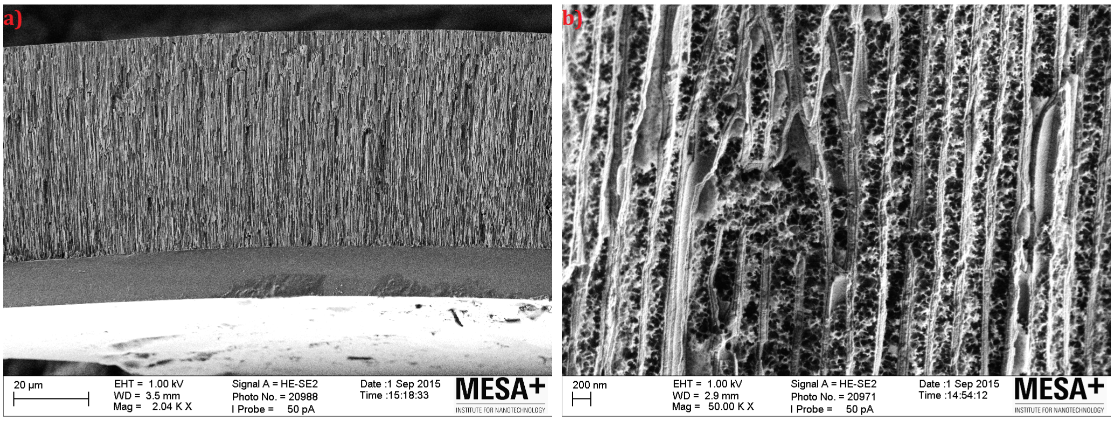

Figure 4.7: Crossectional SEM images of Type-B-0h samples. a)Low magnification image. Lower solid gray area is the current collector, which shrank by approx. 80% after pyrolysis. The curvature of samples shows the amount of stress that is involved due to the shrinkage of Su-8 during carbonization. b) A high magnification image on the walls shows that the solid Su-8 fibers turned into a sponge-like carbon attached to the aluminum oxide walls.

Despite the fact that this sponge like structure is valuable since it enhances the surface area, it is not accessible to the electrolyte. The etching of the template was not possible since carbon had uniformly covered it. On figure 4.8 a closer look at the walls and the top part of the electrode is presented. The whole surface is covered with a few nanometers of solid carbon. And the aluminum oxide walls have a solid layer of carbon around it.

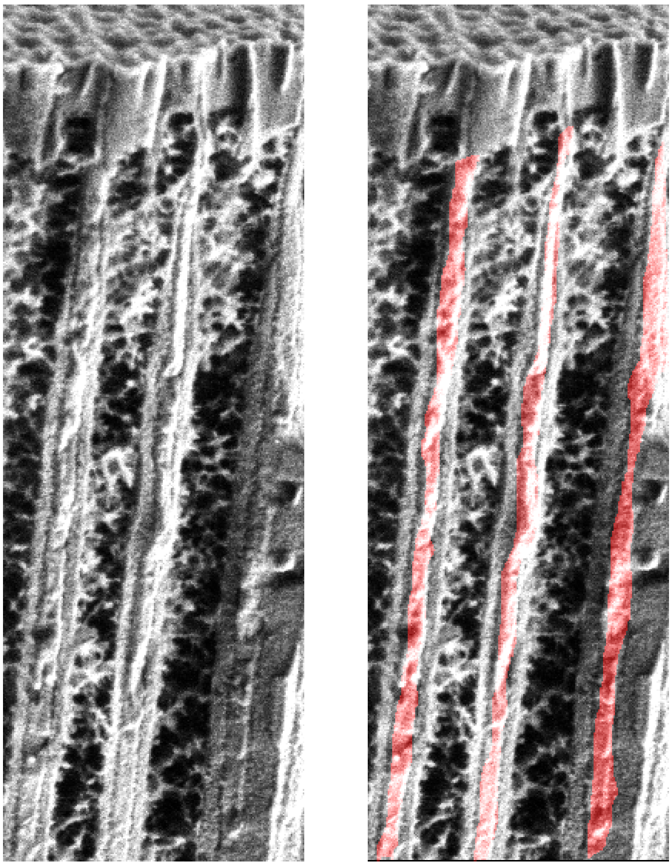

Figure 4.8: SEM image of Type-B-0h. Aluminum oxide is marked with red in the right image and grayscale features are carbon. The sponge-like carbon features are again visible. On the top of the electrode a solid layer of carbon has formed which protects the aluminum oxide membrane from being etched.

On figure 4.9.a SEM image from crossection under angle of the electrode shows some roughness on its surface. On figure 4.9.b the same roughness is visible from the top view SEM image. The top surface has only roughness and no pores can be seen down to the resolution of SEM. And on figure 4.9.c a bottom view of the electrode (current collector surface) is presented. On the current collector some fiber like features have been created. The material of the fibers is unknown. The carbon surface is non-porous.

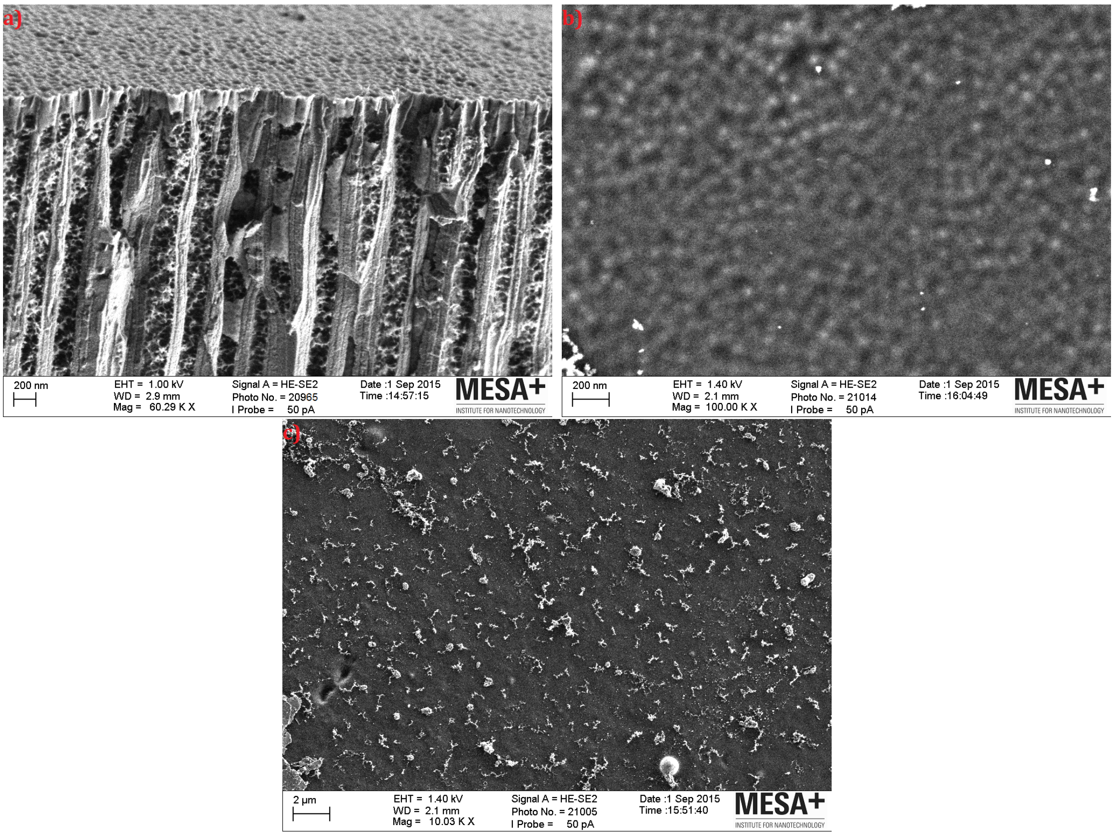

FIGURE 4.9: SEM image of Type-B-0h. a) Crossecion image under angle shows the roughness of the surface. b) Top view of the electrode. Once again the roughness is visible and no pores are present down to the resolution of the SEM microscope. c)Bottom view (surface of the current collector). There is some random roughness coming from the Su-8 defects but no pores are present. In addition some fiber-like features are present made of unknown material.

4.1.4 Type-B-1h

Type-B-1h is the sample that was activated for one hour in CO_2 atmosphere at 900^oC. Four SEM images are presented on figure 4.10. The first remark that should be made is that activation only occurred on the surface of the electrode. This can be deducted by looking the crossection images. The structure inside the pores is completely identical to the non-activated sample. The second remark is that the activation was not uniform. In all images one can see areas with different shading. The darker areas were activated more. But once again the aluminum oxide was not exposed to the etching medium hence the removal of the template was once again impossible. This can also be seen in figure 4.10.c.

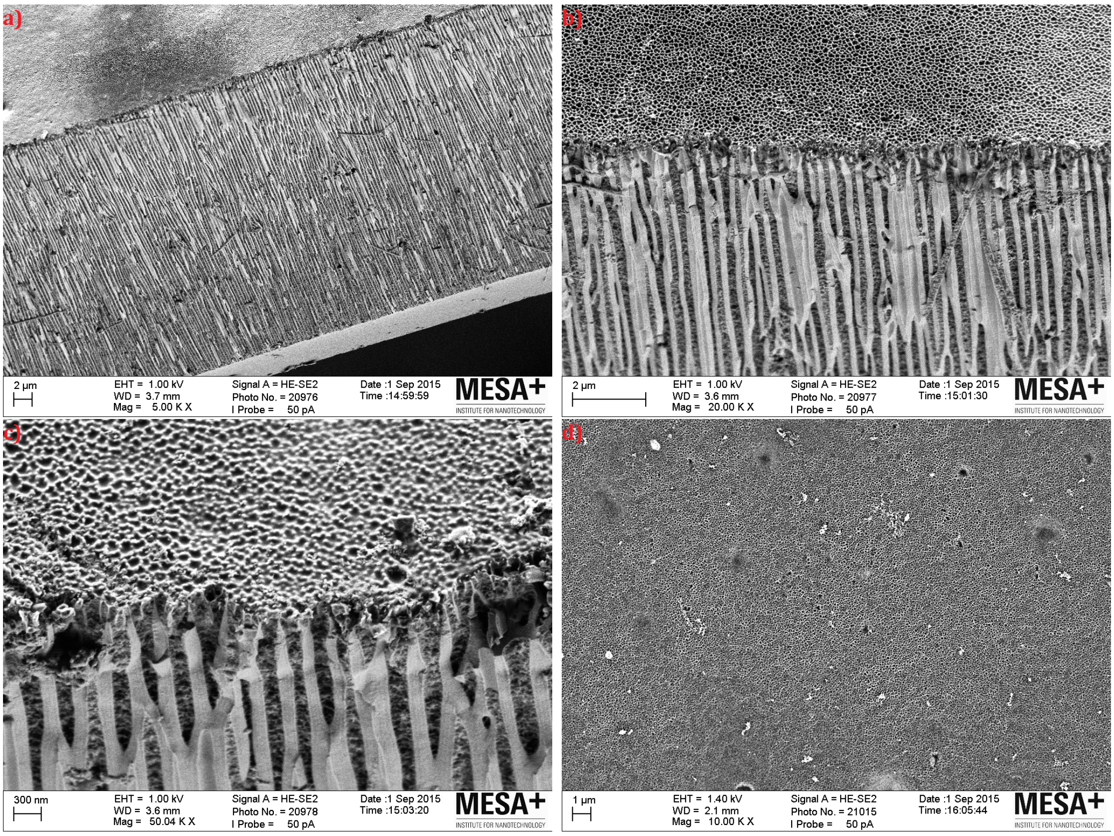

FIGURE 4.10: SEM image of Type-B-1h. a)Low magnification crossection images under angle. A thin gray layer on the bottom side of the image is the current collector. The aluminum oxide membrane filled with carbon is above the current collector. On the top side of the image where the surface is visible, different shading shows different level of activation. b,c) Higher magnification image at the edge between side and surface of the electrode. The sponge-like features are unaffected from the activation process. In addition, the aluminum oxide membrane is still not exposed from the top side. Again different level of activation can be seen on the surface of the electrodes (image b - Difference in shading between top left and top right of the image.) d) Top view of the electrode. Once again different activation areas are visible. Samples Type-B-1h have higher roughness than the unactivated sample.

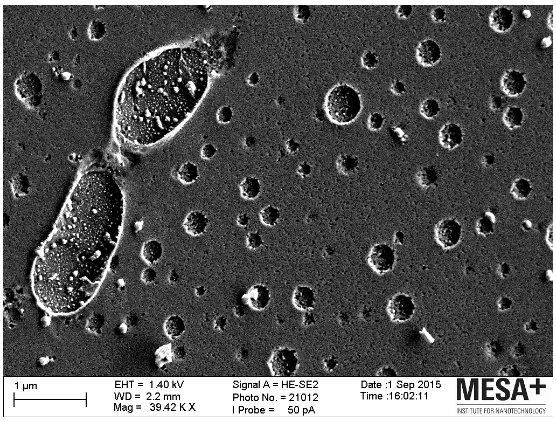

FIGURE 4.11: SEM image of bottom view of Type-B-1h. The current collector have been partially activated creating crater-like features and pores.

On figure 4.11 a SEM image is presented of the bottom view. There are activation areas which created crater-like features and pores on the current collector.

4.1.5 Type-B-4h

The results are similar to the sample Type-B-1h. The activation was more severe on some areas than others. Once again the activation had no effect on the carbon inside the pores. Whereas, almost the whole current collector have been activated/removed, since only but a few hundreds of nanometers are left. The top layer of figure 4.12.a is all that is left from the current collector. The current collector has the look of an expected activated carbon, with a wide range of pores. At the breaking points the current collector was pealed off (4.12.a and b). Figure 4.12.c and d) show a top view(c) and bottom view(d) of the electrode. Figure 4.12.c shows areas with higher and areas with lower activation since a change in shade is noticed. Figure 4.12.d once again shows the activated current collector with a wide range of pore size pores. Finally the figure 4.12.e shows the top of the electrode with two different detectors. On (e1) the back-scattered electron detector was used which shows a contrast difference depending on the material density. The bright areas are aluminum oxide and the darker areas carbon. On right image(e2) the secondary electron detector has been used which shows more the surface geometry. Despite the fact that the aluminum oxide seems exposed, once again was unable to be removed. The most reasonable explanation is that there is still a few nanometers of carbon on top of it which protects it from the etchant.

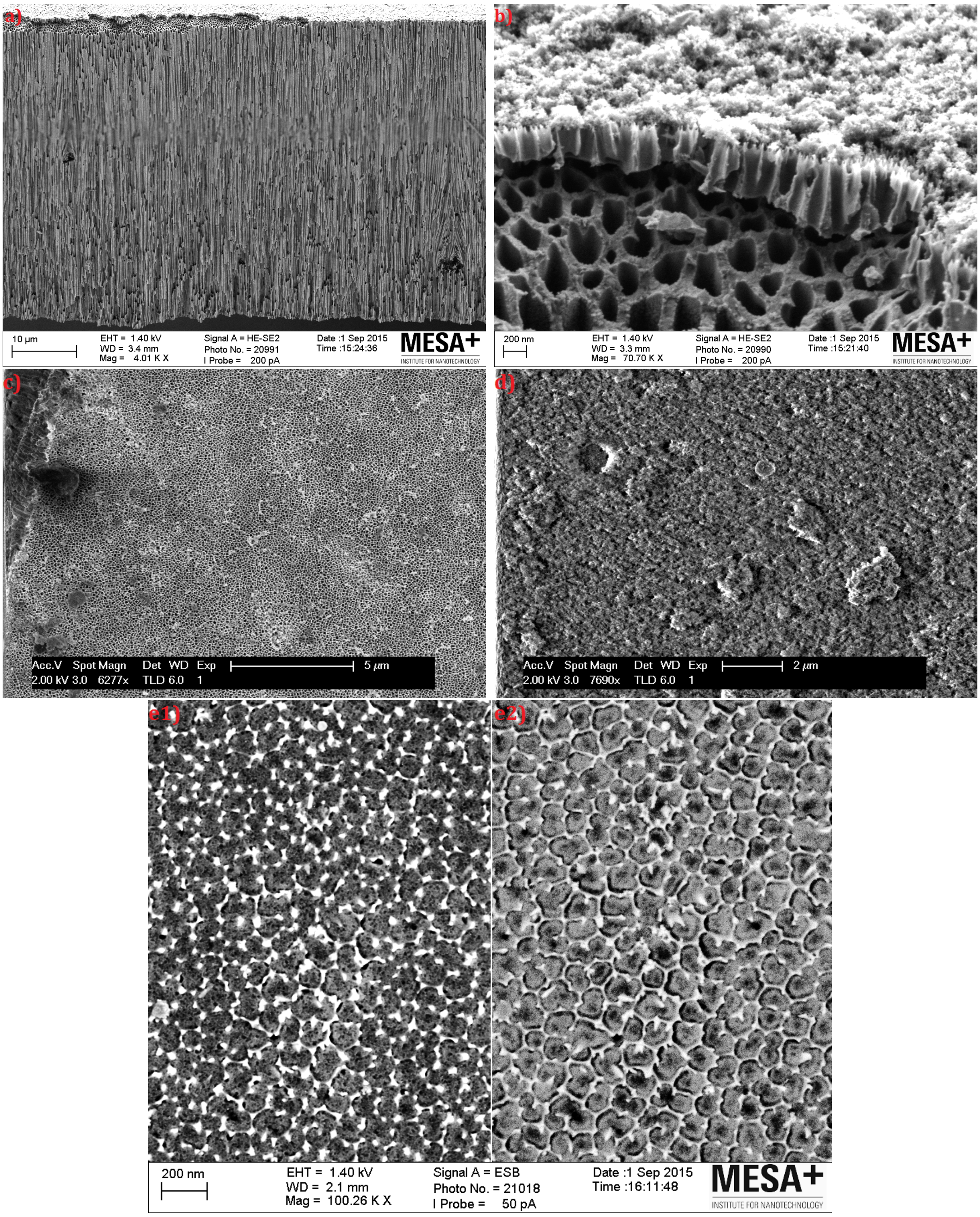

FIGURE 4.12: SEM image of Type-B-4h. a) Crossection view of the electrode. Higher magnification crossection images on the pores showed exactly the same sponge-like structure of carbon. The activation does not affect the carbon inside the pores. The electrode is upside down so the top part of the electrode is the current collector. b) High magnification image of the current collector. The current collector is fully activated and it is pealed of at the breaking points. c) Top view of the electrode. Once again different levels of activation are noticed. d) Bottom view (current collector surface) of the electrode. The current collector has a typical view of AC material. In both b and d images pores with wide range of width can be seen. e1) Top view SEM image with back-scattered electron detector. The different in brightness shows difference in material density. Brighter spots are aluminum oxide and darker spots are carbon. e2) Top view SEM image with secondary electron detector which shows the surface geometry.

4.1.6 Par-0h

The anopore membrane was coated with a $\sim 50nm$ parylene-C film and then pyrolysed. Crossection and top view SEM images have been taken and presented on figure 4.13. On the top images(a,b) the top view is presented. The sieve like structure has been created. Notice that the pores of the sieve are smaller than $200nm$ which is the average pore size of the membrane. The crossection view (lower images) does not reveal any significant information.

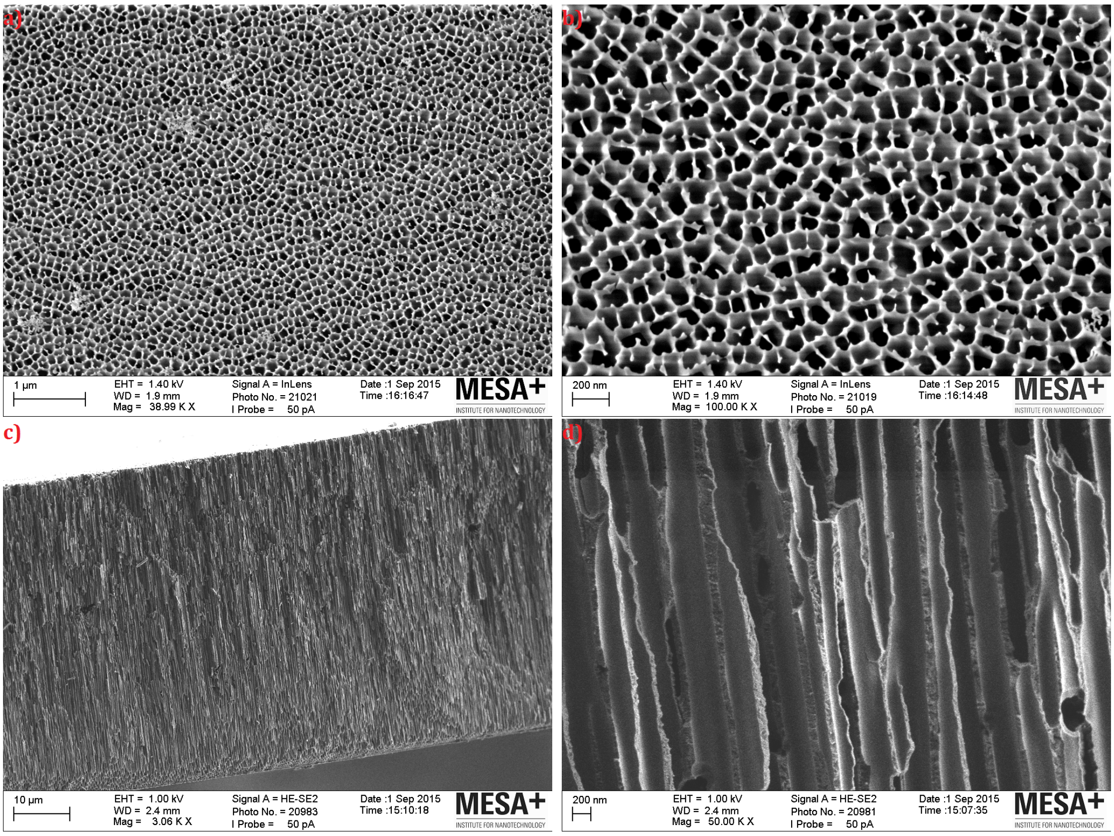

FIGURE 4.13: SEM image of Par-0h sample. a,b) Top view images with low(a) and high(b) magnification. Carbon structures create pores with size smaller than $200nm$, which is the size of the pores of the membrane. c,d) Low (c) and high(d) magnification cross-sectional images. The electrode looks similar to the bare membrane.

Only at extreme magnification some more information can be seen. Such an image is presented in figure 4.14. On this image one can see the different shades between materials. The different material is shaded with red color in the right image. Another remark about this image is the relevant roughness or porosity on the walls of the pore.

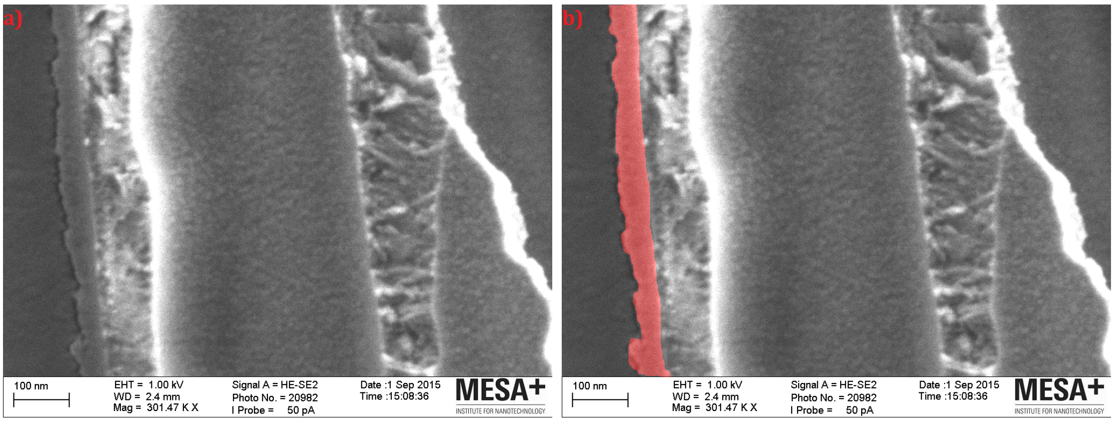

Figure 4.14: High magnification crossectional image of Par-0h. On image (b) carbon is marked with red color. In addition some roughness or pores with size beyond the resolution of the SEM are present on the surface of the electrode.

4.1.7 Par-1h

For the Par-1h sample which was activated for 1 hour cross-sectional images did not show any difference to the Par-0h sample. A top view SEM image is presented on figure 4.15. The pores became wider and rounder compared to the previous sample. The activation removed some of the carbon and widen the pores.

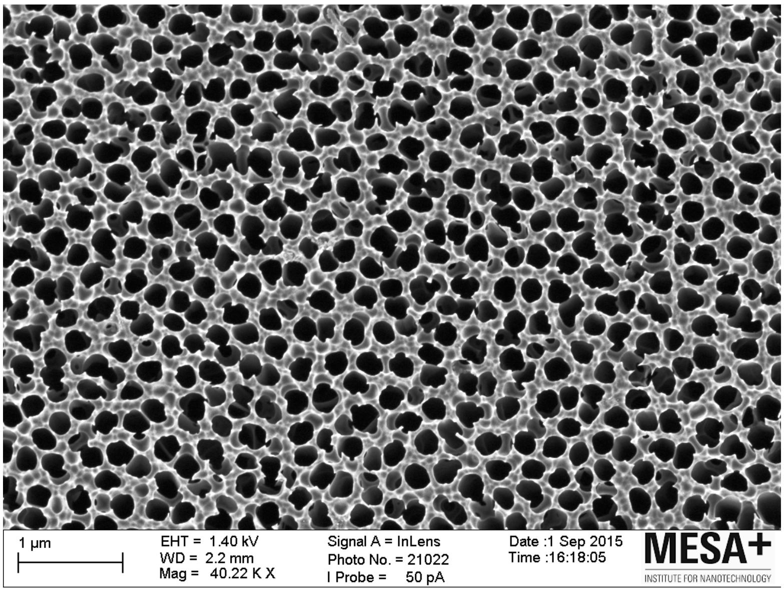

Figure 4.15: Top view of Par-1h sample. The pores became wider and rounder compared to the unactivated sample.

4.1.8 Par-4h

Par-4h samples were activated for 4 hours in CO_2 atmosphere. Similarly to the previous sample the cross-sectional images reveal no information. The top view (figure 4.16) shows that the pores became slightly wider and rounder. It looks similar to the bare membrane. Nevertheless the aluminum oxide template is still covered with carbon since all the samples were left in high concentration KOH solution for several days which would have etched aluminum oxide, if it was exposed.

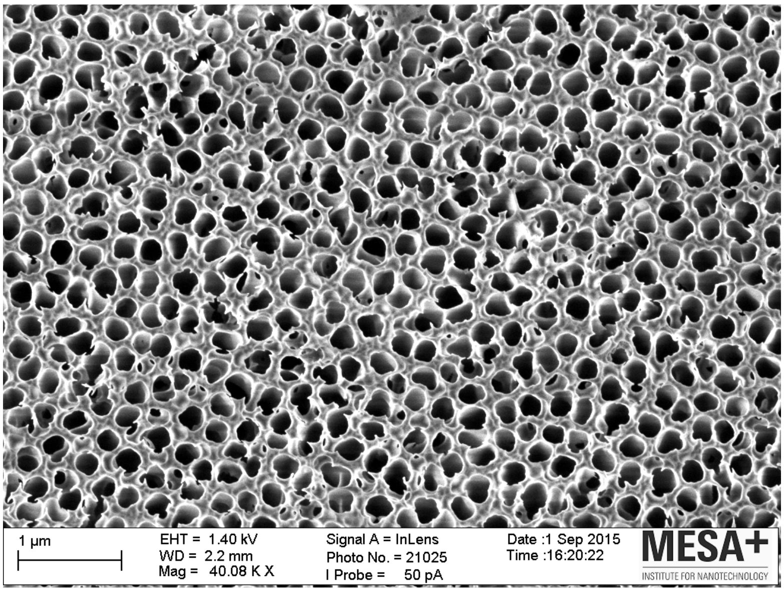

Figure 4.16: Top view of Par-4h sample. The pores became smoother and rounder than sample Par-1h.

4.2 Cyclic Voltametry (CV)

All the electrochemical experiments took place with a SP-300 Bio-Logic® Potentiostat. Saturated KCl solution ($4.82M$) was used as electrolyte. Three electrode potentiostat configuration was used. The active material created was attached on a 99.9% graphite rod with a carbon/graphite ink from Gwent Group. The active material, carbon paste and graphite rod was used as the working electrode. As counter electrode a $23F$ Kynol activated carbon fabric was fabricated. The counter and working electrode behave as two capacitors in series. The measured capacitance (C) of such system equals to:

$$\frac{1}{C} = \frac{1}{C_{WE}} + \frac{1}{C_{CE}},$$

were C_{WE} is the working electrode's capacitance and C_{CE} is the counter electrodes capacitance. Only the working electrode's capacitance must be measured. In order to minimize the effect of counter electrode's capacitance in the measurement, the counter electrode should have much higher capacitance than the working electrode. For that reason, the working electrode kept under $1F$ in capacitance. If an $1F$ capacitor is connected in series with a $23F$ one, the total capacitance will be $0.9583F$. As reference electrode a Ag/AgCl electrode was used.

All the electrodes exhibit a butterfly shaped CV curve for several scan rates. An example of a CV curve is presented on figure 4.17.

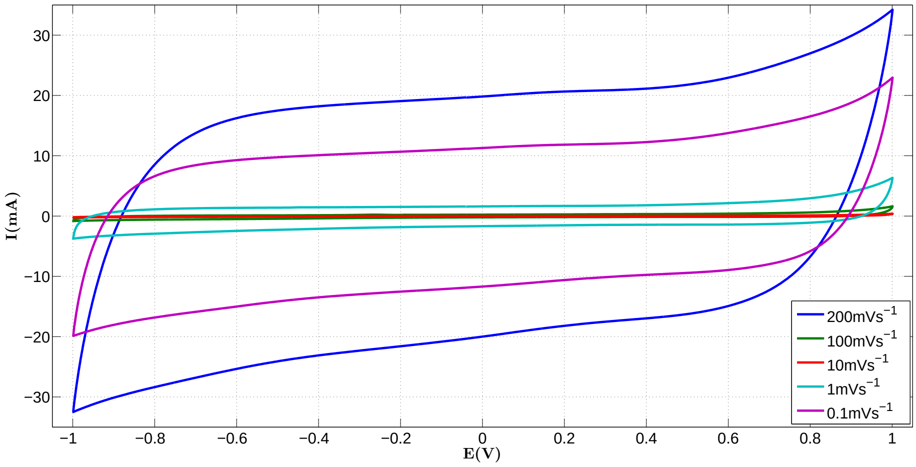

Figure 4.17: CV curve of Type-B-4h. Scan rates are marked in the legend. The CV curve keeps the butterfly shape for all scan rates. (Electrolyte - Saturated KCl).

On figure 4.18 CV curves of all samples are presented in the same scan rate. Note that the current axis has been normalized over the weight of the electrode for direct comparison of the electrodes.

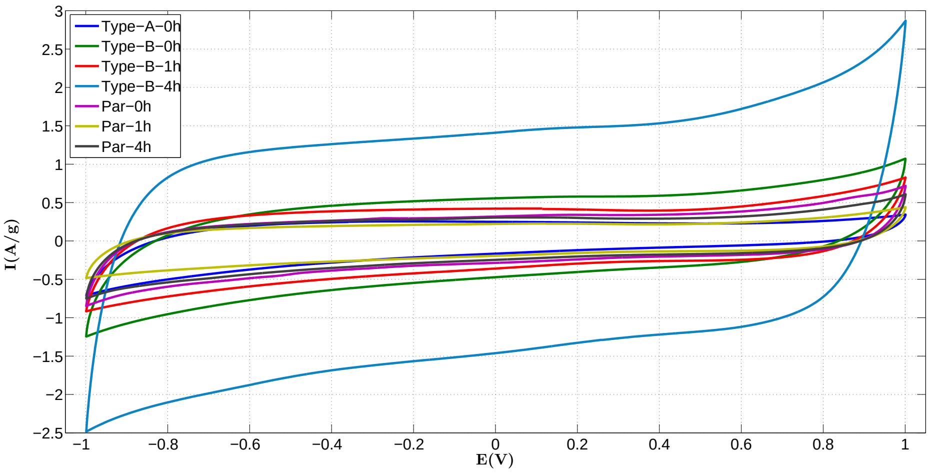

FIGURE 4.18: CV curve of all the samples. All samples show a butterfly shaped curve and the higher capacitance comes from sample Type-B-4h.(Electrolyte - Saturated KCl, Scan rate - $100mV/s$)

One can see that most of the electrodes have similar behavior with the exception of Type-B-4h which capacitance is much higher. In order to quantify the difference between the electrodes the capacitance have been extracted from the CV curves by averaging the current over the whole potential window and dividing by the scan rate. This method has been mathematically described in chapter 2.4. The resulted gravimetric capacitance (F/g) is summarized in table 4.1.

	Gravimetric Capacitance						
Scan Rate	Type-A-0h	Type-B-0h	Type-B-1h	Type-B-4h	Par-0h	Par-1h	Par-4h
200 mV/s	$1.81F/g$	$2.65F/g$	$4.11F/g$	$10.75F/g$	$2.77F/g$	$1.83F/g$	$2.56F/g$
100 mV/s	$2.27F/g$	$4.10F/g$	$5.35F/g$	$14.63F/g$	$3.28F/g$	$2.17F/g$	$2.90F/g$
10 mV/s	$4.80F/g$	$6.60F/g$	$10.54F/g$	$23.38F/g$	$5.54F/g$	$3.39F/g$	$4.85F/g$
1 mV/s	$9.34F/g$	$12.11F/g$	$20.83F/g$	$38.37F/g$	$15.95F/g$	$7.81F/g$	$12.77F/g$
0.1 mV/s	$32.93F/g$	$36.42F/g$	$50.30F/g$	$84.63F/g$	$106.20F/g$	$29.60F/g$	-

TABLE 4.1: Gravimetric capacitance of all electrodes in saturated KCl electrolyte in potential window from $-1V$ to $1V$.

The results of gravimetric capacitance with extremely low scan rate (i.e 0.1 mV/s) have been separated from the rest of results. On this scan rate the current was extremely low (in the nA scale) which resulted in the deformation of the graphs from the rectangular shape, due to noise effects. Thus, the results are not considered reliable. One can notice the anomalous increase in capacitance at that scan rate (e.g. Par-0h electrode in table 4.1). In order to verify the results at this scan rate, electrodes with more active material must be used in order to increase the capacitance and hence the current. The increased current will be less subjuctable to noise. In addition, EDLCs are used in application were the charge and discharge occurs in seconds or minutes, thus extremely low scan rates have no practical applications.

The general trend is that the capacitance is increasing when the scan rate decreases. That is because there is more time for ions to diffuse into the pores increasing the charge in EDLC.

The results also show that the best behavior in terms of capacitance comes from the Type-B-4h sample which exhibits up to $38.37F/g$ at $1mV/s$ in saturated KCl electrolyte.

4.2.1 Potential Window and Pseudocapacitance

The aforementioned results came from CV scans from $-1V$ to $1V$. A strange phenomenon was noticed during the CV experiments when the potential window was changed. Specifically, the capacitance decreases with decreasing the potential window. This is due to the fact that with increasing potential the capacitance increases since the EDL squeezes under the higher electric field and decreases the distance between ions and electrode surface. This explains the non perfect rectangular shape of the CV curve, that an ideal capacitor would show. The EDL squeezing does not explain the noticed phenomenon shown in figure 4.19. One would expect that the graphs with different potential window should overlap on the same potential no matter the potential window. But this is not the case. The same behavior is noticed for all electrodes. at all scan rates, hence it is not a time depended.

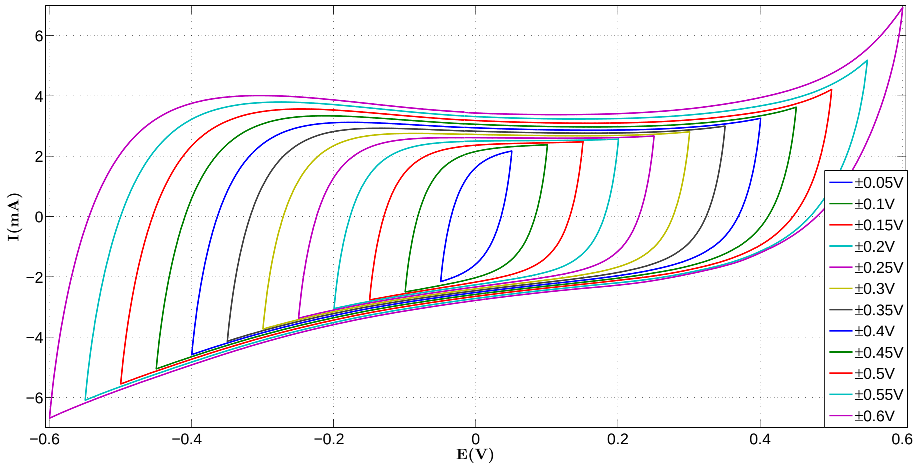

FIGURE 4.19: CV curves of the same electrode for different potential windows. The potential window is shown in the legend. Scan rate - 50mV/s. The average current and the current at zero potential decreases with decreasing potential windows, so does the capacitance.

The graphs overlap when only positive or negative scans take place. On the positive scan the graphs overlap from the top side and on the negative scan they overlap in the bottom side. Those CV curves are presented on figures 4.20 and 4.21.

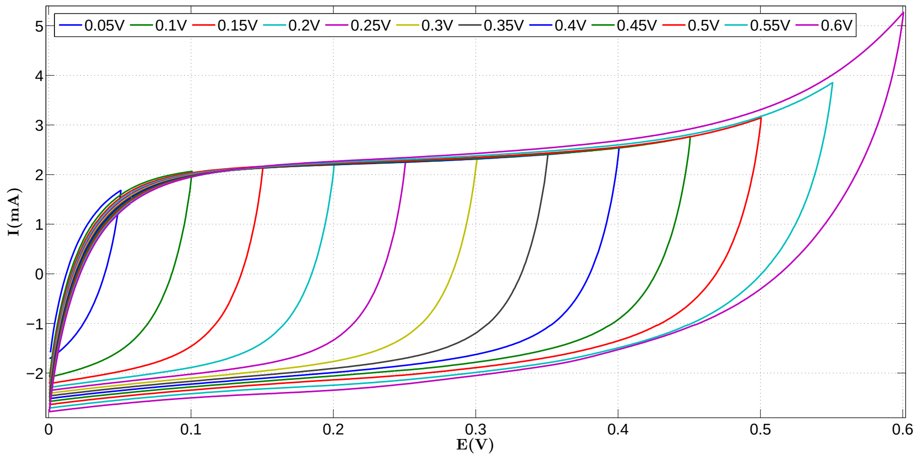

FIGURE 4.20: Only positive scan CV curves of the same electrode for different potential windows. The top part of the curves overlap regardless the potential window, but in the bottom part the effect of pseudocapacitance is obvious. The upper potential limit is shown in the legend. Scan rate - 50mV/s.

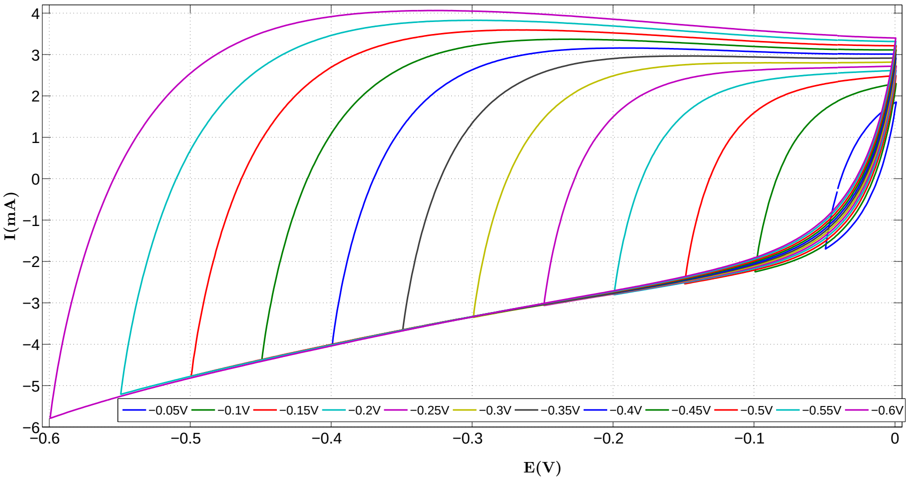

FIGURE 4.21: Only negative scan CV curves of the same electrode for different potential windows. Similar to the positive case, the curves overlap in the bottom side regardless the potential window and the pseudocapacitance currents differ on the top side. The lower potential limit is shown in the legend. Scan rate - 50mV/s.

If the current at zero potential (ZPC) is plotted versus the potential window, one can see their dependency. The curves for $0V$ to $0.05V$ and $-0.05V$ to $0V$ potential windows tend to break the pattern of overlapping. It is most likely that the scan rate is two high for this potential window. It takes one second to get to max/min potential and the whole cycle is two seconds. The ZPC versus potential window graphs are presented on figures 4.22 and 4.23 for positive and negative scan respectively.

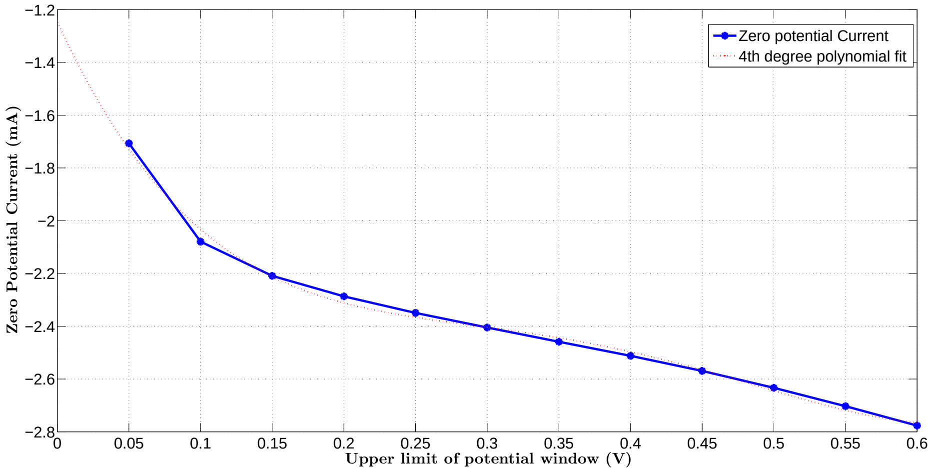

FIGURE 4.22: Zero potential current vs potential window for positive scan. The relation between potential window and zero potential current is linear down to $0.01V$. The red dotted line represent the 4th grade polynomial fit. The point were the fitting line intercepts the y-axis(zero potential window) gives the pure EDL current.

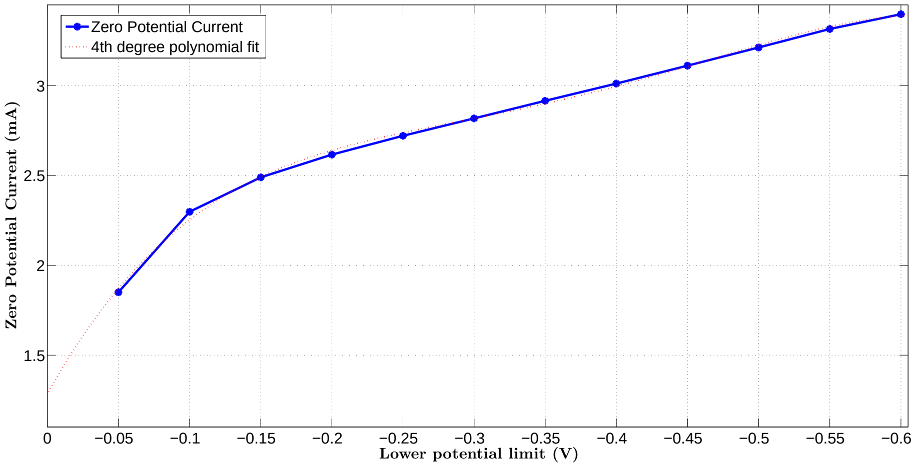

FIGURE 4.23: Zero potential current vs potential window for negative scan. The graph is symmetric to the positive scan. The red dotted line represent the 4th grade polynomial fit. The point were the fitting line intercepts the y-axis(zero potential window) gives the pure EDL current.

Since the phenomenon depends on the potential window, by extrapolating the fitted line to zero potential window the effect of the phenomenon can be excluded from the current and the capacitance.

The question that remains is "What causes this phenomenon?"
The answer is pseudocapacitance. On figure 4.24 four CV curves from previously reported pseudocapacitors are shown [60, 61, 62, 63]. The curves deviate from the rectangular shape but the same dependency of the capacitance to the potential window is noticed.

Pseudocapacitance is potential depended and there are several factors that contribute to capacitance. First factor is the electrosorption of ions of the electrolyte in the inner Helmholz plane of the double layer. This is a possible factor in our application. A second factor is redox reaction of metal oxides. This is unlikely in our case since there are no metal oxides. There is aluminum oxide in some electrodes but it is not exposed to the electrolyte. If it were, it would have been etched during the etching of the template. In addition, Type-A-0h has no aluminum oxide at all, and same pseudocapacitance is noticed. A third factor is the oxidation of the electrode, which is also unlikely since carbon is quite chemically inert. A fourth factor that can cause faradaic currents and hence pseudocapacitance due to the decomposition of the electrolyte. This is also not possible in our case since the pseudocapacitance is also noticed for very low potentials (down to $0.05V$) where the electrolyte's electrochemical stability is not questioned. A fifth factor is the exchange of charges between electrode and electrolyte in the form of functional groups on the surface of the electrode. On carbon electrodes several different functional groups exist, depending on the fabrication process. Groups such as carboxyls and quinone type have been reported for carbon electrodes[64, 65, 66]. An exchange of charges in form of OH^- or H^+ is possible. In order to verify if this is case for the proposed electrodes, CV measurements in the same electrolyte with varying pH should be taken.

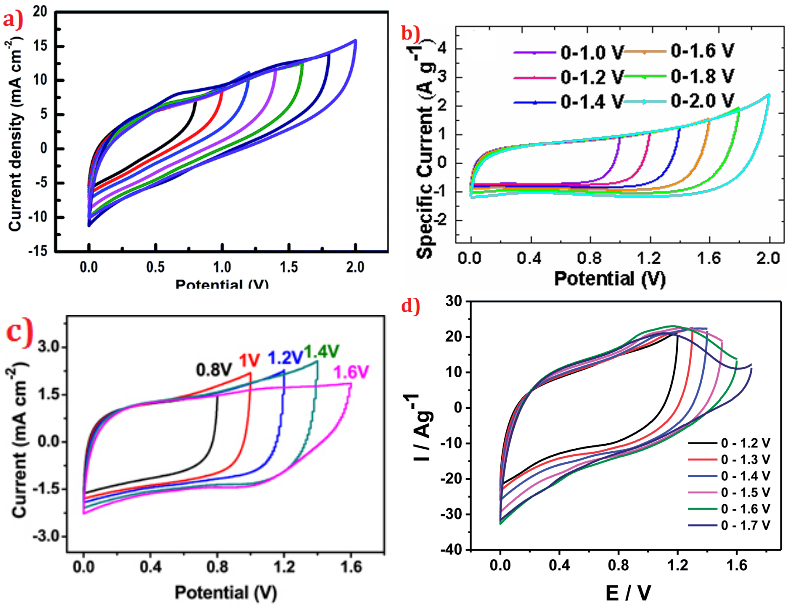

FIGURE 4.24: Typical CV curves of pseu-docapacitors. The butterfly CV curve is distort in some cases but the pseudocapacitance dependency on potential window is obvious in all cases.(a) - [60], b) - [61], c) - [62], d) - [63]).

CV experiments have been made for the pure graphite rod used in the fabrication of electrodes and for graphite rod covered in the carbon paste used as an adhesive medium between graphite rod and active material. In addition, CV experiments with different potential window were done with a commercial EDLC capacitor, specifically a $4F$ Powerstor® HV series capacitor. The pure graphite rod exhibits extremely low capacitance but it is almost purely EDL capacitance as it can be seen in figure 4.25.

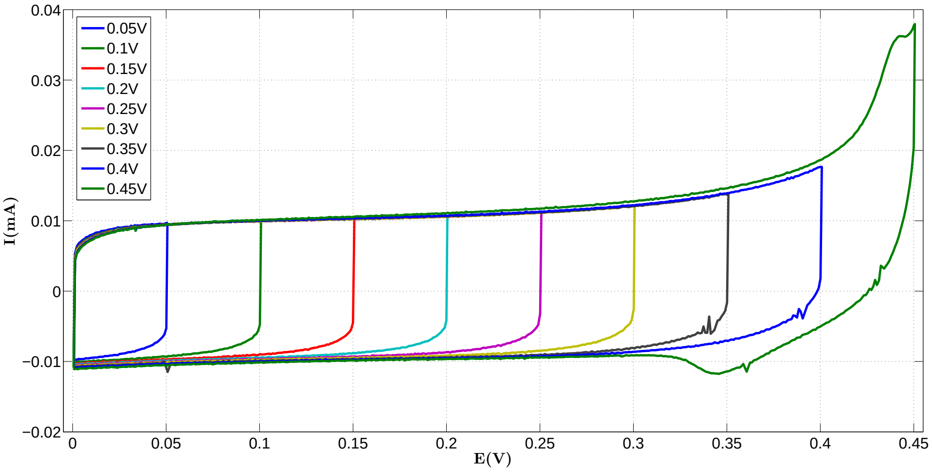

FIGURE 4.25: CV curve of graphite rod. Almost pure EDL capacitance can be seen. Scan rate - $50mV/s$. The upper potential limit is marked in the legend.

The graphite rod covered with the carbon paste exhibits higher capacitance but still much lower compared to the previously test electrodes with the active material. The capacitance was approx. $5mF$ compared to a typical value of a few hundreds of millifarads for the fabricated electrodes. The CV graphs are presented on figure 4.26 and the phenomenon of pseudocapacitance is still present. It is more likely that the pseudocapacitance is introduced **only** by the carbon paste in all the electrodes. This is still just an assumption and further experiments are needed.

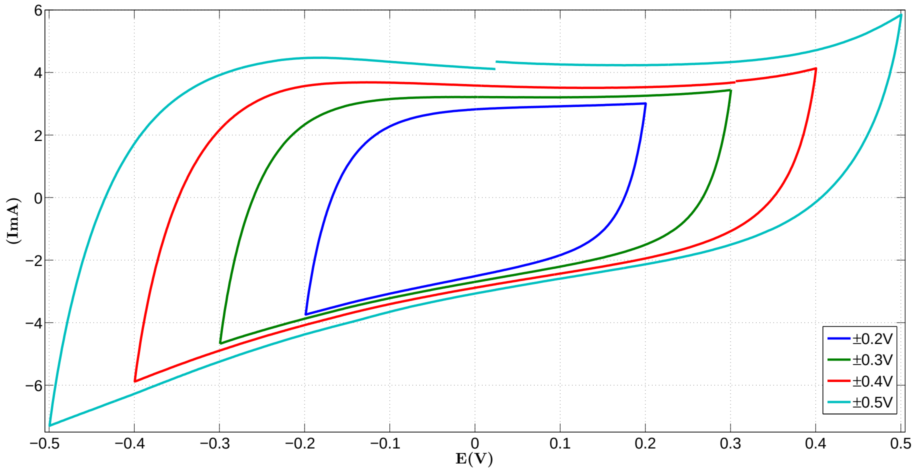

FIGURE 4.26: Pseudocapacitance behavior from the graphite rod covered with graphite paste. Potential window is marked in the legend. Scan rate - $50mV/s$

The commercial supercapacitor on first look exhibits pure EDL capacitance. But the huge capacitance of the capacitor increases the current so the use of $50mV/s$

scan rate was not possible to be used since the current was close to the limit of the potentiostat. The different scan rate makes impossible the direct comparison of the pseudocapacitance current. A zoomed image were the pseudocapacitance is expected shows a small deviation between the graphs, so some pseudocapacitance is still present but is negligible compared to the huge EDL capacitance and buried under the high current. The CV graph and the zoomed part are presented in figure 4.27.

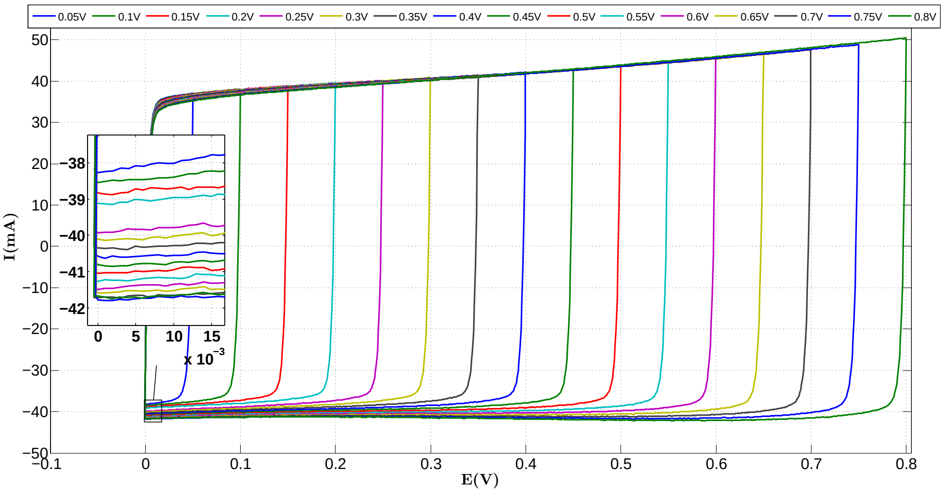

Figure 4.27: CV graph of the commercial capacitor. Some pseudocapacitance is noticed at the ZPC shown in the small window. The increasing positive current is explained by the squeezing of EDL. Upper potential limit is shown in the legend. Scan rate - $10mV/s$

Unfortunately, pseudocapacitance and EDL are not completely independent. In order to try to quantify the pure EDL capacitance for our electrodes all the CVs for all the electrodes were repeated with a potential window of $\pm 0.5V$ instead of $\pm 1V$ used previously. The results are shown in table 4.2. And similarly to figure 4.22 and 4.23 the ZPC was extrapolated to zero potential window and the pure EDL capacitance was extracted from that current. The ZPC capacitance is presented on table 4.3. This capacitance is much lower compared to the ones from potenial windows of $\pm 1V$ and $\pm 0.5V$. Nevertheless, in general the capacitance increases with decreasing scan rate and once again Type-B-4h has the highest gravimetric capacitance.

4.2.2 Electrolyte

Saturated KCl is easy to prepare and safe because of its low toxicity and low corrosiveness. This makes it ideal when testing several electrodes. Nevertheless, KCl is

	Gravimetric Capacitance						
Scan Rate	Type-A-0h	Type-B-0h	Type-B-1h	Type-B-4h	Par-0h	Par-1h	Par-4h
200 mV/s	0.97F/g	1.40F/g	2.38F/g	9.00F/g	1.51F/g	1.12F/g	1.54F/g
100 mV/s	1.32F/g	1.88F/g	3.15F/g	10.55F/g	1.90F/g	1.31F/g	1.73F/g
10 mV/s	2.45F/g	3.20F/g	5.24F/g	14.88F/g	2.65F/g	1.86F/g	4.74F/g
1 mV/s	4.74F/g	4.88F/g	8.63F/g	18.25F/g	7.59F/g	3.37F/g	4.30F/g
0.1 mV/s	17.98F/g	16.02F/g	20.83F/g	36.00F/g	72.15F/g	10.93F/g	-

Table 4.2: Gravimetric capacitance of all electrodes in saturated KCl electrolyte in potential window from $-0.5V$ to $0.5V$.

	Gravimetric Capacitance						
Scan Rate	Type-A-0h	Type-B-0h	Type-B-1h	Type-B-4h	Par-0h	Par-1h	Par-4h
200 mV/s	0.32F/g	0.42F/g	1.27F/g	7.51F/g	0.60F/g	0.60F/g	0.85F/g
100 mV/s	0.73F/g	0.86F/g	1.625F/g	9.00F/g	0.77F/g	0.79F/g	1.03F/g
10 mV/s	1.18F/g	1.24F/g	2.38F/g	11.23F/g	1.23F/g	1.03F/g	1.21F/g
1 mV/s	1.60F/g	2.36F/g	1.07F/g	12.14F/g	2.26F/g	1.88F/g	1.93F/g
0.1 mV/s	1.81F/g	5.43F/g	6.85F/g	4.75F/g	29.75F/g	-	-

Table 4.3: Gravimetric capacitance of all electrodes in saturated KCl electrolyte extracted from the ZPC for zero potential window (Pure EDL capacitance).

not an ideal EDLC electrolyte. As shown in figure 4.28 potassium chloride has the poorest performance in term of specific capacitance compared to other aqueous electrolytes [67].

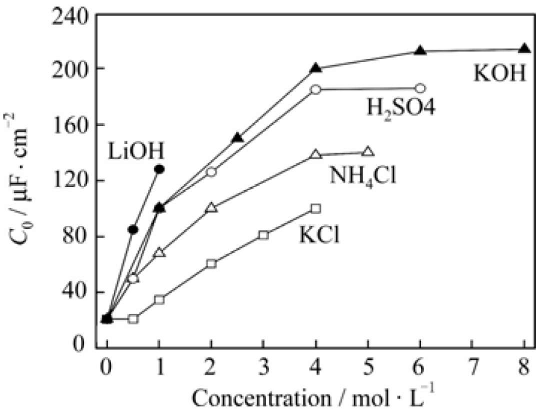

Figure 4.28: Comparison of specific capacitance of various aqueous electrolytes. KOH yields almost triple specific capacitance compared to KCl. The reported values are measured with two platinum electrode system.[67]

On the other hand KOH seems to be a better electrolyte. Two electrodes were tested with $6M\ KOH$ solution as electrolyte. Specifically, Type-B-4h and Par-4h electrodes were tested for potential window of $\pm 0.5V$ and $-1V$ to $0.7V$. At a potential of around $0.8V$ bubbles start to form around the working electrode, so the positive potential had to be limited to $0.7V$. In addition, the reference electrode was switched from a Ag/AgCl to a platinum electrode. In figures 4.29 and 4.30 a CV curve with KCl and KOH electrolytes of sample Par-4h and Type-B-4h are presented. Note that the current axis is normalized over the mass of the electrode.

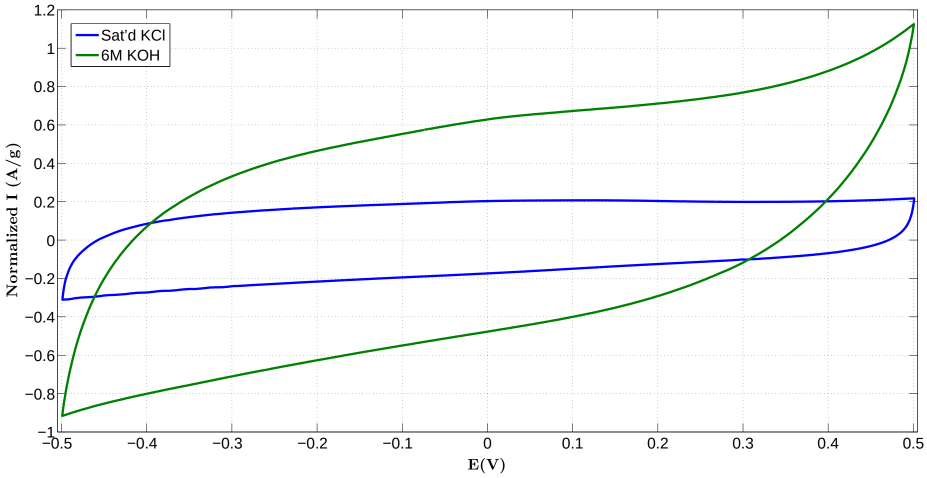

FIGURE 4.29: Comparison of CV curves of Par-4h electrode with saturated KCl and 6M KOH electrolyte. The current is normalized over the mass of working electrode. KOH yields more than double ZPC than KCl Scan rate - $100mV/s$

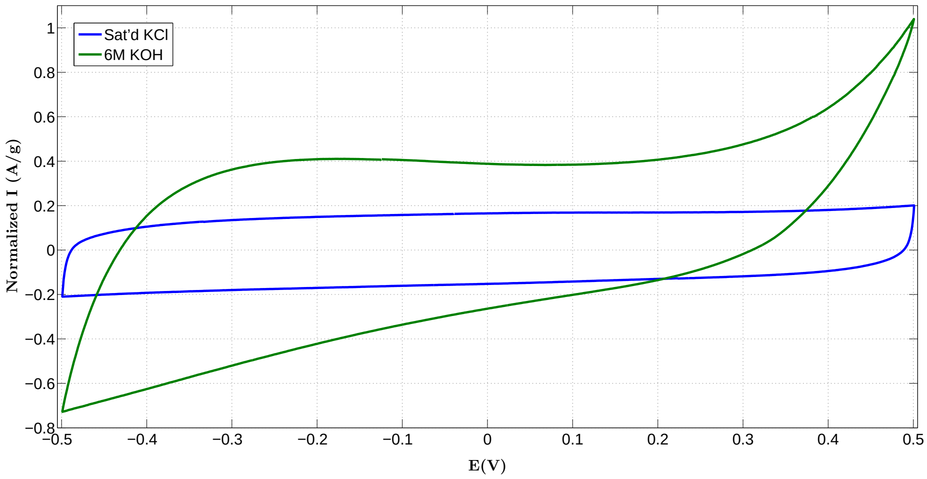

FIGURE 4.30: Comparison of CV curves of Type-B-4h electrode with saturated KCl and 6M KOH electrolyte. Similar to the Par-4h electrode KOH exhibits higher capacitance. The current is normalized over the mass of working electrode. Scan rate - $10mV/s$

Despite the different electrolyte the phenomenon of pseudocapacitance is still noticed in KOH. In figure 4.31 the Par-4h electrode were tested with different potential windows. The capacitance decreases with the decrease in the potential window.

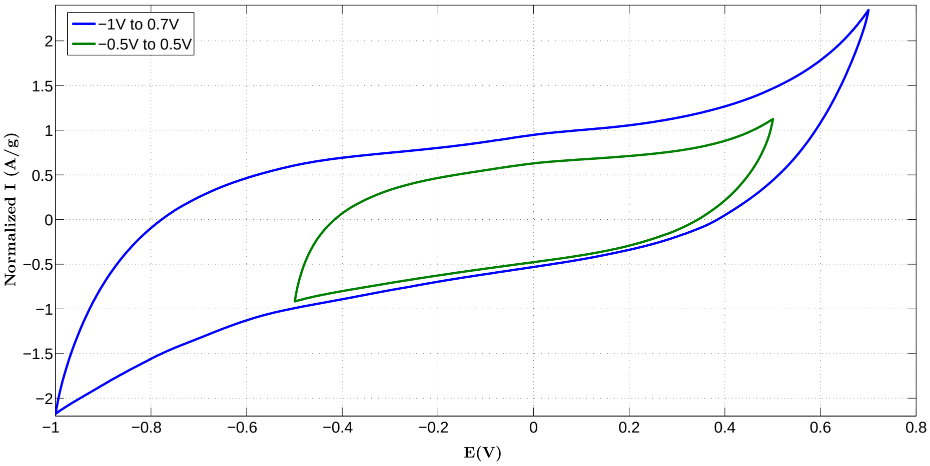

FIGURE 4.31: CV graphs with different potential windows of Par-4h electrode in 6M KOH electrolyte. Pseudocapacitance is still present in KOH electrolyte. The current is normalized over mass. Scan rate - $10mV/s$

Finally, the calculated gravimetric capacitances for both electrodes for both potential windows are presented in table 4.4. Once again Type-B-4h electrode yields the higher capacitance up to $217.63F/g$ for $1mV/s$ scan rate. This capacitance probably comes from the bottom activated current collector, which created very high surface area. In addition, in order to keep the capacitance low to avoid the contribution of the counter electrode, only but a few milligrams (approx. $6mg$) of material were used. This makes the effect of the pseudocapacitance coming from the paste an important factor, since the mass ratio between paste and active material is changed. This can also be noticed by the big difference in capacitance between wide and narrow potential window. More experiments should be done with more active material and a counter electrode with higher capacitance. Nevertheless, the highest calculated capacitance from the experiments is $\mathbf{217.63F/g}$ for the Type-B-4h electrode in $6M\ KOH$ electrolyte for a potential window of $-1V$ to $0.7V$ and a scan rate of $1mV/s$.

	Gravimetric Capacitance			
	Potential Window ($-1V$ to $0.7V$)		Potential Window ($-0.5V$ to $0.5V$)	
Scan Rate	**Type-B-4h**	**Par-4h**	**Type-B-4h**	**Par-4h**
200 mV/s	19.23 F/g	6.74 F/g	11.08 F/g	4.13 F/g
100 mV/s	28.95 F/g	9.08 F/g	17.05 F/g	5.48 F/g
10 mV/s	73.16 F/g	27.48 F/g	39.36 F/g	13.5 F/g
1 mV/s	217.63 F/g	102.22 F/g	75.18 F/g	31.35 F/g

TABLE 4.4: Gravimetric capacitance of Type-B-4h and Par-4h electrodes in $6M\ KOH$ electrolyte for different potential windows.

4.3 Electrochemical Impedance Spectroscopy (EIS)

In order to calculate the power density EIS measurements have been performed. The measurements took place in the same device as the CV experiments under the same setup. A sinus potential signal of amplitude of $1mV$ was applied from frequencies of $50mHz$ to $2MHz$. The resulting impedance is plotted in a Nyquist plot where the real part of the impedance is shown in the x-axis and the imaginary part in the y-axis. By taking the point where the curve intercepts the real axis one can find the equivalent series resistance (ESR). The ESR consists of all the electric resistances of the capacitor and it is used for the calculation of power density [68, 69, 70]. A typical Nyquist EIS plot is shown in figure 4.32 for KCl and KOH electrolyte.

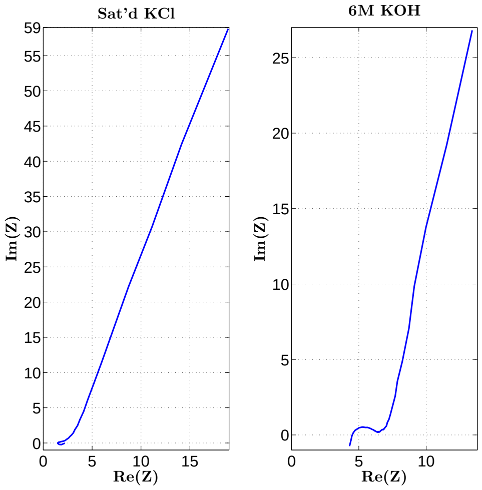

FIGURE 4.32: EIS Nyquist plot of Type-B-4h electrode in saturated KCl and 6M KOH electrolyte.

Another method to calculate the ESR is through the charge-discharge cycling technique. The capacitor is charged with a current pulse until it reaches a desired potential and then an opposite current pulse discharges the capacitor down to zero potential. At the point of current pulse edge, there is a potential Ohmic drop (iR). Dividing the iR with two times the applied pulse amplitude the ESR can be calculated [71]. An example of a charge-discharge cycling is presented on figure 4.33.

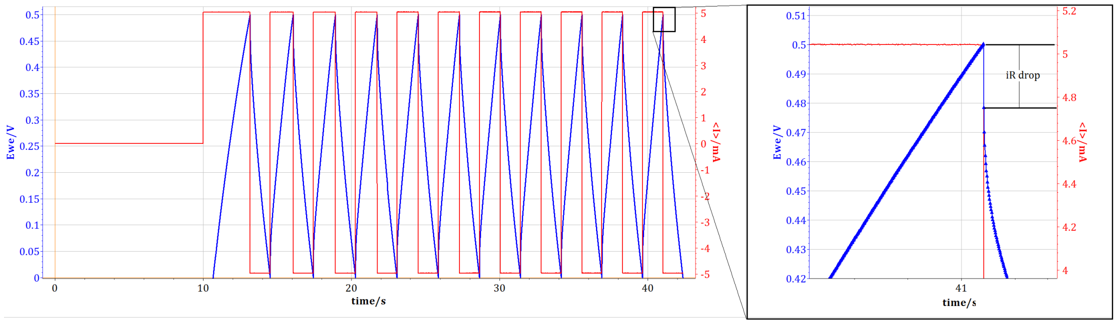

Figure 4.33: Charge discharge cycling and ohmic drop calculation.

In addition, from the EIS curve the equivalent diffusive resistance (EDR) can be calculated. EDR is calculated by the length of the Warburg region which is the 45^o slope length in the EIS Nyquist plot. An example is shown in figure 4.34. EDR shows how readily do the ions diffusive into the pores and close to surface to form the EDL.

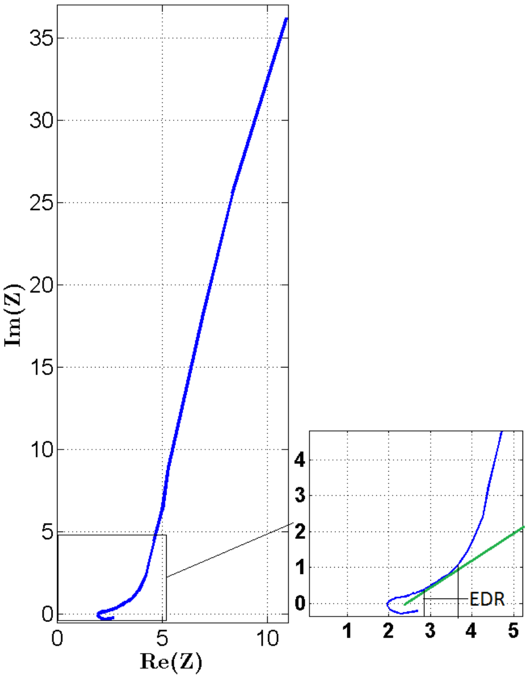

Figure 4.34: Nyquist plot of EIS and calculation of EDR through the Warburg region. (Green line with slope 45^o)

The calculated ESR from EIS and charged discharge cycling and EDR are presented in table 4.5 for KCl electrolyte and table 4.6.

The EDR is higher for Type-A sample than Type-B samples, which shows that the diffusion in the small and shallow pores of Type-B samples is easier than the slightly bigger but longer pores of sample Type-A. Between the Type-B samples, the longer the activation the higher the EDR. The activation creates extra nanopores especially

	ESR - EIS	**ESR - Dis-/charge**	**EDR**
Type-A-0h	1.337Ω	2.13Ω	1.297Ω
Type-B-0h	1.492Ω	2.00Ω	0.920Ω
Type-B-1h	1.613Ω	1.71Ω	1.020Ω
Type-B-4h	1.971Ω	2.47Ω	1.133Ω
Par-0h	1.225Ω	2.20Ω	3.203Ω
Par-1h	1.737Ω	2.53Ω	2.965Ω
Par-4h	1.334Ω	2.44Ω	3.194Ω

Table 4.5: ESR and EDR in KCl electrolyte.

	ESR - EIS	**ESR - Dis-/charge**	**EDR**
Type-B-4h	4.891Ω	6.384Ω	0.712Ω
Par-4h	6.041Ω	6.492Ω	1.240Ω

Table 4.6: ESR and EDR in KOH electrolyte.

in the current collector. The nanopores hinder the diffusion. Finally as expected the Par-0h, Par-1h and Par-4h samples have the higher diffusion resistance because of the very long pores as it can be seen on table 4.6. The Par samples have pores with width of $100nm - 200nm$ and length of $\sim 60\mu m$ (the diffusion length is $\sim 30\mu m$ since the pores are open to electrolyte from both sides). The diffusion in those pores is much harder compared to the other electrodes hence the EDR is much higher. In addition, the activation does not seem to have any effect on the diffusion and pores. Finally, for the comparison of the EDR between different electrolytes, it is obvious that the EDR is much lower in KOH than in KCl. This is expected since the mobility of the OH^- ion is much higher than the one of Cl^- ion. In addition OH^- ion is smaller (effective ionic radius $0.110nm$[72]) than Cl^- (effective ionic radius $0.181nm$[73]).

The two methods of calculating ESR give similar results. The charge/discharge method yielding slightly higher ESR. Since current collectors were not thick enough to have direct electric contact between them and the device electrodes, the performance of the current collector cannot be conclusive directly by the comparison of ESR. In addition carbon paste was used to attached the active material on a graphite rod, and the contact area between the active material and the paste were not consistent between different electrodes.

Nevertheless an attempt to analyze the resulted ESR calculated from EIS will follow. Type-A sample which the carbon paste were attached on the current collector yields lower ESR than Type-B samples that were attached on random sides since the active material pieces were quite small. Looking the measurements of Type-B samples, the ESR increases as the activation time increases. This is either caused by the change of conductivity due to activation or due to the activation/etching of the current collector. Finally the Par samples have the lower ESR of all. This either comes from the fact the different carbon precursor materials were used, which may result in higher conductivity carbon, or the fact that carbon paste filled some (thousand in numbers) pores which resulted in a higher contact area between paste and active material hence reduced electric resistance.

In KOH the ESR is significantly higher. The reason behind this, is still unknown. One would expect that KOH would yield lower ESR since its conductivity is higher than KCl. Specifically, $6M\ KOH$ has a conductance of approx. $0.55S/cm$ where saturated KCl has approx $0.36S/cm$ [74].

The maximum power (P) of each electrode and the gravimetric power (P_g) can be calculated from the following formulas [75]:

$$P = \frac{V^2}{4 * ESR}$$

$$P_g = \frac{P}{m},$$

where V is the maximum applied potential and m is the mass of the electrode. The calculated gravimetric capacitance for all electrodes is presented on table 4.7. As it can be seen the KOH yields lower power than KCl because of the higher ESR but also because the narrower potential window. The best performance in terms of power density comes from the Par-0h which also has the lower ESR compared to all other electrodes.

4.4 Discussion

BET measurement have been done only for Type-B-0h, Type-B-1h and Type-B-4h samples and revealed a SSA of $105.58m^2/g$, $161,18m^2/g$ and $275.70m^2/g$, respectively. The BET measurement was done in Micrometrics® Gemini VII device but validation errors are showing up in the reports because of the low amount of mass used

	Saturated KCl	
	Gravimetric Power EIS	**Gravimetric Power Dis-/Charge**
Type-A-0h	$5.649kW/kg$	$3.561kW/kg$
Type-B-0h	$6.547kW/kg$	$4.88kW/kg$
Type-B-1h	$9.225kW/kg$	$8.753kW/kg$
Type-B-4h	$15.855kW/kg$	$12.652kW/kg$
Par-0h	$25.83kW/kg$	$14.836kW/kg$
Par-1h	$6.44kW/kg$	$4.464kW/kg$
Par-4h	$18.55kW/kg$	$10.313kW/kg$
	6M KOH	
	Gravimetric Power EIS	**Gravimetric Power Dis-/Charge**
Type-B-4h	$9.718kW/kg$	$4.746kW/kg$
Par-4h	$7.445kW/kg$	$4.416kW/kg$

Table 4.7: Gravimetric power calculated from EIS and charge discharge cycling in KCl electrolyte

for the measurements. New electrodes must be fabricated and the measurements should be repeated. Nevertheless, an attempt for an approximation of the specific surface capacitance will be made. For the Type-B-0h electrode the SSA corresponds to specific capacitance from $2.51\mu F/cm^2$ to $11.47\mu F/cm^2$. For sample Type-B-1h corresponds to a specific capacitance from $2.55\mu F/cm^2$ to $12.92\mu F/cm^2$. And for sample Type-B-4h from $3.89\mu F/cm^2$ to $13.91\mu F/cm^2$ in KCl and from $6.97\mu F/cm^2$ to $78.93\mu F/cm^2$ in KOH.

If the results of the BET measurements are correct there is another proof that the activation process did not work as it was intended to. In literature one hour CO_2 activation results in carbons with SSA of approx. $700m^2/g$ and four hours activation in samples with SSA of approx. $2000m^2/g$ [46]. Nevertheless the relatively small increase of surface area caused an increase in gravimetric capacitance summarized in table 4.8.

	Gravimteric Capacitance					
Scan Rate	**Type-B-0h**	**Type-B-1h**	**Type-B-4h**	**Par-0h**	**Par-1h**	**Par-4h**
$200mV/s$	-	+55.0%	+305.66%	-	−33.93%	−7.58%
$100mV/s$	-	+30.48%	+256.82%	-	−33.84%	−11.58%
$10mV/s$	-	+59.69%	+254.24%	-	−38.80%	−12.45%
$1mV/s$	-	+68.29%	+216.84%	-	−52.91%	−19.93%

Table 4.8: Effect of activation on gravimetric capacitance. The numbers indicate the difference from the non-activated samples. (Electrolyte - saturated KCl, potential window $\pm 1V$).

As we can see for the Type-B samples the longer the activation the higher the capacitance. This is because of the addition of the extra surface area that mainly came from the activation of the bottom layer that was planed to be used as current collector.

In contrast, for the Par electrodes the activation reduce their gravimetric capacitance. This again comes from the reduction of SSA. One can see the difference between Par-0h and Par-4h samples in their SEM images (figure 4.13 and 4.16).

	Gravimetric Capacitance			
	Type-B-4h		**Par-4h**	
Scan Rate	**KCl**	**KOH**	**KCl**	**KOH**
$200mV/s$	-	+23.11%	-	+168.18%
$100mV/s$	-	+61.61%	-	+216.67%
$10mV/s$	-	+164.55%	-	+184.81%
$1mV/s$	-	+311.94%	-	+633.72%

Table 4.9: Comparison of electrolytes in terms of gravimetric capacitance. The numbers indicate the difference from KCl electrolyte. (For potential window $\pm0.5V$)

In table 4.9 the effect of electrolyte on gravimetric capacitance is presented. It is obvious that KOH gives a huge boost in capacitance especially in lower scan rates. This is expected as shown before in figure 4.28 where KOH has almost triple specific capacitance on platinum electrode. The effect on the scan rate maybe it has to do with the difference in mobilities of Cl^- and OH^-.

The change of capacitance (i.e pseudocapacitance) dependency on the potential window is presented on table 4.10 for KCl and KOH electrolytes.

	Gravimetric Capacitance				
	Saturated KCl				
	Scan Rate	$200mV/s$	$100mV/s$	$10mV/s$	$1mV/s$
Electrode Name	**Potential window ($-0.5V$ to $0.5V$)**	**Potential window ($-1V$ to $1V$)**			
Type-A-0h	-	+86.60%	+71.97%	+95.91%	+97.05%
Type-B-0h	-	+89.28%	+118.09%	+106.25%	+148.16%
Type-B-1h	-	+72.69%	+69.84%	+101.15%	+141.37%
Type-B-4h	-	+20.44%	+38.67%	+57.12%	+110.24%
Par-0h	-	+83.44%	+72.63%	+109.06%	+110.14%
Par-1h	-	+63.39%	+65.65%	+82.26%	+131.75%
Par-4h	-	+66.23%	+67.63%	+23.20%	+196.98%
	6M KOH				
Electrode Name	**Potential window ($-0.5V$ to $0.5V$)**	**Potential window ($-1V$ to $0.7V$)**			
Type-B-4h	-	+73.56%	+69.79%	+85.87%	+189.94%
Par-4h	-	+63.19%	+65.69%	+103.56%	+226.06%

Table 4.10: Dependency of gravimetric capacitance on potential window for KCl and KOH electrolyte. The numbers indicate the difference from $\pm0.5V$ potential window.

The results almost in all the cases are consistent. The pseudocapacitance effect increases with the scan rate. The fact that all the samples have similar percentages may indicate that indeed the carbon paste causes the pseudocapacitance. Since Type-A and

Type-B samples use different precursor material (i.e. Su-8) compared to Par samples (i.e. Parylene-C) and yet they exhibit the same pseudocapacitance.

Par-4h sample has a constant (percentage) psedocapacitance in KCl and KOH electrolyte. In contrast, Type-B-4h sample has lower psedocapacitance effect in KCl than in KOH. This maybe an effect of different pH of the electrolytes. The high pH of KOH may promote the disassociation of functional groups from the surface of Type-B-4h electrode which maybe not present in the Par-4h electrode.

Finally, in order to investigate the stability and the ageing of the electodes long charge/discharge cycling were taken for the Par-4h electrode in KOH electrolyte. In figure 4.35 gravimetric capacitance vs the cycle number is presented. The electrode exhibits excellent stability, since it experiences a drop in capacitance of only $\sim 5\%$ over 11000 cycles.

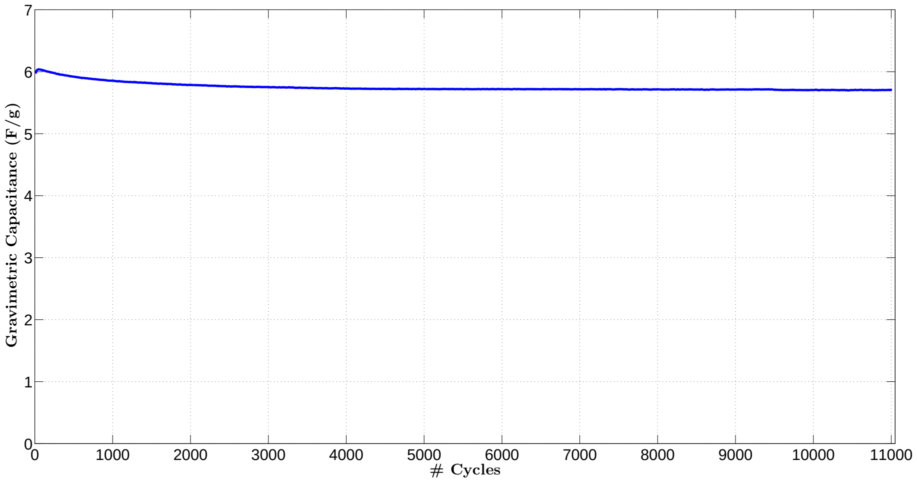

Figure 4.35: Long charge/discharge cycling for stability and ageing investigation. Only a drop of $\sim 5\%$ is noticed over 11000 cycles. (Applied current pulses of $\pm 5mA$ and max charge potential of $0.5V$)

Chapter 5

Conclusion

5.1 Summary

In this thesis the subject of electric double layer capacitor electrode has been investigated. First, in order to answer our first research question, through literature study the ideal properties of EDLC solid electrode have been found in terms of energy (charge storage) and power density. The literature study revealed that both micropores and meso-, macropores are needed. Micropores serve for the desolvation of electrolyte ions and achieving the superionic state. Wider pores work as electrolyte buffer reservoir and ion highways.

According to these properties several electrodes proposed and fabricated with two novelties. First, the use of current collector made out of the same material as the electrode itself, and incorporate it in the fabrication of the electrode. This way unwanted interface phenomena(electric resistance/capacitance) are theoretically eliminated. Second, the proposed electrode combines two fabrication methods, i.e. templating method and carbon activation. Through the templating method highly order macropores are are created, and through activation nanopores are created on the walls of the macropores. Aluminum oxide membrane was used as a template and the samples were activated through physical activation in CO_2 atmosphere. The activation did not had the expected results on the electrodes. This is our attempt to answer the second scientific question in respect with the findings of the first question.

The electrodes have been physically and electrochemically characterized and exhibit high capacitance (up to 217.63 F/g) and power up to 25.83 kW/kg. The value for the capacitance is not extremely high and capacitances up to $370F/g$ have previously reported for aqueous electrolytes and AC electrodes [76]. The power density is a quite high value but once again commercial electrodes are available with power densities up to $37.12kW/kg$ [77]. Despite the fact the values are average there is a plenty room for improvement.

5.2 Future work

Nevertheless, this is only but a first step for the creation of an ideal electrode. Some proposals for future work and improvement of our electrode concept follows.

Current Collector and fabrication process - Since our electrodes greatly deform and even crack during pyrolysis, thick carbon current collectors were impossible to be used. Since the back layer was still too thin and too fragile to make direct contact for the measurements, the fabricated electrodes were attached with carbon paste on a graphite rod. Despite the fact that all three (carbon electrode, carbon paste and graphite rod) are made out of carbon, interface phenomena are still present. New fabrication ways must be investigated that will enable the fabrication of flat and less deformed electrodes. When this is achieved the concept of merged electrode and current collector can be in detail investigated. A first step towards the improvement of the fabrication process, is the removal of the dicing foil from the process. Dicing foil is convenient for detaching the Su-8 layer from the substrate but only for thin layer which are flexible. With the increased thickness of Su-8 the process of removing the foil is much harder and the samples tend to crack. An easy substitute can be a sacrificial layer of polystyrene instead of dicing foil. Polystyrene can be dissolved in toluene which leaves Su-8 and aluminum oxide intact. The process has been used before and is described in detail in [78]. Finally, the etching of the template were not possible in Type-B samples, since a carbon layer was protecting it. A future fabrication process should also tackle this problem since there was a significant amount of surface area and pores which was not accessible to the electrolyte.

Activation - As it is described the activation was not successful, meaning that the results were not the ones that were expected. The activation process should be tuned for our electrodes. Finding the right parameters for the activation is expected to improve the results by a significant factor.

Template - An easy next step experiment is to use an aluminum oxide membrane with smaller pores. Specifically membranes with pores down to $20nm$ are commercially available. Reducing the size of the pore will significantly improve the specific surface area and hence the capacitance. Finally, instead of aluminum oxide membrane, different templates with highly order pores can be used, such as a nanofabricated membrane.

Precursor Material and Electrolyte - During the thesis several times the significant of the electrolyte has been noted. Specifically, the size of electrolyte ions compared to the nanopores of the electrode. Despite the fact that physical activation of carbon is a tunable process, it always yields electrodes with relatively wide pore size distribution. As described in Chapter 2.3 carbide derived carbons offer very narrow pore size distribution. Instead of Su-8 as precursor and carbon activation, a carbide and chlorine treatment can be used. Note that the carbide should be chosen along with the electrolyte. Different carbides yield different pore sizes. Someone can investigate which electrolyte yield the best results for a specific carbide and virsa versa. In addition different electrolytes can be tested with the current design, including aqueous, organic and IL electrolytes.

Result validation - The **most** important second step is the validation of the results. Over the whole thesis there are several instances were the reliability of the results is questioned. So the repeat of the same fabrication and same experimentation is mandatory. Some further experiments that will help in the understanding of some phenomena are listed bellow.

- **Current collector:** Electrodes of Type-A could be fabricated with different thickness of current collector and the ESR can be quantified and its dependency to the current collector thickness can be found.
- **Pseudocapacitance:** An important finding was the pseudocapacitance of the electrodes. First, the source of the pseudocapacitance must be found. If thick

current collectors are fabricated the use of carbon paste will be avoided. Testing of such electrodes without paste can reveal if the pseudocapacitance comes from the paste or the active material. If the pseudocapacitance comes from the electrode CV measurements with different pH in the same electrolyte can show if the pseudocapacitance comes from the functional groups on the surface of the electrode.

- **Capacitance:** In order to verify the capacitance results, electrodes with more mass and hence more capacity must be tested. This will allow the use of lower scan rates since the current will be higher and noise will not affect the measurement. In addition higher mass of active material will also give information on the pseudocapacitance since the ratio between mass of paste and mass of active material will be different.
- **BET measurements:** In order to validate the results of the BET measurements, the measurements should be repeated with higher amount of each sample.

There are several other improvements that one can propose and the race for pushing the boundaries of energy and power density in EDLC is still on.

Appendices

Appendix A

Fabrication Remarks

During fabrication some unexpected results came to the surface irrelevant to the EDLC applications. Specifically I would like to describe three phenomena.

A.1 Crystalline Pyrolytic Carbon

During the first experiments of pyrolysis where we had Su-8 directly coated on silicon wafer, because of the high adhesion the carbon used to crack under the stress due to shrinking. After SEM imaging, small carbon crystals could be noticed. Such crystals are presented in figure A.1.The crystals are in the sub-micrometer scale.

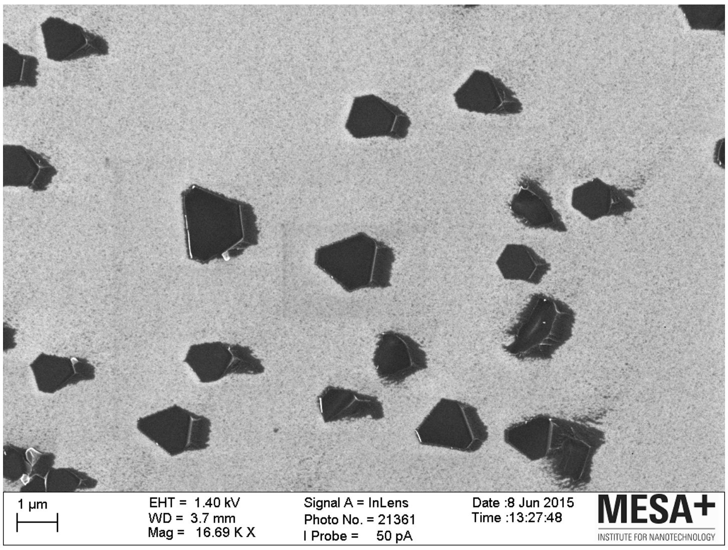

Figure A.1: SEM image of small carbon crystals

In addition in cases where the samples cracked under the stress of pyrolysis carbon crystalic structures grew out of the side pores of the membrane. An example is shown on figure A.2.

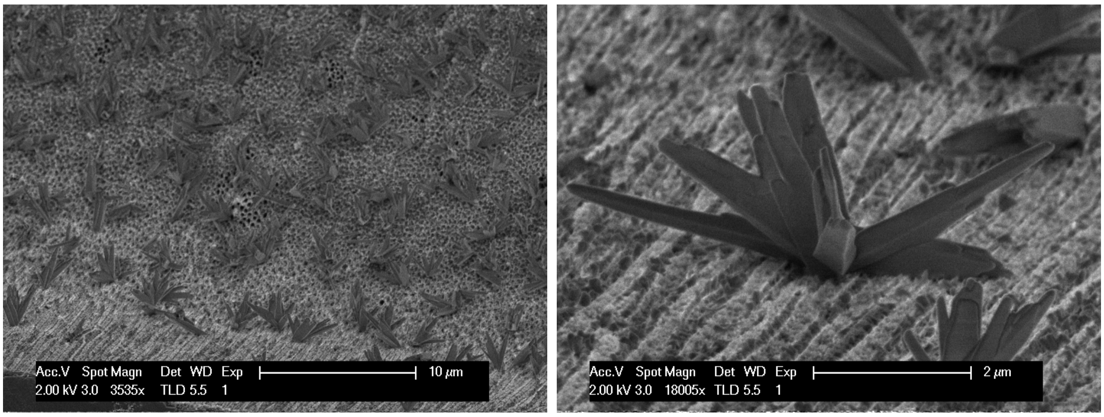

FIGURE A.2: SEM image of small carbon crystalic structures grow on the side of the membrane.

The crystals are made out of a material named crystalline pyrolytic carbon. And they consist of graphene sheets with covalent bonds between them[79]. There are several unique properties of crystalline pyrolytic carbon that make it appealing.E.g. crystalline pyrolytic carbon exhibits several anisotropic properties (e.g. thermal conductivity) depending on the crystal orientation and exhibits the highest diamagnetism of all diamagnets in room temperature along the cleavage of the crystal. Pyrolysis of Su-8 at 950^oC is not expected to create crystalline carbon. In order to create such carbon, pyrolysis at extremely high temperatures (2700^oC)[55].

Two remarks must be made. First, temperature of 950^oC to cause the formation of small carbon crystals. Second, crystalline pyrolytic carbon can be created via high temperature pyrolysis.

A.2 Calcium Carbonate Activation

Once again, during pyrolysis trials some of our samples were contaminated by Calcium Carbonate($CaCO_3$) particles. Calcium carbonate is a typical contamination substance and it can come from paper(non cleanroom tissues) or from powder inside the latex or nitrile gloves. The surprising result was that carbon was activated around the area of such particles. Examples of such activation are presented in figure A.3. As shown in the picture, severe activation took place around the particles. The closest to the particle the higher the activation. The pores are in the nanometer scale.

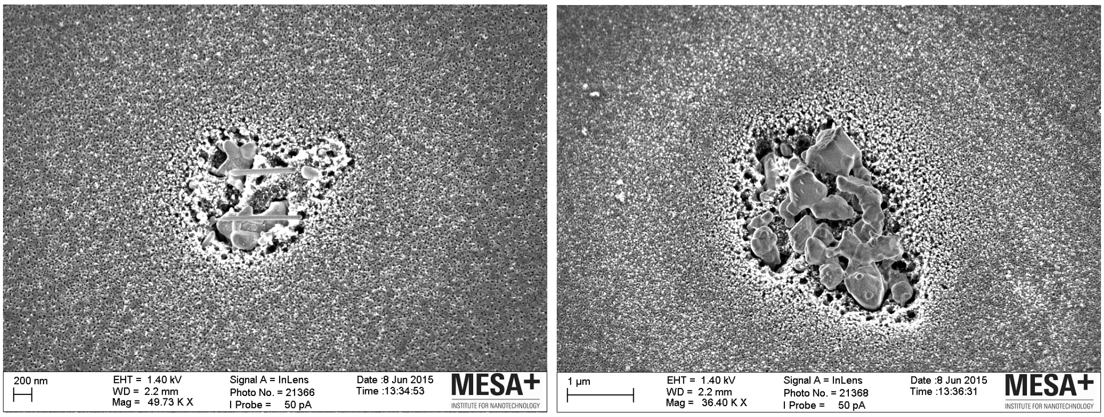

Figure A.3: SEM image of calcium carbonate activation.

EDX during SEM confirmed that the particles were indeed Calcium Carbonate. Up to my current knowledge calcium carbonate has not been used for the activation of carbon. The results is unknown if they are reproducible, controllable, or tunable.

A.3 Carbon Nanofibers

During the fabrication of Type A electrodes, SEM images directly after pyrolysis, reveal another unexpected result. Carbon nanofibers seem to have grown out of the surface of the electrode. Such an example is presented on figure A.4.

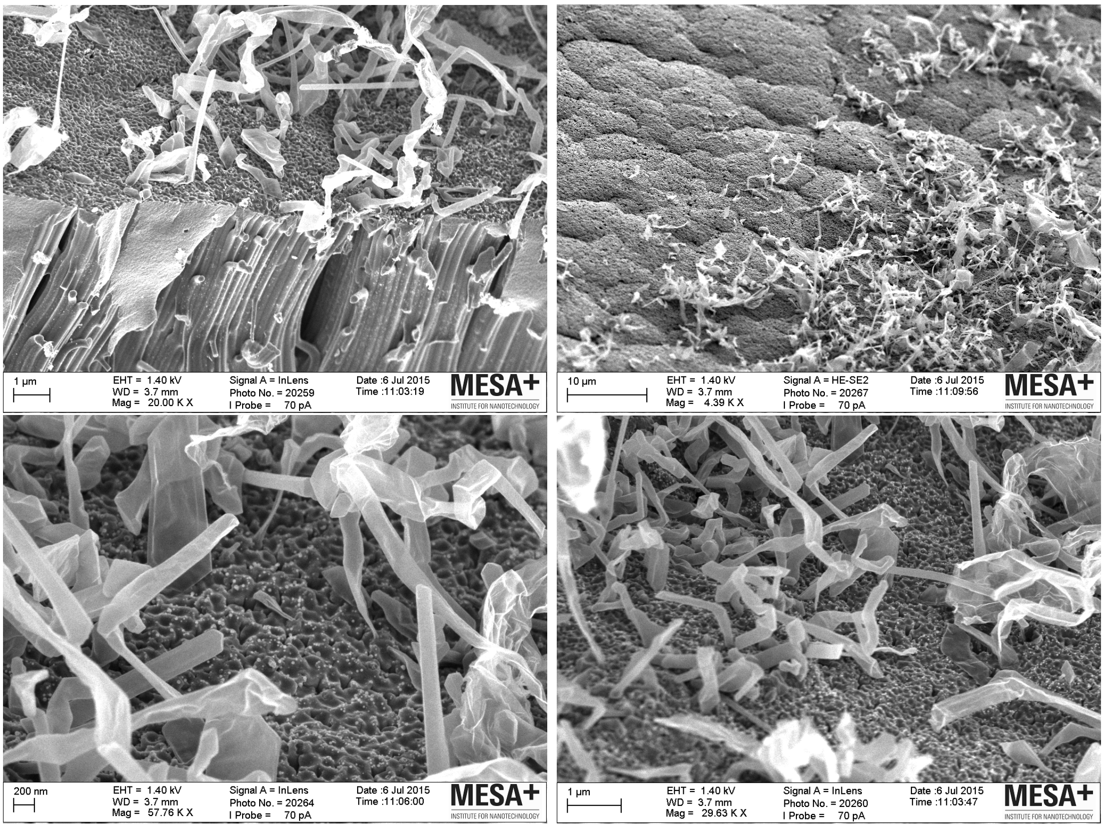

FIGURE A.4: Carbon nanofibers grown on the surface of the electrode

The carbon nanofibers can be seen with white color. There are areas where more fibers are present and areas with no fibers(Figure A.4-top right). EDX analysis showed that the fibers are indeed made out of carbon. Their thickness ranges between 100nm and 200nm. The reason and the mechanism of growth is still unknown.

Bibliography

[1] J. R. Miller and P. Simon, "Materials science. Electrochemical capacitors for energy management.," *Science (New York, N.Y.)*, vol. 321, no. 5889, pp. 651–652, 2008.

[2] R. Kötz, R. Kötz, M. Carlen, and M. Carlen, "Principles and applications of electrochemical capacitors," *Electrochim. Acta*, vol. 45, pp. 2483–2498, 2000.

[3] C. Vix-Guterl, E. Frackowiak, K. Jurewicz, M. Friebe, J. Parmentier, and F. Beguin, "Electrochemical energy storage in ordered porous carbon materials," *Carbon*, vol. 43, no. 6, pp. 1293–1302, 2005.

[4] E. Frackowiak and F. Béguin, "Carbon materials for the electrochemical storage of energy in capacitors," *Carbon*, vol. 39, no. 6, pp. 937–950, 2001.

[5] "Basic research needs for electrical energy storage," tech. rep., US Department of Energy, 2007.

[6] J. M. Tarascon and M. Armand, "Issues and challenges facing rechargeable lithium batteries.," *Nature*, vol. 414, no. 6861, pp. 359–367, 2001.

[7] R. J. Brodd, K. R. Bullock, R. A. Leising, R. L. Middaugh, J. R. Miller, and E. Takeuchi, "Batteries, 1977 to 2002," 2004.

[8] M. Armand and J.-M. Tarascon, "Building better batteries.," *Nature*, vol. 451, no. 7179, pp. 652–657, 2008.

[9] R. F. Service, "New 'supercapacitor' promises to pack more electrical punch," *Science*, vol. 313, no. 5789, p. 902, 2006.

[10] FIA, "F1 regulations 2014." `http://www.fia.com/sites/default/files/publication/file/FIA%20F1%20Power%20Unit%20leaflet.pdf`, 2015. url date: 2015-09-24.

[11] *Electrochemical Supercapacitors: Scientific Fundamentals and Technological Applications.* Kluwer, 1999.

[12] R. Kötz and M. Carlen, “Principles and applications of electrochemical capacitors,” *Electrochimica Acta*, vol. 45, pp. 2483–2498, May 2000.

[13] Y. Zhang, H. Feng, X. Wu, L. Wang, A. Zhang, T. Xia, H. Dong, X. Li, and L. Zhang, “Progress of electrochemical capacitor electrode materials: A review,” *International Journal of Hydrogen Energy*, vol. 34, pp. 4889–4899, June 2009.

[14] E. Frackowiak, “Carbon materials for supercapacitor application,” *Phys. Chem. Chem. Phys.*, vol. 9, pp. 1774–1785, 2007.

[15] H. Li, M. Yu, F. Wang, P. Liu, Y. Liang, J. Xiao, C. Wang, Y. Tong, and G. Yang, “Amorphous nickel hydroxide nanospheres with ultrahigh capacitance and energy density as electrochemical pseudocapacitor materials,” *Nature Communications*, vol. 4, no. 1894, 2013.

[16] R. J. Hunter, *Foundations of Colloid Science.* Oxford: Clarendon Press, 2nd ed., 2001.

[17] M. Gouy, “Sur la constitution de la charge électrique à la surface d’un électrolyte,” *Journal de Physique Théorique et Appliquée*, vol. 9, no. 1, pp. 457–468, 1910.

[18] D. L. Chapman, “Li. a contribution to the theory of electrocapillarity,” *Philosophical Magazine Series 6*, vol. 25, no. 148, pp. 475–481, 1913.

[19] W. B. Russel, D. A. Saville, and W. R. Schowalter, *Colloidal Dispersions.* 1989.

[20] J. H. Masliyah and S. Bhattacharjee, *Electrokinetic and Colloid Transport Phenomena.* 2005.

[21] O. Stern *Z. Elektrochem. Angew. Phys. Chem.*, vol. 30, no. 508, 1924.

[22] D. C. Grahame, “The electrical double layer and the theory of electrocapillarity.,” *Chemical Reviews*, vol. 41, no. 3, pp. 441–501, 1947. PMID: 18895519.

[23] H. Wang and L. Pilon, “Accurate simulations of electric double layer capacitance of ultramicroelectrodes,” *Journal of Physical Chemistry C*, vol. 115, no. 33, pp. 16711–16719, 2011.

[24] L. Blum, *Structure of the Electric Double Layer*, pp. 171–222. John Wiley & Sons, Inc., 2007.

[25] M. S. Kilic, M. Z. Bazant, and A. Ajdari, "Steric effects in the dynamics of electrolytes at large applied voltages. II. Modified Poisson-Nernst-Planck equations," *Physical Review E - Statistical, Nonlinear, and Soft Matter Physics*, vol. 75, no. 2, 2007.

[26] H.-J. Butt, K. Graf, and M. Kappl, *Physics and Chemistry of Interfaces.* 2003.

[27] A. J. Bard and L. R. Faulkner, *Electrochemical methods : fundamentals and applications.* 2001.

[28] J. Varghese, H. Wang, and L. Pilon, "Simulating Electric Double Layer Capacitance of Mesoporous Electrodes with Cylindrical Pores," *Journal of The Electrochemical Society*, vol. 158, no. 10, p. A1106, 2011.

[29] B. J. Kirby, "Micro- and Nanoscale Fluid Mechanics: Transport in Microfluidic Devices," *Brian*, p. 512, 2010.

[30] W. M. Deen, "Hindered transport of large molecules in liquid-filled pores," *AIChE Journal*, vol. 33, no. 9, pp. 1409–1425, 1987.

[31] V. Jenel, Z. Hu, and D. Bedrov, "Increasing energy storage in electrochemical capacitors with ionic liquid electrolytes and nanostructured carbon electrodes," *Journal of physical chemistry letters*, vol. 4, no. 1, pp. 2829–2837, 2013.

[32] P. Simon and Y. Gogots, "Capacitive energy storage in nanostructured carbon electrolyte systems," *Accounts of chemical research*, vol. 46, no. 5, pp. 1094–1103, 2013.

[33] P. Simon and Y. Gogotsi, "Materials for electrochemical capacitors.," *Nature materials*, vol. 7, no. 11, pp. 845–854, 2008.

[34] D. Aurbach, M. D. Levi, G. Salitra, N. Levy, E. Pollak, and J. Muthu, "Cation trapping in highly porous carbon electrodes for edlc cells," *Journal of electrochemical society*, vol. 155, no. 10, pp. A745–A753, 2008.

[35] A. Janes, T. Thomberg, H. Kurig, and E. Lust, "Nanoscale fine-tuning of porosity of carbide-derived carbon prepared from molybdenum carbide," *Carbon*, vol. 47, no. 1, pp. 23–29, 2009.

[36] R. Mysyk, E. Raymundo-Pinero, J. Pernak, and F. Beguin, "Confinement of symmetric tetraalkylammonium ions in nanoporous carbon electrodes of electric double-layer capacitors," *Journal of physical chemistry*, vol. 113, no. 30, pp. 13443–13449, 2009.

[37] H. Shi, "Activated carbons and double layer capacitance," *Electrochemical Acta*, vol. 41, no. 1, pp. 1633–1639, 1995.

[38] C. Largeot, C. Portet, J. Chmiola, P. L. Taberna, Y. Gogotsi, and P. Simon, "Relation between the ion size and pore size for an electric double-layer capacitor," *Journal of the American Chemical Society*, vol. 130, no. 9, pp. 2730–2731, 2008.

[39] R. Lin, P. L. Taberna, J. Chmiola, D. Guay, Y. Gogotsi, and P. Simon, "Microelectrode Study of Pore Size, Ion Size, and Solvent Effects on the Charge/Discharge Behavior of Microporous Carbons for Electrical Double-Layer Capacitors," *Journal of The Electrochemical Society*, vol. 156, no. 1, p. A7, 2009.

[40] J. Huang, B. G. Sumpter, and V. Meunier, "A universal model for nanoporous carbon supercapacitors applicable to diverse pore regimes, carbon materials, and electrolytes," *Chemistry - A European Journal*, vol. 14, no. 22, pp. 6614–6626, 2008.

[41] Y. Yamada, T. Sasaki, N. Tatsuda, D. Weingarth, K. Yano, and R. Kötz, "A novel model electrode for investigating ion transport inside pores in an electrical double-layer capacitor: Monodispered microporous starburst carbon spheres," *Electrochimica Acta*, vol. 81, pp. 138–148, 2012.

[42] a. Celzard, F. Collas, J. F. Marêché, G. Furdin, and I. Rey, "Porous electrodes-based double-layer supercapacitors: Pore structure versus series resistance," *Journal of Power Sources*, vol. 108, no. 1-2, pp. 153–162, 2002.

[43] V. Lorrmann, G. Reichenauer, C. Weber, and J. Pflaum, "Electrochemical double-layer charging of ultramicroporous synthetic carbons in aqueous electrolytes," *Electrochimica Acta*, vol. 86, pp. 232–240, 2012.

[44] L. L. Zhang and X. S. Zhao, "Carbon-based materials as supercapacitor electrodes.," *Chemical Society reviews*, vol. 38, no. 9, pp. 2520–2531, 2009.

[45] F. Endres, D. MacFarlane, and A. Abbott, *Electrodeposition from Ionic Liquids*. 2008.

[46] L. Wei and G. Yushin, “Electrical double layer capacitors with activated sucrose-derived carbon electrodes,” *Carbon*, vol. 49, no. 14, pp. 4830–4838, 2011.

[47] J. Wang and S. Kaskel, “KOH activation of carbon-based materials for energy storage,” 2012.

[48] Y. Gogotsi, A. Nikitin, H. Ye, W. Zhou, J. E. Fischer, B. Yi, H. C. Foley, and M. W. Barsoum, “Nanoporous carbide-derived carbon with tunable pore size.,” *Nature materials*, vol. 2, no. 9, pp. 591–594, 2003.

[49] a. M. Bittner, M. Zhu, Y. Yang, H. F. Waibel, M. Konuma, U. Starke, and C. J. Weber, “Ageing of electrochemical double layer capacitors,” *Journal of Power Sources*, vol. 203, pp. 262–273, 2012.

[50] L. S. Smith, “Impedance spectroscopy theory, experiment, and applications,” *Choice: Current Reviews for Academic Libraries*, vol. 43, no. 1, p. 130, 2005.

[51] A. Lewandowski, A. Olejniczak, M. Galinski, and I. Stepniak, “Performance of carbon-carbon supercapacitors based on organic, aqueous and ionic liquid electrolytes,” *Journal of Power Sources*, vol. 195, no. 17, pp. 5814–5819, 2010.

[52] S. Brunauer, P. H. Emmett, and E. Teller, “Adsorption of Gases in Multimolecular Layers,” *Journal of the American Chemical Society*, vol. 60, no. 1, pp. 309–319, 1938.

[53] R. Mysyk, E. Raymundo-Piñero, and F. Béguin, “Saturation of subnanometer pores in an electric double-layer capacitor,” *Electrochemistry Communications*, vol. 11, no. 3, pp. 554–556, 2009.

[54] H. Wang and L. Pilon, “Mesoscale modeling of electric double layer capacitors with three-dimensional ordered structures,” *Journal of Power Sources*, vol. 221, pp. 252–260, 2013.

[55] A. Singh, J. Jayaram, M. Madou, and S. Akbar, “Pyrolysis of Negative Photoresists to Fabricate Carbon Structures for Microelectromechanical Systems and Electrochemical Applications,” 2002.

[56] R. Martinez-Duarte, P. Renaud, and M. J. Madou, “A novel approach to dielectrophoresis using carbon electrodes,” *Electrophoresis*, vol. 32, no. 17, pp. 2385–2392, 2011.

[57] C. Wang, G. Jia, L. H. Taherabadi, and M. J. Madou, “A novel method for the fabrication of high-aspect ratio C-MEMS structures,” *Journal of Microelectromechanical Systems*, vol. 14, no. 2, pp. 348–358, 2005.

[58] R. Martinez-duarte, “SU-8 Photolithography as a Toolbox for Carbon MEMS,” pp. 766–782, 2014.

[59] K. C. Morton, C. A. Morris, M. A. Derylo, R. Thakar, and L. A. Baker, “Carbon electrode fabrication from pyrolyzed parylene C,” *Analytical Chemistry*, vol. 83, no. 13, pp. 5447–5452, 2011.

[60] W. Liu, N. Liu, Y. Shi, Y. Chen, C. Yang, J. Tao, S. Wang, Y. Wang, J. Su, L. Li, and Y. Gao, “A wire-shaped flexible asymmetric supercapacitor based on carbon fiber coated with a metal oxide and a polymer,” *J. Mater. Chem. A*, vol. 3, pp. 13461–13467, 2015.

[61] M. Huang, Y. Zhang, F. Li, Z. Wang, Alamusi, N. Hu, Z. Wen, and Q. Liu, “Merging of Kirkendall growth and Ostwald ripening: CuO@MnO2 core-shell architectures for asymmetric supercapacitors.,” *Scientific reports*, vol. 4, p. 4518, 2014.

[62] C. Wang, Y. Zhan, L. Wu, Y. Li, and J. Liu, “High-voltage and high-rate symmetric supercapacitor based on mno 2 -polypyrrole hybrid nanofilm,” *Nanotechnology*, vol. 25, no. 30, p. 305401, 2014.

[63] D. H. Nagaraju, Q. Wang, P. Beaujuge, and H. N. Alshareef, “Two-dimensional heterostructures of v2o5 and reduced graphene oxide as electrodes for high energy density asymmetric supercapacitors,” *J. Mater. Chem. A*, vol. 2, pp. 17146–17152, 2014.

[64] T. Tran, D. Lenz, K. Kinoshita, and M. Droege, “Electrochemical properties of carbon aerogel composites,” *Materials for Electrochemical Energy Storage and Conversion Ii-Batteries, Capacitors and Fuel Cells*, vol. 496, pp. 607–611, 1998.

[65] V. Ruiz, C. Blanco, E. Raymundo-Pinero, V. Khomenko, F. Beguin, and R. Santamaria, “Effects of thermal treatment of activated carbon on the electrochemical behaviour in supercapacitors,” *Electrochimica Acta*, vol. 52, no. 15, pp. 4969–4973, 2007.

[66] H. A. Andreas and B. E. Conway, “Examination of the double-layer capacitance of an high specific-area c-cloth electrode as titrated from acidic to alkaline phs,” *Electrochimica Acta*, vol. 51, no. 28, pp. 6510 – 6520, 2006.

[67] Q. Pan, W. Tu, L. Ding, and G. Mi, “Characteristics of electric double layer in different aqueous electrolyte solutions for supercapacitors,” *Wuhan University Journal of Natural Sciences*, vol. 17, no. 3, pp. 200–204, 2012.

[68] K. H. An, K. K. Jeon, J. K. Heo, S. C. Lim, D. J. Bae, and Y. H. Lee, “High-Capacitance Supercapacitor Using a Nanocomposite Electrode of Single-Walled Carbon Nanotube and Polypyrrole,” 2002.

[69] X. Liu and P. G. Pickup, “Ru oxide supercapacitors with high loadings and high power and energy densities,” *Journal of Power Sources*, vol. 176, no. 1, pp. 410 – 416, 2008.

[70] H. Michel, “Temperature and dynamics problems of ultracapacitors in stationary and mobile applications,” *Journal of Power Sources*, vol. 154, no. 2, pp. 556 – 560, 2006. Selected papers from the Ninth Ulm Electrochemical Days.

[71] G. Ma, J. Li, K. Sun, H. Peng, J. Mu, and Z. Lei, “High performance solid-state supercapacitor with pva–koh–k3[fe(cn)6] gel polymer as electrolyte and separator,” *Journal of Power Sources*, vol. 256, pp. 281 – 287, 2014.

[72] Y. Marcus, “Volumes of aqueous hydrogen and hydroxide ions at 0 to 200C,” *Journal of Chemical Physics*, vol. 137, no. 15, 2012.

[73] “Size of atoms.” `http://chemed.chem.purdue.edu/genchem/topicreview/bp/ch7/size.html`, 2015. url date: 2015-09-25.

[74] N. Lange, *Handbook of Chemistry.* 1999.

[75] L. D. Wen Lu 2010-03-01.

[76] V. Khomenko, E. Raymundo-Pinero, and F. Beguin, “High-energy density graphite/ac capacitor in organic electrolyte,” *Journal of power sources*, vol. 177, no. 1, pp. 643–651, 2008.

[77] FastCap and Systems, “Fastcap technology.” `http://www.fastcapsystems.com/home/technology/`, 2015. url date: 2015-09-18.

[78] C. Luo, A. Govindaraju, J. Garra, T. Schneider, R. White, J. Currie, and M. Paranjape, "Releasing SU-8 structures using polystyrene as a sacrificial material," *Sensors and Actuators, A: Physical*, vol. 114, no. 1, pp. 123–128, 2004.

[79] B. D. Ratner, A. S. Hoffman, F. J. Schoen, and J. E. Lemons, *biomaterials science: An Introduction to Materials in Medicine*. 2004.

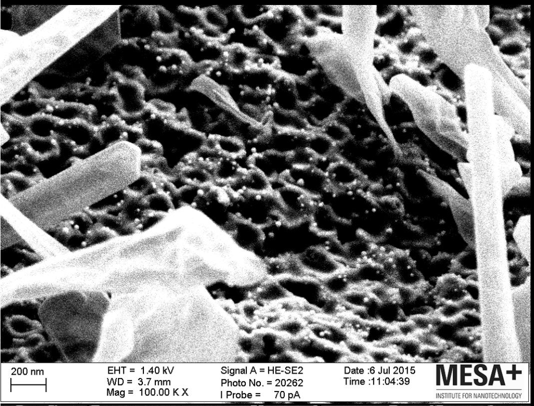
200 nm
EHT = 1.40 kV
WD = 3.7 mm
Mag = 100.00 K X
Signal A = HE-SE2
Photo No. = 20262
I Probe = 70 pA
Date :6 Jul 2015
Time :11:04:39
MESA+
INSTITUTE FOR NANOTECHNOLOGY

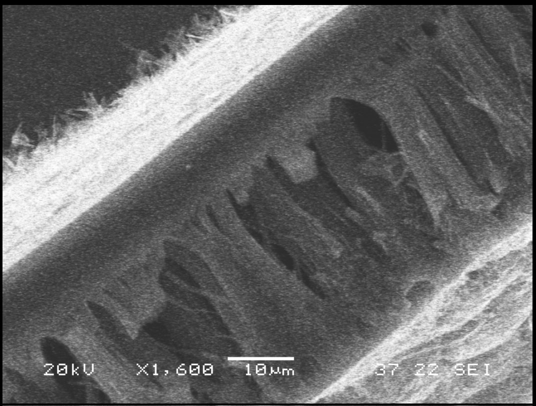
20kV X1,600 10μm 37 22 SEI

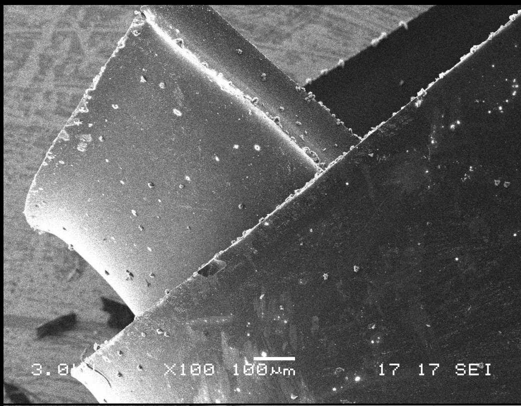
3.0 X100 100μm 17 17 SEI

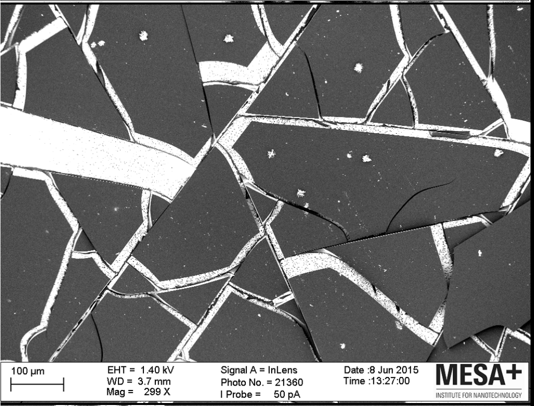
100 μm
EHT = 1.40 kV
WD = 3.7 mm
Mag = 299 X
Signal A = InLens
Photo No. = 21360
I Probe = 50 pA
Date :8 Jun 2015
Time :13:27:00
MESA+
INSTITUTE FOR NANOTECHNOLOGY

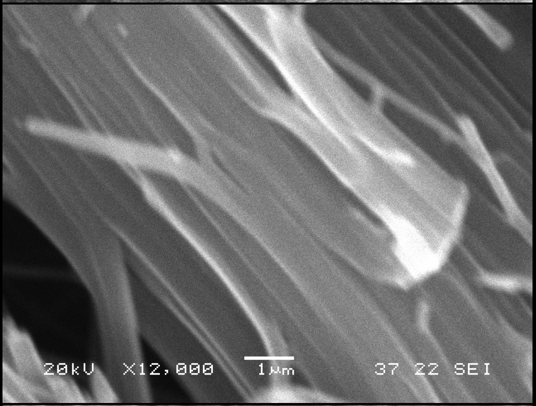
20kV X12,000 1μm 37 22 SEI

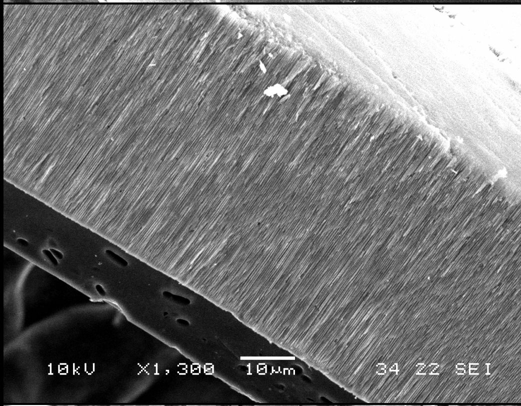
10kV X1,300 10μm 34 22 SEI

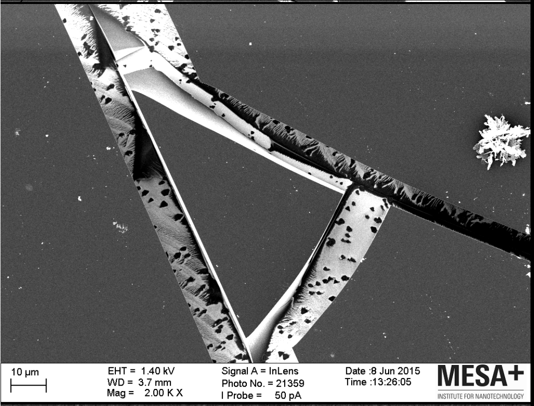
10 μm
EHT = 1.40 kV
WD = 3.7 mm
Mag = 2.00 K X
Signal A = InLens
Photo No. = 21359
I Probe = 50 pA
Date :8 Jun 2015
Time :13:26:05
MESA+
INSTITUTE FOR NANOTECHNOLOGY

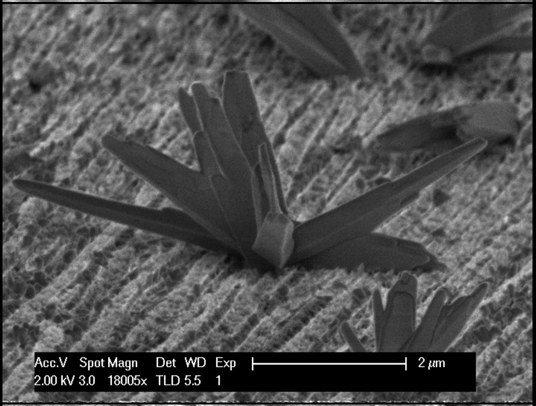
Acc.V Spot Magn Det WD Exp
2 μm
2.00 kV 3.0 18005x TLD 5.5 1

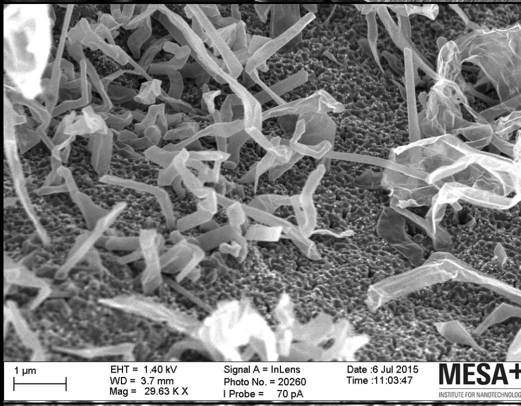
1 μm
EHT = 1.40 kV
WD = 3.7 mm
Mag = 29.63 K X
Signal A = InLens
Photo No. = 20260
I Probe = 70 pA
Date :6 Jul 2015
Time :11:03:47
MESA+
INSTITUTE FOR NANOTECHNOLOGY

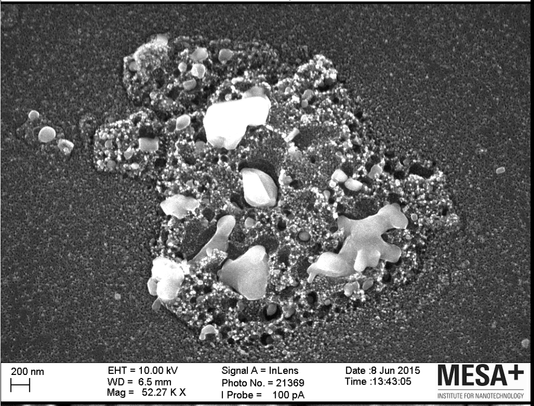
200 nm
EHT = 10.00 kV
WD = 6.5 mm
Mag = 52.27 K X
Signal A = InLens
Photo No. = 21369
I Probe = 100 pA
Date :8 Jun 2015
Time :13:43:05
MESA+
INSTITUTE FOR NANOTECHNOLOGY

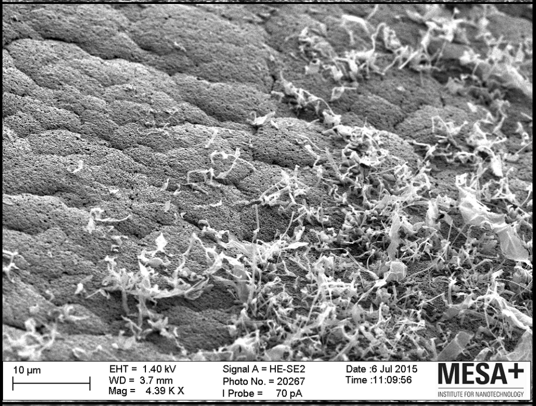
10 μm
EHT = 1.40 kV
WD = 3.7 mm
Mag = 4.39 K X
Signal A = HE-SE2
Photo No. = 20267
I Probe = 70 pA
Date :6 Jul 2015
Time :11:09:56
MESA+
INSTITUTE FOR NANOTECHNOLOGY

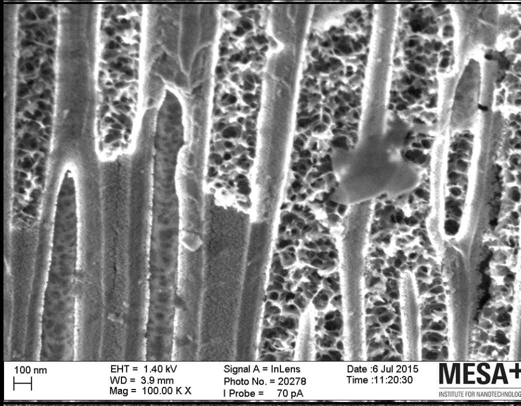
100 nm
EHT = 1.40 kV
WD = 3.9 mm
Mag = 100.00 K X
Signal A = InLens
Photo No. = 20278
I Probe = 70 pA
Date :6 Jul 2015
Time :11:20:30
MESA+
INSTITUTE FOR NANOTECHNOLOGY

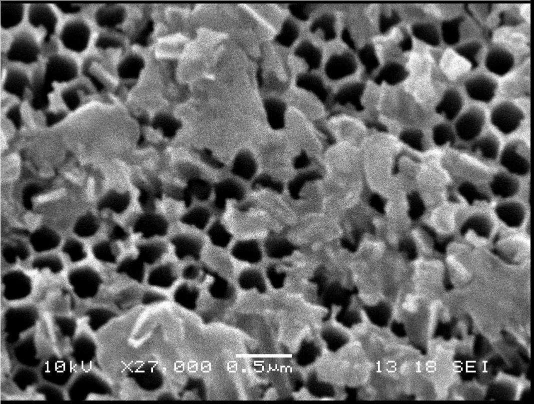
10kV X27,000 0.5μm 13 18 SEI

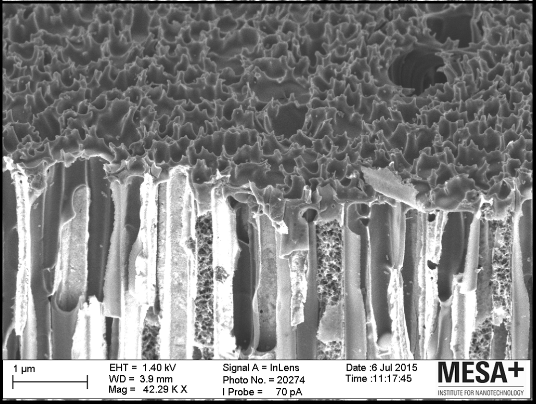
1 μm
EHT = 1.40 kV
WD = 3.9 mm
Mag = 42.29 K X
Signal A = InLens
Photo No. = 20274
I Probe = 70 pA
Date :6 Jul 2015
Time :11:17:45
MESA+
INSTITUTE FOR NANOTECHNOLOGY

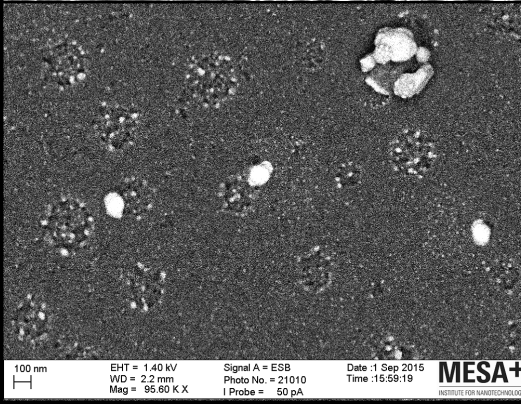
100 nm
EHT = 1.40 kV
WD = 2.2 mm
Mag = 95.60 K X
Signal A = ESB
Photo No. = 21010
I Probe = 50 pA
Date :1 Sep 2015
Time :15:59:19
MESA+
INSTITUTE FOR NANOTECHNOLOGY